2006

CHARACTERIZATION AND MEASUREMENT OF TENSION-INDUCED LONGITUDINAL WRINKLES IN GOSSAMER MEMBRANES USING PHOTOGRAMMETRY

SreeRam Mangalampalli
University of Kentucky, mareersm@yahoo.com

ABSTRACT OF THESIS

CHARACTERIZATION AND MEASUREMENT OF TENSION-INDUCED LONGITUDINAL WRINKLES IN GOSSAMER MEMBRANES USING PHOTOGRAMMETRY

Gossamer membranes are large, ultra light weight, highly flexible thin films. They have been proposed for use as elements in systems such as solar sails and optical apertures, whose large areas require a low-mass material that can be launched in a compact package and then deployed to operational configuration upon reaching orbit. Many of the proposed applications require that the film possess a flat, wrinkle-free surface. Surface wrinkle configuration is determined, in part, by the method used to support the film. One configuration that has not been studied in detail involves the formation of vertical wrinkles oriented along the direction of a tensile force applied at the upper and lower horizontal film supports. An experiment was designed to allow known forces to be applied to a 9 inch by 9 inch square sample of film supported at its upper and lower boundaries. Four films 7.6 μm and 12.7 μm thick samples of Kapton (polymide), and 12.2 μm and 23.4 μm thick samples of Mylar were loaded at levels of applied tensile force ranging from 1.446 to 4.388 N. The out-of-plane surface contours that resulted were measured using close-range photogrammetry, a non-contact, optical measurement technique. Experimental results indicate that both wrinkle wavelength and amplitude decrease as a function of applied force magnitude. These trends matched those obtained using numerical techniques, which also showed that lateral border strain, not measured during the experiment, may be a more important factor in determining surface wrinkle configuration. After presentation of the results, the photogrammetry technique is further considered as a tool for use in the manufacturing industry, in similar close-range applications, for the measurement of both dimensions and displacements.

Keywords: Gossamer membranes, solar sails, optical apertures, space contours, photogrammetry.

Signed: _____

Date: _____

CHARACTERIZATION AND MEASUREMENT OF TENSION-INDUCED LONGITUDINAL WRINKLES IN GOSSAMER MEMBRANES USING PHOTOGRAMMETRY

By

SreeRam Mangalampalli

_____
Director of Thesis

_____
Director of Graduate Studies

_____
Date

CHARACTERIZATION AND MEASUREMENT OF TENSION-INDUCED LONGITUDINAL WRINKLES IN GOSSAMER MEMBRANES USING PHOTOGRAMMETRY

By

SreeRam Mangalampalli

_____
Co-Director of Thesis

_____
Committee member

_____
Date

RULES FOR THE USE OF THESES

Unpublished theses submitted for the Master's degree and deposited in the University of Kentucky Library are as a rule open for inspection, but are to be used only with due regards of the rights of the authors. Bibliographical references may be noted, but with quotations or summaries of parts may be published only with the permission of the author, and with the usual scholarly acknowledgements.

Extensive copying or publication of the thesis in whole or in part also requires the consent of the Dean of the Graduate School of the University of Kentucky.

A library that borrows this thesis for use by its patrons is expected to secure the signature of each user.

Name Date

_____

_____

_____

_____

_____

_____

_____

_____

_____

_____

_____

_____

THESIS

SreeRam Mangalampalli

The Graduate School

University of Kentucky

2006

CHARACTERIZATION AND MEASUREMENT OF TENSION-INDUCED LONGITUDINAL WRINKLES IN GOSSAMER MEMBRANES USING PHOTOGRAMMETRY

THESIS

A thesis submitted in partial fulfillment of the requirements of the degree of Master of Science in Mechanical Engineering in the College of Engineering at the University of Kentucky

By

SreeRam Mangalampalli

Lexington, Kentucky

Director: Dr. Jack Leifer, Assistant Professor of Mechanical Engineering

Lexington, Kentucky

2006

CHARACTERIZATION AND MEASUREMENT OF TENSION-INDUCED LONGITUDINAL WRINKLES IN GOSSAMER MEMBRANES USING PHOTOGRAMMETRY

THESIS

A thesis submitted in partial fulfillment of the requirements of the
degree of Master of Science in
Mechanical Engineering
in the College of Engineering
at the University of Kentucky

By
SreeRam Mangalampalli
Lexington, Kentucky

Committee members
Co-Director: Dr. J. D. Jacob, Associate Professor of Mechanical Engineering and
Dr. Lawrence E. Holloway, Associate Professor of Electrical Engineering

Lexington, Kentucky

2006

MASTER'S THESIS RELEASE

I authorize the University of Kentucky
Libraries to reproduce this thesis in
whole or in part for the purposes of research.

Signed:_____

Date:_____

Dedication

To my father, grandmother and Jack Leifer

ACKNOWLEDGEMENTS

The following thesis could not be completed without the guidance and advice of my director, Jack Leifer. I could complete this thesis due to his patience and dedication. I thank him for the opportunity he has provided me in his research, his confidence in me at critical situations of the thesis, and those endless trips he made back and forth between Lexington and Paducah to make sure that I am not deprived of the guidance other students get from their advisors.

I am obliged to Dr. Suzanne Smith for providing me with the lab facilities to run my experiments. I would like to take this opportunity to extend my gratitude to Dr. Jacob who played a moral support to me during my masters. Working for him as a teaching assistant has greatly helped me strengthen my basics and thereby apply in my thesis. I thank Dr. Holloway for accepting to be my thesis defense committee member.

I am thankful to my father, Satya Mohan Singh Mangalampalli, who has empowered me to make decisions all through my career. I am greatly indebted to my grandmother , Venkata Ramani Indraganti, who believed me and inspired me all through my career. Last but not the least; I would like to thank my girl friend, Rajamanjari Mokrala, for encouraging me and standing behind me while I walked through my masters.

SreeRam Manglampalli

TABLE OF CONTENTS

LIST OF FIGURES

LIST OF TABLES

Chapter 1: INTRODUCTION

1.1 Introduction

Ever since the time of Aristotle, the science of photography developed slowly and steadily. Looking at the current technology, where cameras and software have become smart enough to measure objects in three dimensional space, many applications in many different fields where such non-contact measurement is useful have been identified. The two major roadblocks to a more widespread use of photogrammetry have been accuracy of measurements and response time. The demands of the applications in various fields such as topography, reverse engineering and manufacturing have driven the improvement of both measurement accuracy and data processing response time. While photogrammetry has been traditionally used to measure large objects and structures, a newer application that is more suitable for the size scales encountered in manufacturing is close-range photogrammetry. Measurement of small sized objects with high precision using this process is still an evolving technology; one application of the close-range photogrammetry process provides the focus of this thesis.

Manufacturing and quality inspections have been prevalent in some form throughout the existence of mankind. By the turn of the 20^{th} Century, the industrial revolution has increased efficiency in manufacturing. The quality of products has improved tremendously with the driving force of increasing competition, and the tolerance allowed by customers for poor quality parts has shrunk dramatically in the last ten years. With open markets, it has become important for manufacturing suppliers to meet the quality demands of their customers. In an era where outsourcing manufacturing to cheap labor countries like China has become more prevalent, it has become difficult for manufacturing companies in United States to compete with the labor costs of other outsourced products. Since the US cannot meet the price of outsourced products, it must exceed their quality, in order to prove their worth. In order to maintain the quality edge, some of these manufactured products require complicated dimensional inspection procedures that demand a lot of time and labor. In some cases, contamination issues might eliminate all inspection procedures except those involving non-contact methods. In situations like these, application of close-range photogrammetry to dimensional

inspection can provide a good solution that could both save considerable amount of labor costs through automation as well as ensuring that the desired quality goals are met.

One good place to test and apply close-range photogrammetry has always been the measurement of in-plane and out-of-plane displacements of Gossamer space structures. Gossamer space structures, considered as the next generation space structures, use films made of materials like Kapton and Mylar to greatly decrease the amount of mass that must be placed into earth's orbit. Their flexibility also enables structures to be deployed to a fully operational configuration from a small launch package, without requiring the need to assemble many parts (such as the procedure currently used to assemble the parts of the International Space Station). Gossamer films have thickness in the order of μm and are extremely light weight and flexible. Their inherent flexibility makes developing predictive models of their mechanical behavior a daunting task. Gossamer films are sometimes coated with Aluminum or Gold to provide highly reflective surfaces for applications such as solar sails, optical mirrors etc.

The performance of the films like Kapton and Mylar depends on their reflective capabilities. Due to the stresses that act on these films caused by various loads, these films tend to develop wrinkles on their surface, which are basically out-of-plane displacements. Over the past century, much effort has been exerted in developing both analytical and numerical models for the prediction of out-of-plane wrinkles as a function of load. In fact, this interest dates back to earliest powered flying vehicles, where thin plates of fabric, and later aluminum were used as control surfaces, as well as means of light weight structural reinforcements. One particular type of wrinkle, which has been observed, but not studied in detail, are the vertical wrinkles formed on thin films when pure tension loads are applied on the top and bottom edges under clamped conditions. In order to measure these out of plane displacements, a non-contact method must be used, as even the slightest of forces caused due to contact can affect the surrounding wrinkle pattern by large amounts. Hence, photogrammetry fits right in to provide a prototypical example for the application of close-range photogrammetry for high precision non-contact measurements.

1.2 Objectives of Thesis

The primary objective of this thesis is to study photogrammetry as a tool used to measure objects in 3-d space with high accuracy and precision. The specific objectives defined in this thesis are:

1. A review of the research done on out-of plane measurements of thin films.
2. Application of photogrammetry in the measurement of out-of-plane displacements of Kapton and Mylar films under pure tension loads as examples.
3. Explore various applications of photogrammetry in industry with a detailed study into the technology and method used in photogrammetry.
4. Study of applications of close-range photogrammetry as related to manufacturing and high precision instrumentation.

1.3 Thesis Summary

A brief introduction to photography along with its history is provided in the beginning part of Chapter 2. Photogrammetry is then introduced and a study of the timeline during which it developed is provided. Finally, earlier research in the measurements of out-of-plane displacements of thin films used in space applications is reviewed. Chapter 3 discusses the experimental set-up and the experimental analysis. It starts with the design and preparation of certain fixturing required and then describes the set-up of the experiment. The procedure for running the experiment is also provided. The chapter finally provides the process by which the photogrammetric data was processed using PhotoModeler and Surfer software. Using the three dimensional grid points of the film exported from Surfer, a procedure has been designed and followed to measure the wavelengths and amplitudes of the wrinkles formed on the films. These measurements are then documented and graphed in Chapter 4. Chapter 5 analyses the results and characterizes the wrinkles. It also discusses other parameters besides longitudinal tension that affects surface wrinkle amplitude and wavelength and discusses the shortcomings in the experimental apparatus to enable future improvements. The applications of photogrammetry in manufacturing are documented in Appendix B. Some of the critical specifications like accuracy of measurements and process time in photogrammetry are discussed in detail to provide information that could help in the right selection of cameras

and software for any particular application. Finally, the importance of application of photogrammetry to the measurement of gossamer films, along with some other applications related to close-range photogrammetry for manufacturing and precision measurements will be discussed in this section.

The significance of this thesis has been the exploration of close-range photogrammetry as an emerging technology that is becoming more commonly used in a diversified number of applications within manufacturing. Photogrammetry has the potential to continue to exceed the metrology demands of the manufacturing industry.

Chapter 2: LITERATURE REVIEW

2.1 History of Photography

From the time of Aristotle through the present, there have always been efforts to use camera equipment and principles of photography for both artistic purposes, as well as for scientific image reproduction and measurement. It is this later endeavor that forms the basis of the measurement method used in this thesis.

The earliest camera in the world was called the Camera Obscura, which consists of a dark room with a hole [1]. The principle behind the working of Camera Obscura dates back to 300 B.C. when Aristotle described that an inverted image is formed on a plane directly opposite a pinhole opening [1,2]. Roger Bacon invented the Camera Obscura in 13th century [2]. Johannes Kepler (Fig. 2-1) was the first person to coin the word Camera Obscura in 1604[2]. Gerolomo Cardono (1501-1576), an Italian mathematician, was the first to use a bi-convex lens in place of the pin hole in his camera [1]. Camera Obscura became a popular aid to sketching perspective drawings [1].

Fig. 2-1: Camera Obscura, Johannes Kepler, 1620 from [2].

From the original room size Camera Obscura, cameras have dramatically decreased in size. This was particularly due to the work of Johann Christoph Sturm, a Mathematics professor at Altford who invented the reflex mirror in 1676 [2]. The initial Camera Obscure required artists to stand and paint the projected image. However, the reflex mirror, when placed at an angle of 45˚, reflected the image onto the lap and thereby helped them to sit and paint in a more comfortable position. This also helped to further decrease the size of the camera. Johann Zahn constructed lenses of shorter and longer focal lengths in 1685 [2]. He also painted the interior of his camera dark [2]. Together, these advances provided the prototype on which all modern cameras are based.

The creation of permanent images on a substrate lagged the development of cameras by many years. In 1827, Joseph Nicephore Niepce produced the first ever picture on a chemical substrate [3]. The substrate hardened on exposure to light and required an exposure time of eight hours [3]. In 1829, Louis Daguerre discovered a process, later named "Daguerreotype" that reduced the exposure time to half an hour [3]. Johann Von Meadler, an astronomer from Berlin, was the first to use the word "photography" in 1839. Later in the same year, Sir John Herschel used this term in his lecture to the Royal Society [3]. Frederick Scott Archer introduced the Collodion process in 1851, which further reduced the exposure time to as little as two or three seconds. The first photographic film, developed by John Corbutt, an Englishman working in Philadelphia, in 1888 was initially produced in flat sheets [3]. George Eastman later developed the film roll in 1889 for his camera, which he named "Kodak", first produced in 1886 [3] (Fig. 2-2). This advance allowed multiple images to be stored inside the camera, and developed at a later time [3].

Fig. 2-2: Kodak Camera.

Kodak was the first company to make cameras available to the public [3]. The company developed cameras of size 6" X 3" X 3" that weighed only 3 pounds [3]. These cameras were portable, and the required exposure time was only $1/25^{th}$ of a second.

Sherman Mills Fairchild was a successful entrepreneur who developed a between-the-lens shutter that used a rotary blade. He developed the K-3 camera, as well as a series of successor models that were used in the Explorer II balloon fights and for mapping the moon's surface during the Apollo missions [9].

During the 1960s, NASA stipulated that digital signals be used for imaging, which prompted the development of film less, digital cameras. Texas Instruments patented the first camera that utilized an electronic imaging element in 1972 [2]. In 1986, Kodak designed the world's first mega pixel sensor. Apple and Kodak were some of the first companies to introduce digital cameras to the market for the general public [2] (Fig. 2-3).

In digital cameras, light passes through the lenses and forms an image upon striking a digital sensor array chip (such as CCD or CMOS) instead of the traditional film [30]. Regardless of the type, each digital sensor is made of millions of tiny light sensitive points called pixels [30]. The first sensor designed by Kodak had 1.4 million pixels on it [29]. When light strikes such a sensor, each pixel gets excited, and produces a signal that is proportional to the intensity of the incoming light. The signals then pass through a series of analog devices, an analog to digital converter, and electronic filters to adjust for color, white balance and aliasing. Unnecessary pixel signals are removed for image compression and the remainder of the image is stored in temporary memory for further processing, subsequent storage on removable media, or display [30]. Although described in simplified form, these steps comprise the basis of operation for most digital cameras on the market today.

Fig. 2-3: Kodak DC40, one of the first ever commercial digital cameras, 1995 from [2].

2.2 History of Photogrammetry

According to the Institute of Photogrammetry and Geo-Information, "Photogrammetry is the science and art of determining the size and shape of objects as a consequence of analyzing images recorded on film or electronic media." [4]

Leonardo da Vinci is one of the originators of the principles of perspective and projective geometry that forms the building blocks of photogrammetry theory [5]. In 1480 he wrote "Perspective is nothing else than the seeing of an object behind a sheet of glass, smooth and quite transparent, on the surface of which all the things may be marked that are behind this glass. The nearer to the eye these are intersected, the smaller the image of their call will appear." [6]

In its early stages, photogrammetry was used to plot topographical and thematic maps. Evolution of photogrammetry is divided into 4 major development cycles [7]. They are:

a) Plane table photogrammetry, approximately 1850-1900

b) Analog photogrammetry, approximately 1900-1960

c) Analytical photogrammetry, approximately 1960-1990

d) Digital photogrammetry, approximately 1990-present

2.2.1 Plane Table Photogrammetry

Plane table photogrammetry mainly involved taking pictures using stationary cameras to compile 2D maps. After the first photograph was made in 1827, R. Sturms and Guido Haick were the first to relate projective geometry to photogrammetry in 1883 [6]. Aime Laussedat, who is referred to as "the father of photogrammetry" was the first to compile topographic maps using terrestrial photographs [5]. C.B Adams invented the radial line triangulation to solve the analytical part of plane table photogrammetry [5]. Dr. Albecht Meydenbauer coined the word photogrammetry. He used Pantoshop lenses with wide angles of 105° in his cameras, and used intersections of corresponding lines from different cameras in order to produce mapped images (Fig. 2-4) [8]. He achieved high accuracy (order of 2 X 10^{-4} m) by using a large format size (0.40 m X 0.40 m) and selecting photo scale to map scale factors of less than 2 [5]. Photo scale is the ratio of the distance between any two points on a photo to the distance between corresponding points on the object. Similarly, map scale is the ratio of the distance between any two points on a map to the distance between corresponding points on the object. In those days measurements made using photographs were translated into maps and stored. Meydenbauer insisted that the ratio of photo scale to map scale be less than 2, to ensure better resolution in the measurement and mapping of objects and structures [5].

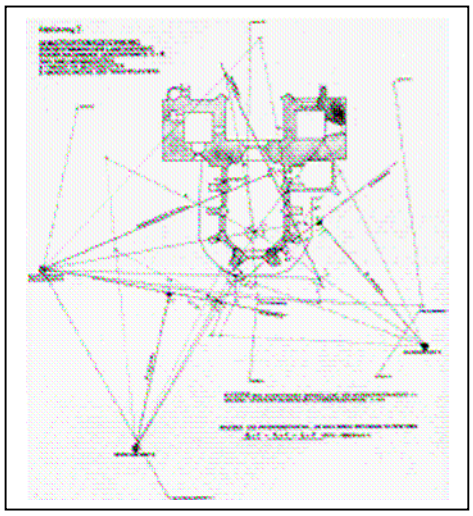

Fig. 2-4: Early works of Dr. Albrecht Meydenbauer on Photogrammetry from [5].

2.2.2 Analog Photogrammetry

The discovery of stereoscopy and the invention of the airplane provided an increased rate of progress for the development of photogrammetry during this period. According to www.startphoto.com, stereoscopy is "photography that uses two images taken from slightly different angles to produce the illusion of three dimensions when seen through a special viewing device" [31]. This advancement helped realize three dimensional measurements with the help of two dimensional photographs. Eduard Gaston and Daniel Deville presented the first stereoscopical instrument for vectorized mapping in 1896, which they called stereo-planigraph in 1896 [5, 9]. He was successful in mapping the Rocky Mountains using this instrument. Professor Reinhard Hugershoff (1882-1941) designed different versions of analog plotters such as the Huggershoff autograph, Universal phototheodolite, aerocartograph, and stereocomparator. Each of these represented an improvement over the previous device, and were all used for various applications. Analog plotters are optical/mechanical instruments used to construct 3D geometry with the help of overlapping images [32]. In 1924, Otto von Gruber derived projective equations and their differentials, which formed the basis of analytical photogrammetry. Later, Earl Church (1890-1956), also known as the "American Father of Photogrammetry", developed the analytical solutions to space resection, orientation, intersection, rectification, and control point extension using directional cosines.

According to Leica Geosystems, "Space resection is the technique used to determine the exterior orientation parameters associated with one image or many images, based on the collinearity condition" [32]. Orientation is the establishment of relationship between the image coordinate system and the object's coordinate system [33]. According to Leica Geosystems, space intersection is the technique used to determine ground coordinates X, Y and Z of points that appear in the overlapping areas of two or more images based on a collinearity condition, which specifies that the exposure station, the ground point and its corresponding image point location must all lie along a straight line [32]. "The process of removing geometric errors caused by various factors inherent in photography and imagery" is known as rectification and the process of extending known coordinates of a point to the corresponding point in the photo is called control point

extension [32]. Many of the basic technologies associated with modern photogrammetry systems were developed and implemented by Earl Church.

2.2.3 Analytical Photogrammetry

Analytical computation of photogrammetry was a complicated task until the development of modern digital computers [5]. The principles of modern analytical photogrammetry, where cameras are set up at different locations (stations) were first developed by Dr. Hellmut Schmid in 1953, using matrix notation. He used transformation matrices to transform the 2D coordinates and angles of each image into the 3D coordinates of the physical object. The development of the analytical plotter also took place during the era of analytical photogrammetry. Analog photogrammetry substituted the expensive mechanical instruments of analog plotters with inexpensive mathematical computation. Hence, it was feasible to compute 3-dimensional geometry with the help of computers and analytical plotters. By this time, 3D mapping was quite possible and it was very easy to apply techniques like Monoplotting and Analytical Stereophotogrammetry, which were prominent during the 1970s [4].

2.2.4 Digital Photogrammetry

Simultaneous to the development of digital photography, this phase of photogrammetric evolution is fast picking up with multiple applications in day to day life. Some of the major contributors to this development cycle were Hobrough, with an automated ortho-photographic system called Gesalt Photo Mapper (GPM) and Uki Helava, who helped develop digital photogrammetric workstations for the Defense Mapping Agency [5].

2.3 Applications of Photogrammetry to Analyze Thin Membranes

Gossamer spacecraft are a new class of ultra lightweight structures that incorporate thin-film membranes. Certain spacecrafts incorporating Gossamer structures, including solar sails, could extend over thousands of square feet in area. In order to help minimize launch weight, it is necessary to achieve minimal aerial densities that could approach

$0.01 kg/m^2$ for certain structures under study by NASA. As this requirement results in very large, yet highly compliant structures that are easily deflected and deformed, understanding the displacement response of these structures is a vital step that must be taken before they are deployed in order to allow them to be managed and controlled during post deployment. One step of understanding the behavior of a thin film structure is simply measuring its response under a known displacement or load state. However, conventional (contacting) sensors cannot be used for the following reasons: (1) They are generally massive enough to significantly affect the response of the thin film and (2) most contacting sensors provide single point measurement, whereas the in-and-out-of-plane surface response of structures are location dependent. Hence a full-field three dimensional non-contact measurement technique is indicated, and photogrammetry, since it allows full field, three dimensional measurements, is a logical choice.

One aspect of the behavior of thin films under in-plane tension is its tendency to respond with both in-plane and out-of-plane displacement components. This tension-induced wrinkling in thin film membranes was first measured using photogrammetry in 1997 [18]. The application of photogrammetry to study the wrinkling pattern of thin film structures such as solar sails was first identified in 2001 [18]. Until then photogrammetry was mainly used in remote sensing and topographical measurement applications. The advantage of converting 2D images to return the 3D coordinates without actually touching the object in observation proved to be a great asset in the observation of these thin membranes. In 2003, NASA funded a Gossamer structure effort under the "In-Space Propulsion" program, which recently selected teams led by L'Garde, Inc. and Able-AEC to further study the behavior of large, scale models of these thin membranes under various transient (deployment) and steady state conditions [19]. Since many of these tests were done under vacuum conditions, photogrammetry and videogrammetry were chosen methods of choice for recording the behavior of scaled test articles. Since 2001, various experimental measurements have been performed on deployed scale-model solar sails [20], integrated solar sail diagnostic systems [19], thin square membranes under shear [21], and simply supported membranes under gravity [24]. Many of these measurements use adhesive-backed retro-reflective targets attached to the surface of the film to allow tracking and measurement of in-and-out-of-plane motion. However, due to the light

weight of the thin films, retro-reflective targets potentially can have a significant effect on their response. Hence, techniques have been developed to precisely target the motion of the thin film structures using laser-induced-fluorescence and projected dots of light [22, 23]. While neither method provides any additional mass on the film surface, only out-of-plane motion can be tracked using the latter method, and the former requires the use of specially prepared membrane materials. Both of these factors may be limiting for certain applications.

2.4 Analysis of Tension-induced Wrinkle Patterns on Thin Membranes

The propulsion mechanism that is predicted to induce acceleration in solar sails is provided mainly through the reflection of photons on the surface of these sails, which cause a momentum transfer from each photon to the membrane. Due to the structure of the solar sails (mainly corner supports), tension loads act upon the solar sails and cause wrinkles on their surface. It is believed that these surface deviations can cause problems such as regions of uneven heating that could seriously degrade the performance and function of the solar sail. NASA is studying the effect of various mechanical and thermal loads on thin film membranes that are believed to result from wrinkling [18].

Various studies have been performed to observe the wrinkling patterns of thin membranes under various loading conditions. Jenkins et al. designed an experimental setup (Fig. 2-5) to study a square Mylar foil with side length of 228.6 mm subject to a combination of tension and shear forces. He used stepper motors to provide forces in X and Y directions and force transducers attached to a computer controlled system to measure them [39]. Using a capacitive displacement sensor, the amplitude, wavelength, angle of wrinkle inclination and the number of full wave wrinkles generated were measured. Jenkins et al. also observed that the number of wrinkles increased with the increase in tension and decreased with the increase in shear load up to a certain limit in each membrane tested. Also, the wrinkle orientation angle increases with shear load until it maximizes along the diagonal of the membrane at 45°, and tended to decrease as tension was increased. Finally, it was also observed that the wrinkle amplitude increases with shear force and decreases with tension force [39].

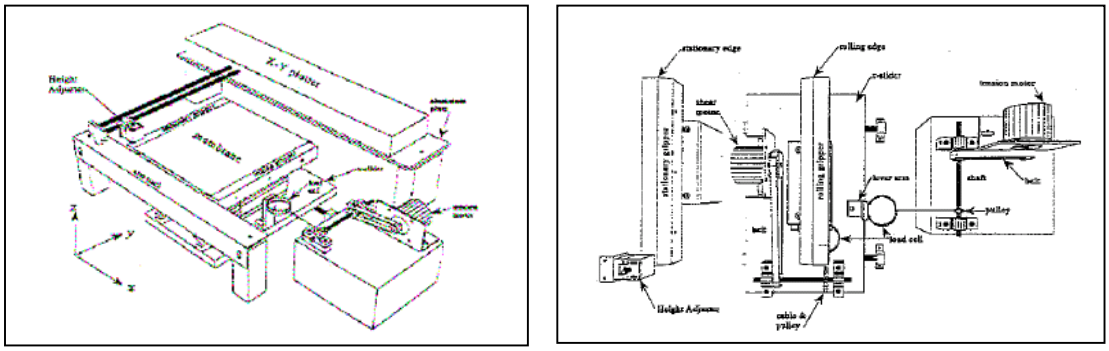

Fig. 2-5: Experimental setup of Jenkins et al. [39].

Wong successfully compared simulations and experiments on various shapes and sizes of the Kapton and Mylar membranes [35]. In 2002, Wong and Pellegrino simulated the wrinkles on thin membranes under pure shear (and low tensile pre-load) in the finite element software ABACUS, in order to study and validate the amplitude and wavelength of the wrinkles [26, 27]. A 25 μm thick rectangular Kapton foil of length 380 mm and height 128 mm was used to simulate wrinkles [27]. An initial step of applying a uniform pre-stress σ_y = 1.7 N/mm^2 in the Y direction was performed. They did eigen buckling analysis to predict what the wrinkle patterns would be (but could not determine the amplitude using that method). They then inserted small inhomogeneties into the FE mesh based on the predicted wrinkle pattern, and applied a lateral displacement along the top edge in small steps up to 3 mm. This simulation was later updated by Leifer and Belvin [37]. They replaced the applied out-of-plane mesh inhomegeneties with small out-of-plane forces that were later removed once the wrinkle pattern was established in the mesh. They showed that the eigen-buckling analysis was not necessary to accurately predict wrinkle contour geometry and amplitude. Similar numerical work done in ABACUS by Tessler and Sleight validated these results. Besides developing a method for simulation wrinkle contours, Wong and Pellegrino used three different mesh sizes to demonstrate the independence of wrinkles over mesh size once certain threshold mesh geometry has been reached. The principal mid-plane stresses were observed to be of the order of 20 N/mm^2 and 40 N/mm^2 corresponding to displacements of 1.6 mm and 3 mm

in the X direction, respectively (Fig. 2-6). The paper notes that neither the analytical solution nor the numerical solution was exact. However, the numerical solution qualitatively resembled the experimentally observed wrinkles. Finally, Wong and Pellegrino compared their simulated results with the experimental results of Jenkins et al [27]. Fig. 2-7 shows the mid height cross sections for different shear displacements along the top edge of the membrane.

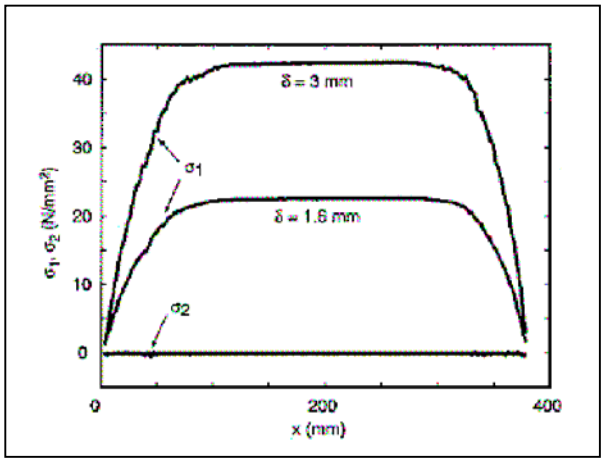

Fig. 2-6: Principle mid-plane stresses across mid-height section [27].

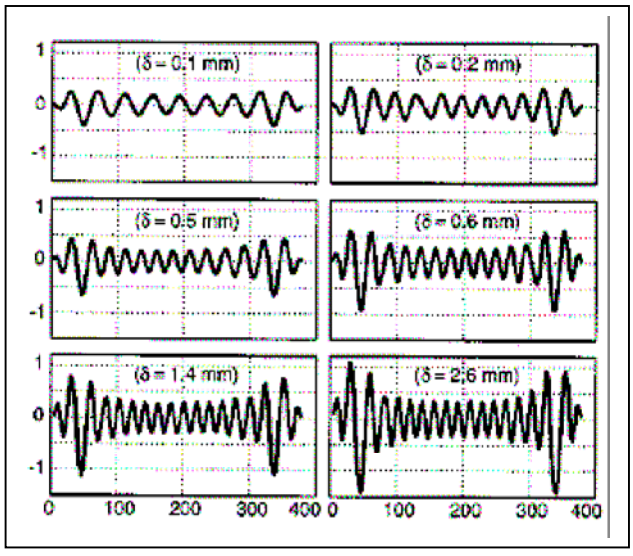

Fig. 2-7: Principle mid-height cross section for different applied shear displacements [27].

Wrinkle amplitude was determined by Leifer and Belvin for a 380mm X 128mm Kapton foil of thickness 25 μm under pure shear using simulation techniques in the ANSYS finite element modeling software package [37]. It was required to initiate the post-buckled behavior (Fig. 2-8) on the film in order that the wrinkles observed experimentally are formed within the simulation. The results were compared to the models developed by Wong and Pellegrino [37]. Fig. 2-9 shows the simulated wrinkles in ANSYS.

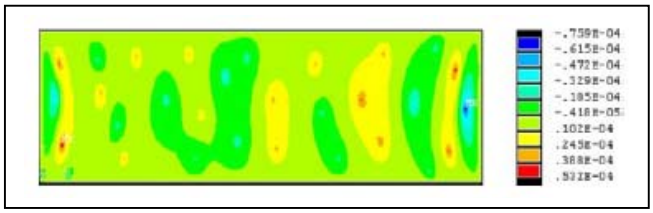

Fig. 2-8: Initiation of post-buckle wrinkles in the membrane, prior to the removal of the out-of-plane "inducement" forces [37].

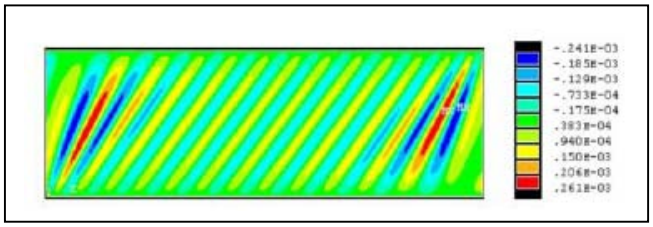

Fig. 2-9: Simulated wrinkles in the Kapton membrane using ANSYS [37].

Wong and Pellegrino's analytical approach, referred to in the previous section, presented an experimentally verified method for calculating wavelength and amplitude of the wrinkles under pure shear (Fig. 2-10). They demonstrated this approach using a 0.025 mm thick rectangular Kapton membrane with dimensions of length (L) 380 mm and height (H) 128 mm [26]. They calculated that once shear-induced wrinkles were fully developed, the major principle stress is inclined at 45°, along the wrinkle direction in the central, uniformly wrinkled part of membrane. The out of plane deflection, W (ξ, η) was calculated to be

$$W = A\sin\frac{\pi\xi}{\sqrt{2}H}\sin\frac{\pi\eta}{\lambda} \qquad \text{(Eq. 2.1)}$$

where A is the amplitude of the wrinkle

H is the height of membrane

λ is a wrinkle half-wavelength measured in the ξ direction

Using Wong and Pellegrino's method based on membrane equilibrium, the wrinkle wavelength can be calculated using

$$2\lambda = \frac{2\sqrt{\pi}}{\left[3(1-\upsilon^2)\right]^{1/4}}\frac{\sqrt{HT}}{\gamma^{1/4}} \qquad \text{(Eq. 2.2)}$$

where γ is the shear strain at 45°

υ is the Poisson's ratio

T is the membrane thickness

Using that result, the wrinkle amplitude was determined by matching the contraction of the membrane to the sum of the strain in the membrane and the geometric strain produced by the out of plane deformation of the membrane. The amplitude A is therefore predicted to be

$$A = \frac{\sqrt{2(1-\upsilon)}}{\sqrt{\pi}\left[3(1-\upsilon^2)\right]^{1/4}}\sqrt{HT}\gamma^{1/4} \qquad \text{(Eq. 2.3)}$$

Thus, it was found that λ is inversely proportional and A is directly proportional to the fourth root of shear angle and both of them are directly proportional to the square roots of the width and thickness of the membrane [26]. Fig. 2-10 shows the sheared Kapton sheet. Note the fully-developed wrinkles in the central portion of the membrane. It is assumed that the top edge in the figure has been displaced slightly uniformly to the right and the bottom edge has been clamped.

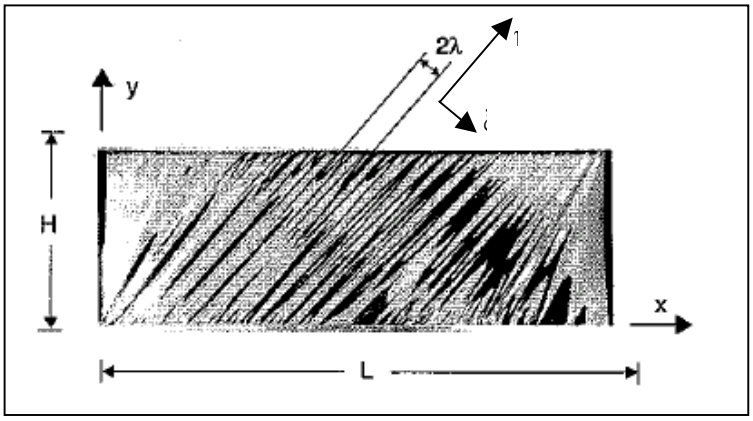

Fig. 2-10: Sheared Kapton Sheet [26].

An extended version of the work covered by Wong and Pellegrino [26] is contained in Wong's thesis dissertation submitted to the University of Cambridge. Beside the analytical approach to determining wrinkle amplitude and wavelength described in Eq. 2.1 - 2.3, he verified the prediction of amplitude using a strain energy approach, which yielded results equivalent to that shown in Eq. 2.2.

The strain energy approach calculates the total mean strain energy of the wrinkle per unit area and minimizes it with respect to the wavelength in order to calculate the wavelength. The total mean strain energy is considered as the sum of the bending strain energy and the stretching strain energy. Fig. 2-11 shows an experimental setup used by Wong to simulate shear in the membrane [35]. Fig. 2-12 provides a sketch of how the shear was applied [35].

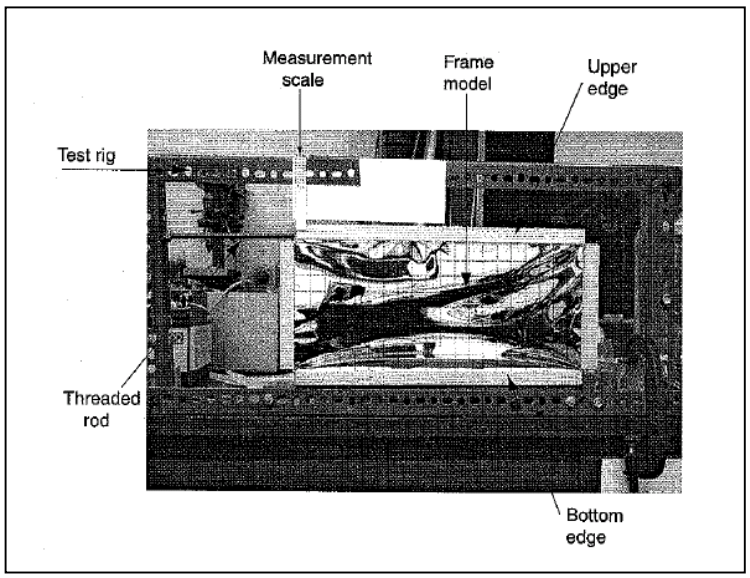

Fig. 2-11: Experimental setup to simulate pure shear [35].

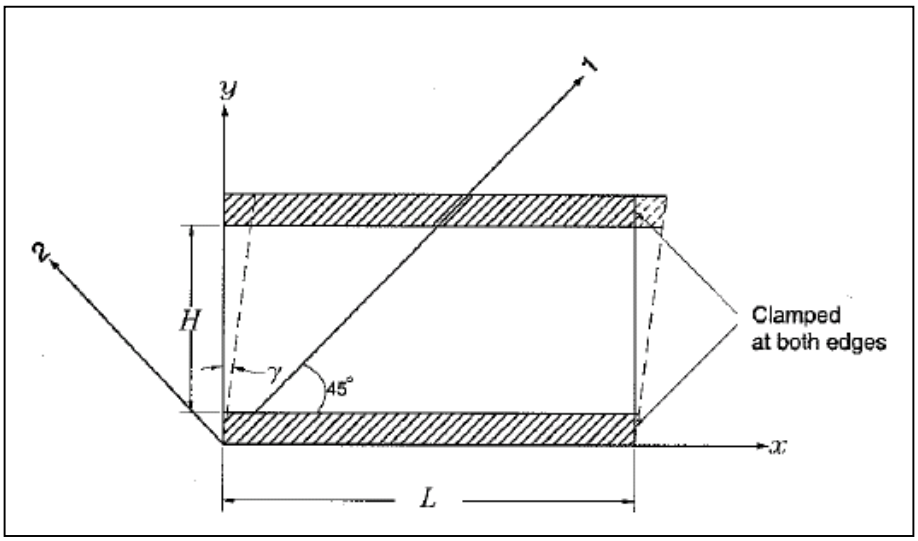

Fig. 2-12: Application of shear on a clamped membrane [35].

Computation of amplitudes and wavelengths of wrinkles in membranes under pure tensile loads applied along the plane of the membrane has proven to be a challenging problem. The development of such wrinkles (γ=0) was documented (though not discussed) by Jenkins et al. where low amplitude vertical wrinkles were photographed under an applied tension with zero edge shear [39]. Fig. 2.13 shows the graph of Amplitude v/s shear forces for different cases plotted by Jenkins et al. [39]. The graph shows that slight amplitudes between 0 mm and 0.2 mm can be observed when pure tension loads and no shear are applied on the membrane. This has inspired the study of wrinkle amplitudes and wavelengths for various materials and membranes with different thicknesses under the influence of pure tension loads and zero shear. Although these pure tension induced wrinkles were documented, no simulation or analytical approach for predicting wavelength and amplitude has been found in the literature. It is the characterization of these wrinkles that form the bulk of this thesis work. A loading configuration that produces such wrinkles is a square membrane oriented vertically, with top and bottom edge configurations constrained by metal strips. By fixing the top edge and applying a known load along the bottom edge (pure tension), a vertical wrinkle pattern can be developed within the central region of the membrane in a controlled and repeatable fashion. By applying a series of known tensile loads and observing changes in the resulting wrinkling pattern in various membrane systems, the effect of material

parameters, membrane thickness, and magnitude of applied load on the wrinkle amplitude and characteristic wavelength can be determined. These experimental observations can be used to verify analytical and numerical models of the wrinkling behavior. A detailed discussion of apparatus used to systematically produce and record vertical tension-induced wrinkles in contained in the next chapter.

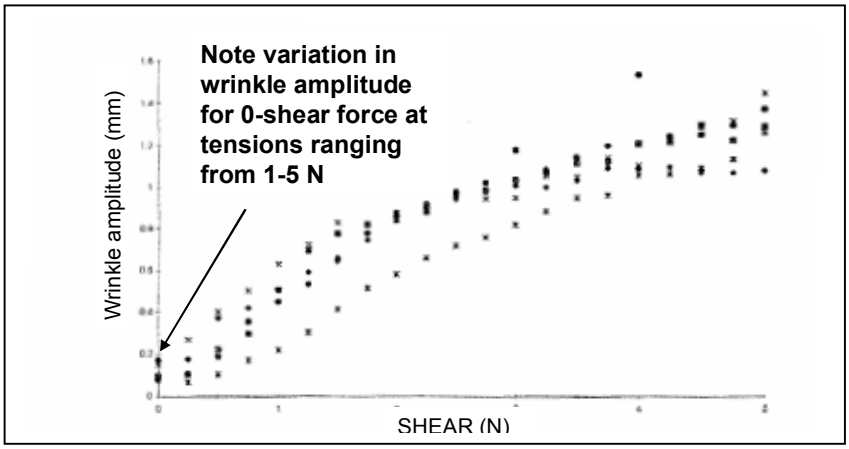

Fig. 2-13: Graph from Jenkins et al. plotted amplitude versus shear forces that shows amplitude for wrinkles under pure tension loads [39].

Chapter 3: EXPERIMENTAL

3.1 Introduction

It was desired to design apparatus that would enable the measurement of tension induced membrane wrinkling under various loading conditions. Fig. 3-1 shows one type of loading scheme, that of uniform tension.

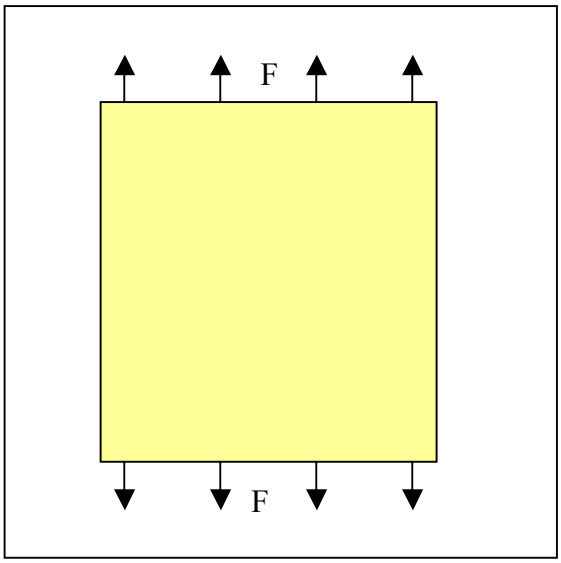

Fig. 3-1: A schematic to produce
uniform tension in a square membrane.

3.2 Distribution of Load

In order to apply a tension load uniformly across the top and bottom boundaries, membrane stiffeners such as those shown in Fig. 3-2, were used to sandwich the top and bottom edges of the membrane, allowing uniform tension conditions to be induced by applying loads at the stiffeners. Two stiffeners were used at the top edge of the membrane, and two were used in a similar fashion on the bottom. A complete schematic diagram showing the membrane, stiffeners and adapter plate is shown in Fig. 3-4 along with a photograph of the corresponding setup. The load was applied via small through holes located along the length of each stiffener. Bolts and adapter plate (Fig. 3-3) were used along the top stiffeners to completely constrain the top edge of the membrane; spring loads attached to thin cables tied to the holes in the bottom stiffener were used to

apply tension to the membrane. According to St. Venant's principle, forces acting far away from the local region of application do not affect the object. In other words, the localized forces applied using this scheme resulted in a fairly uniform force distribution within the membrane stiffeners and were not simply localized forces at each point of application.

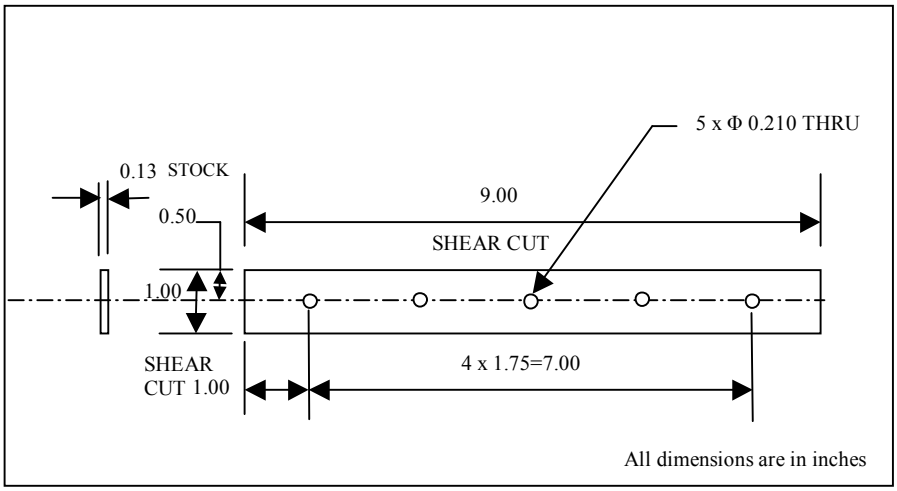

Fig. 3-2: Membrane stiffeners.

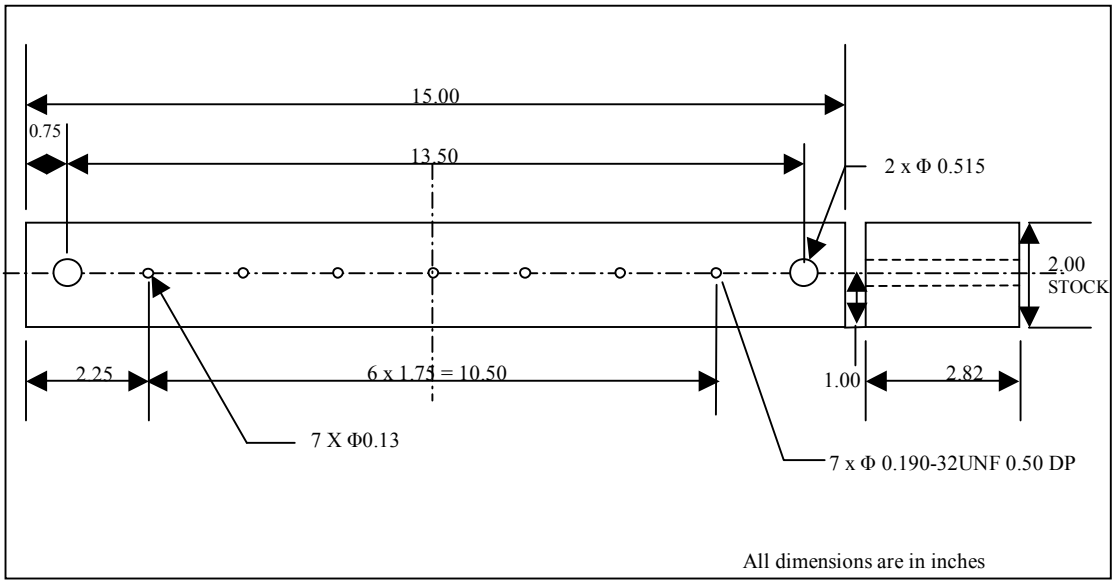

Fig. 3-3: Design of the upper adaptor plate.

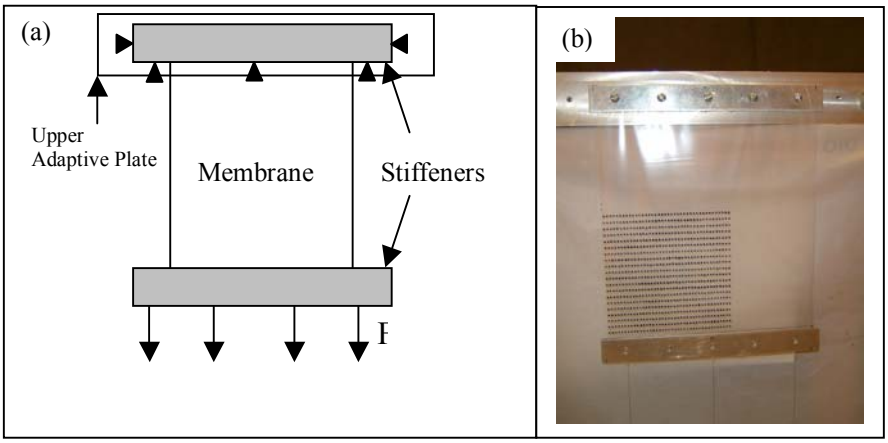

Fig. 3-4: Application of loads (a) Schematic (b) Picture.

3.3 Application of Load

In order to apply a uniform vertical force to the bottom membrane stiffener it was initially planned to apply loads using weights hanging from the membrane stiffeners themselves (Fig. 3-5). This method was chosen because mass loading had been successfully used in the corner loaded membrane experiments performed by Wong and Pellegrino as well as others [28]. However, initial trials showed that using weights freely hanging at the ends resulted in a highly under-damped system that oscillated when disturbed by minor breezes in the lab, caused by someone passing the set up, or even opening or closing a door. Since the amplitude of these disturbances were as large as the out of plane membrane wrinkles under study here, an alternative means of applying a known tension to the membrane was required. A better idea that eliminated membrane oscillations was to attach the bottom of the membrane to three spring balances which in turn, were constrained by a lower adaptor plate as shown in Fig. 3-6. A spring balance is an instrument typically used to measure loads, and contains a spring attached to a hook. The principle of the operation of spring balance is that the displacement of spring is directly proportional to the force applied. So, when a force is applied on the ends of a spring balance by an attached cable or string, the force applied is equal to the tension in the string which can be read by the scale on the spring balance as shown in Fig. 3-7.

In order to apply a known force, a screw and nut arrangement was designed using the pitch principle. One end of the fishing line (serving as a cable) was tied to the end of

the spring balance. The other end of the fishing line was tied tight against a right handed carriage screw that was screwed into the lower adaptor plate. In order to increase the load, the carriage screw was turned forward, so that the fishing line wound around it. The fishing line then pulled the hook of the spring balance and increased the applied tension load. Fig. 3-8 shows the complete set-up designed along with the schematic.

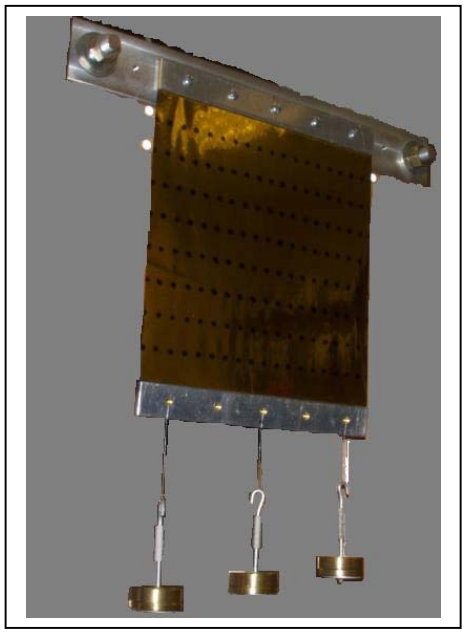

Fig. 3-5: Applied tension with hanging weights.

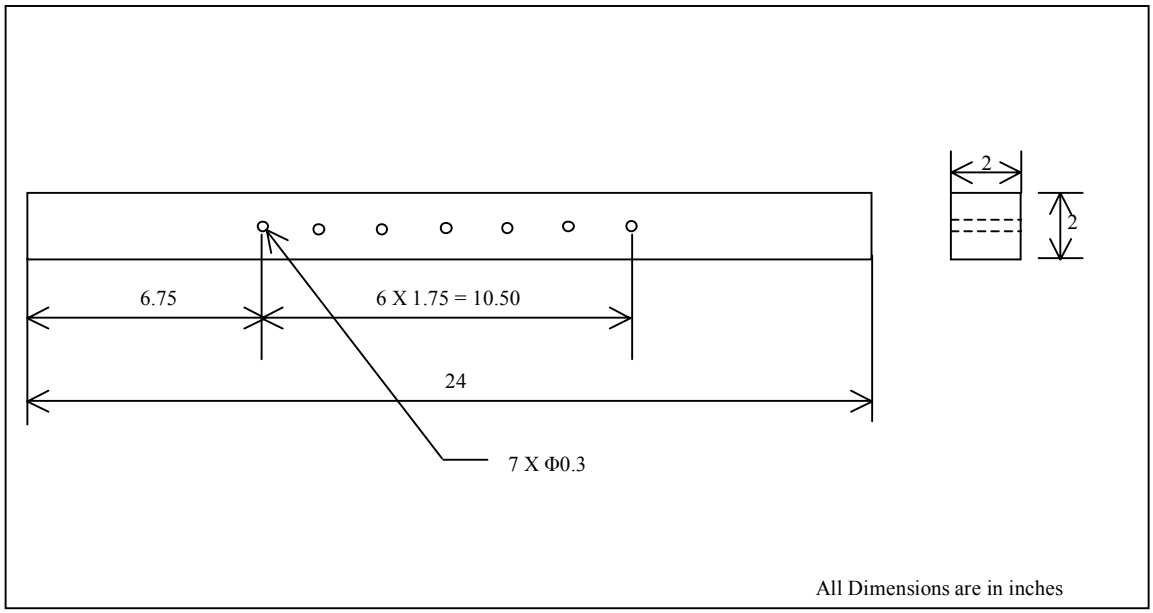

Fig. 3.6: Design of lower adapter plate.

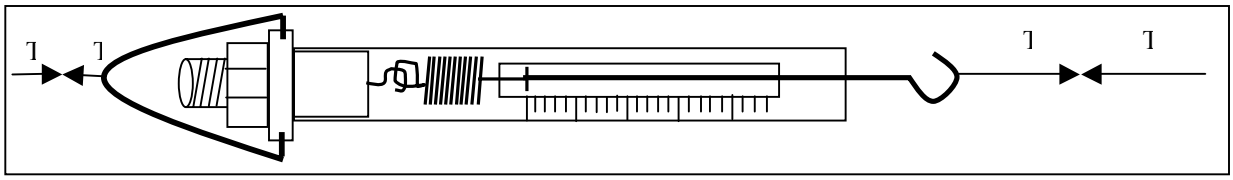

Fig. 3-7: Schematic of a spring balance with tension loads acting on it.

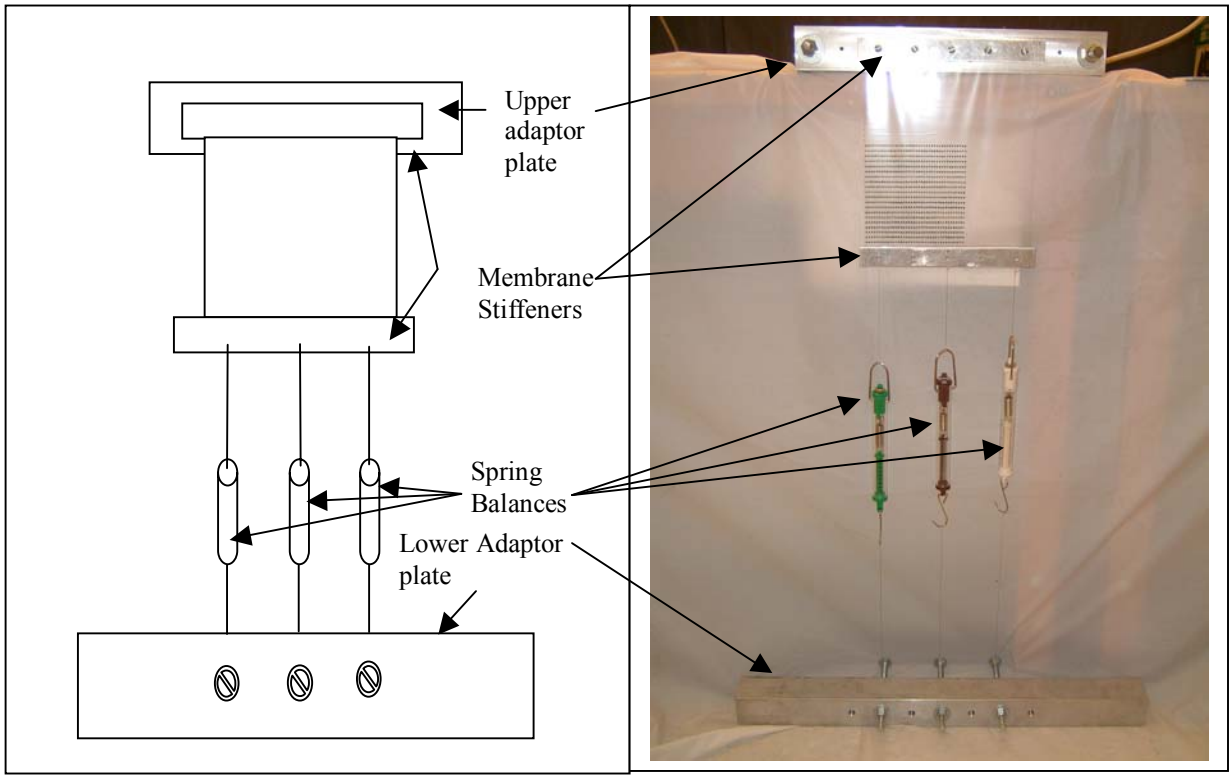

Fig. 3-8: Schematic and picture of the complete set-up of the experiment.

3.4 Measurement of Test Article using Photogrammetry

3.4.1 Approach

As mentioned previously, photogrammetry is a non-contact measurement method that is capable of performing very precise, full field measurements of surface contour. In the present experiment, the idea was to use four cameras (referred to here as cameras 1-4) to simultaneously image the same object from multiple vantage points. This scheme was chosen based on prior studies conducted at NASA Langley and others that used a similar set of instrumentation [18; 21-24; 36-38]. Using photogrammetry software such as PhotoModeler® Pro, a specific point on the object under evaluation is located on each image in two dimensions. The two-dimensional coordinates of the point in each image are then used to calculate the absolute three-dimensional location of the point, through a process known as triangulation. If enough points on the object under study are targeted and located in three dimensions using this method, the object's shape can be approximated by the resulting "point cloud" (Fig. 3-9). After proper benchmarking, we can plot the points in 3D space with mapping software like Surfer®, which imports all the points calculated by PhotoModeler Pro and uses a Krigging algorithm to estimate the shape of the best-fit surface formed by the points. The shape contour calculated by this process can then be exported to other software packages and used for analysis.

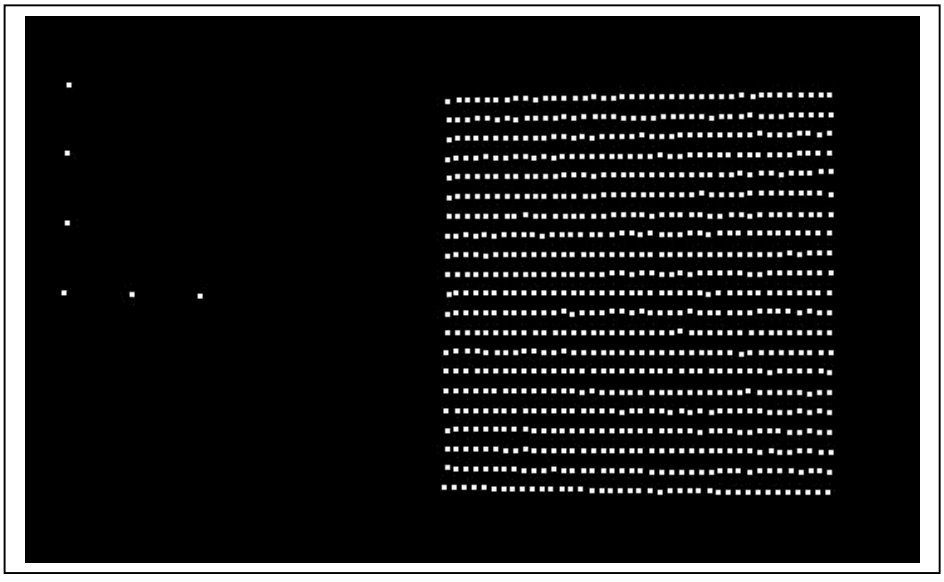

Fig. 3-9: "Point Cloud" of a wrinkled membrane surface (right) as displayed by PhotoModeler® Pro. The six points located to the left of the main point cloud correspond to fixed points used for referencing and calibration.

3.4.2 Targeting Scheme

The goal of this work was to precisely measure the out-of-plane displacements of a thin-film membrane under a uniform tensile load applied at its top and bottom edges. In order to accomplish this task, a suitable targeting scheme had to be developed whereby points on the membrane could be uniquely identified and tracked. The initial idea for targeting was to print an equidistant array of dots across the entire surface of each film sample under study. However, these points were spaced at horizontal distances of 0.2" and vertical distances of 0.4", which did not provide a sufficient number of measurement points to resolve the crests and troughs present in the tensioned film. This is shown in Fig. 3-10, which clearly illustrates the position of the targets relative to the number of vertical wrinkle contours. In order to accurately represent the surface contour, the minimum distance between each target point must be less than one-half the minimum wrinkle wavelength, in conformance with the Nyquist sampling criterion from signal processing:

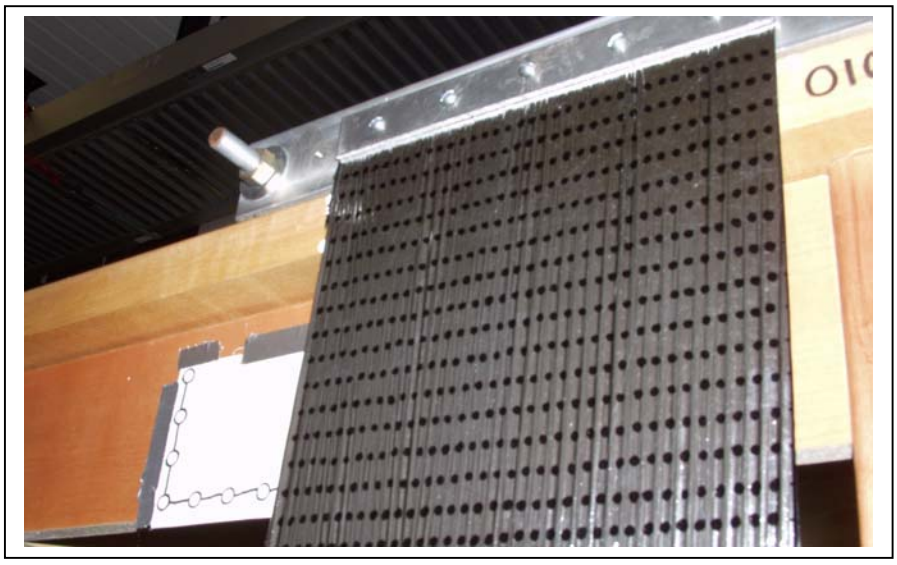

Fig. 3-10: Targets spaced on 0.2" horizontal and 0.4" vertical centers were not close enough together to correctly resolve the wrinkle formation.

$$d_{target} = \lambda \qquad (3\text{-}1)$$

where d_{target} is the distance between the centroids of adjacent horizontal targets, and λ is the apparent **half wavelength** of the tension-induced wrinkle. Note that the vertical

density of the targets was not a major concern as the features of interest induced in the tensioned surface were generally vertical. For this reason, the tensioning experiment was repeated with a more dense population of targets (horizontal spacing 0.1" and vertical spacing 0.2"). However, when the resulting images were processed, the dots were too close together to each be individually resolved by the PhotoModeler® Pro software. Fig. 3-11 shows the dense array of targets. This problem was eliminated by decreasing the diameter of each target while maintaining thin placement, on the same 0.1" vertical centers shown in Fig. 3-12.

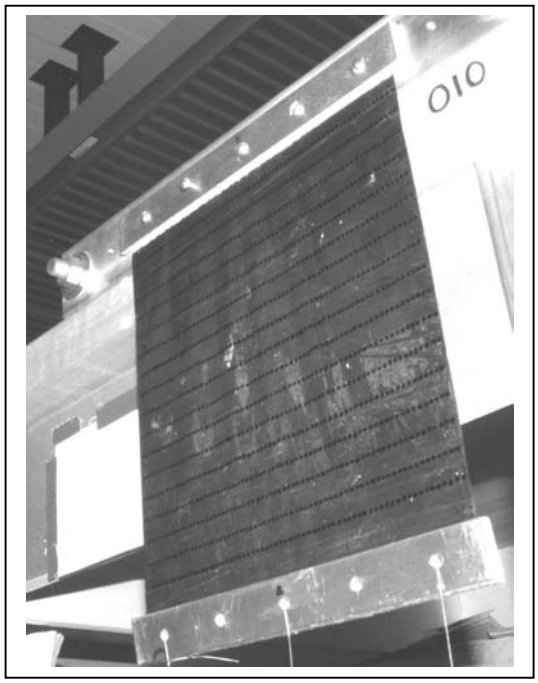

Fig. 3-11: Close-spaced dots could not be resolved by PhotoModeler® Pro.

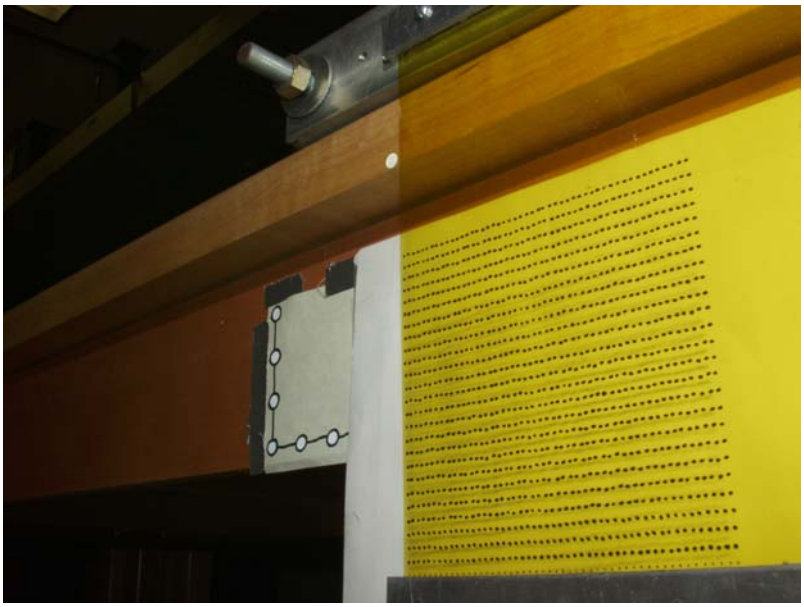

Fig. 3-12: Small targets with horizontal spacing on 0.1" centers and vertical spacing on 0.2" centers.

In order to reduce the total number of targets that required processing while still providing sufficient target density, only a 5" X 5" section of each test article was printed with dots. Assumed symmetry of both the applied tension and the sample geometry enabled results obtained within this region to be extrapolated over the entire membrane surface. This film within this 5" X 5" region was printed with dots using a horizontal and vertical spacing between centers of 0.1" and 0.2", respectively. The targeted film was then tensioned, and imaged by the four stationary cameras. These image sets were then imported into PhotoModeler® Pro for processing and analysis.

3.4.3 Test Article Lighting

Metallized Kapton and Mylar are both highly reflective and even clear non-metal coated membranes can produce unwanted reflections. The dark surface texture of the film apparent in Fig. 3-11 presented additional difficulty while conducting the experiment. This dark surface texture was caused by the film's reflection of the darkness of the room opposite to the film, as well as the reflection of the tube lights installed in the ceiling. Reflective films cannot be illuminated directly, and are best illuminated by indirect lighting. A white cloth was used to cover all parts of the room that were expected to be reflected in the test article when viewed from the vantage point of each camera. This

cloth was spread on the floor behind the imaging cameras and across the ceiling opposite to the test article. High intensity lights were directed towards the cloth material positioned around the perimeter of the work area, as shown in Fig. 3-13.

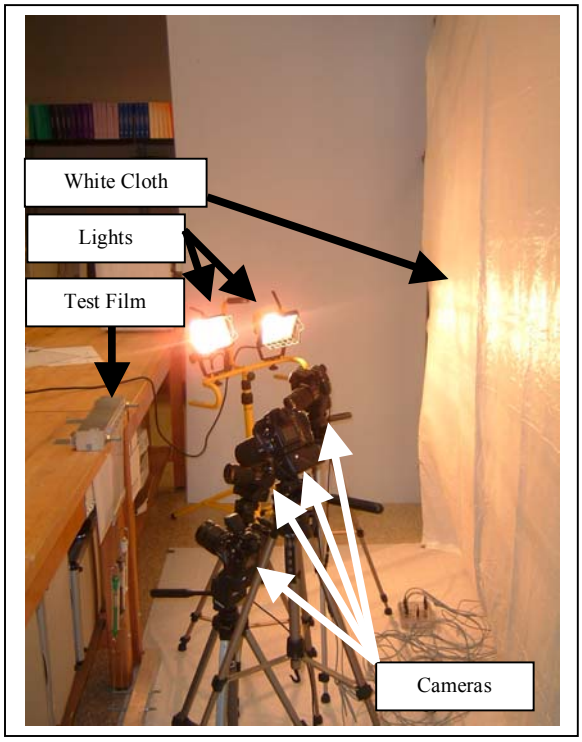

Fig. 3-13: White cloth hung opposite to the film and on floor.

This produced a bright white surface texture on the test article that contrasted with the dark black targets. Fig. 3-14 shows how the contrast between the targets and background was improved by the implementation of the indirect lighting scheme.

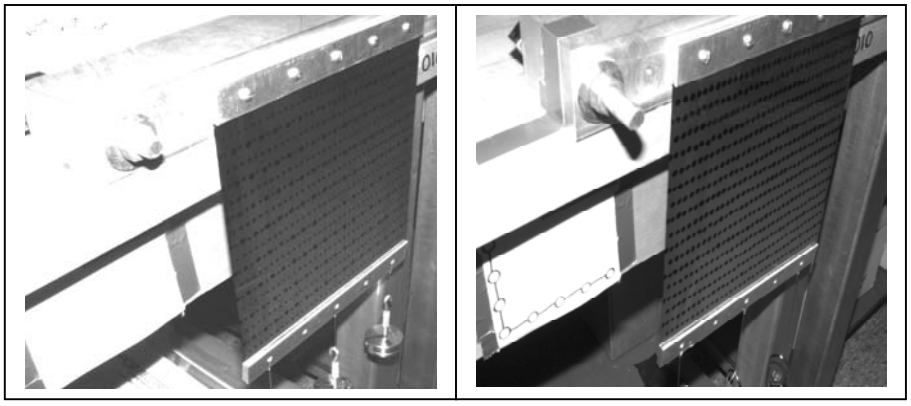

Fig. 3-14: Image of a metal coated Kapton film before and after the indirect lighting scheme was implemented.

3.4.4 Test Article Support and Imaging Sequence

In order to maximize measurement resolution, the image of the test article must use as much of the camera's available field-of-view as possible. Due to the small size of this particular test article, this required cameras to be placed close-in to the test article. This physical constraint made the use of multiple cameras quite difficult, because it was awkward to position them properly in front of the test article. As the arrangement of wrinkles on the surface of a uniformly tensioned membrane only changes as tension is added or removed, it was initially felt that one camera moved to various positions close to the test article, could be used to image the membrane surface. As the surface configuration was expected to remain invariant as the camera was repositioned, it was believed that a high-quality measurement could be obtained with just one camera. This one-camera scheme was used successfully by Thota and Leifer, et al [36].

However, once consecutive images using the single-camera technique were taken and imported into PhotoModeler Pro for this particular application, it was observed that the slight disturbances in air waves caused unintended test article motion; hence it was not possible to back-calculate a unique three-dimensional location that corresponded to a single point identified in each of the two-dimensional images. In order to eliminate any differences in test article position between images, a more conventional approach to close-range photogrammetry, using four stationary cameras triggered simultaneously, was used. The cameras were positioned so that the normal to the imaging plane of each camera was approximately 45^{o} from the normal to the test article surface, and were placed so that their image plane normals were approximately 90^{o} apart (Fig. 3-15).

Even using this more conventional four-camera scheme, problems occurred due to the free hanging test article. Initially, in order to provide a known, in-plane vertical tension within the film, weights were hung in the three holes of the lower stiffener shown in Fig. 3-16. However, this geometry essentially formed an ideal pendulum, and small disturbances in the room caused the masses (and hence the film) to swing. Because the damping in the system was negligible, it was difficult, if not impossible, to reach a state where the film lay motionless. Even though the four cameras were triggered simultaneously, this motion caused blurry images that did not allow the targets to be

resolved. Therefore, the addition of either damping or constraints to the physical set-up was required, in order to eliminate this problem. Constraints were added to the bottom edge of the film in the form of three, spring-loaded "fishing scales," which simultaneously applied tension along the bottom edge of the membrane while remaining anchored to a heavy aluminum block (lower adaptors plate) lying on the floor. In cases where the desired tension was too large to be supported by the weight of the aluminum block, concrete cinder blocks were used on either side to hold the aluminum block to the floor. The spring balance tensioning apparatus is shown in Fig. 3-17, and its operation is described in detail in Section 3-3.

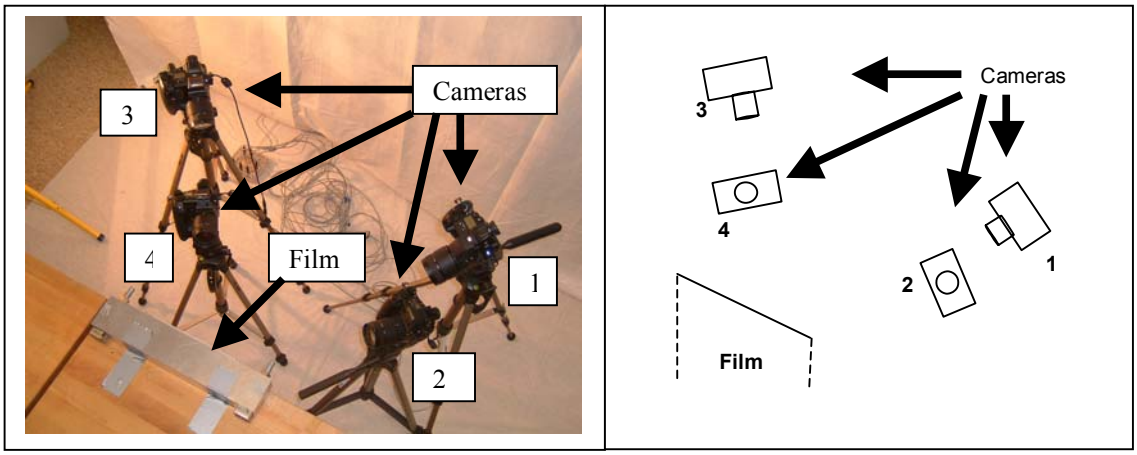

Fig. 3-15: Cameras arranged so that each lens is pointing at 45º angle with respect to the test article.

Fig. 3-16: Tension applied using free weights.

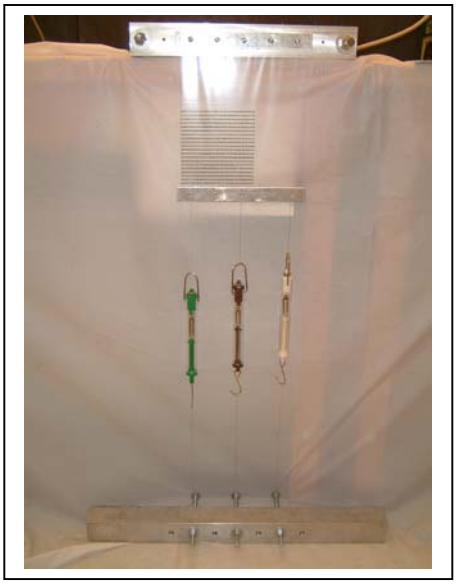

Fig. 3-17: Tension applied using spring-loaded scales.

Camera Calibration is a necessary step when performing optical metrology. In order to compensate for distortions or other image artifacts that stem from the camera optics, the procedure for calibrating the cameras for use with the Photo Modeler Pro software is explained in detail in Appendix A.

3.5 Test Article Assembly

The following items were used to assemble test articles with a 9" X 9" active (wrinkling) area, for tensioning and characterization using photogrammetry. While measurements of the mounting brackets used to support the membrane for this series of experiments, their exact values were not crucial to the success of the experiment. Rather, they were provided as a guideline that will enable others to modify and improve upon this work, if they so desire. Note that the spacing of the holes placed along the membrane edges had to match the geometry of the holes used in the larger "holding bracket," from which the membrane was suspended.

- Al bar (lower adaptor plate), 2" X 2" X 24"; five 0.3" holes drilled and tapped on 1.75" centers (Fig. 3-5).
- 3 spring balances (MacNan Science Supplies) 0-1000 g range
- Fishing line
- 4 flat Al strips, 9" X 1" X 0.13"; five 0.212" holes drilled on 1.75" centers (used as membrane stiffeners) (Fig. 3-2)
- Various samples of thin film membrane material, cut to 9" X 11"
- Upper adaptor plate 15" X 2" X 2.82"; six 0.13" holes drilled and tapped on 1.75" centers (Fig. 3-3)
- Ruler, white office paper, rubber cement, digital scale for weighing samples

3.5.1 Attaching the Membrane Edge Stiffeners

Precise assembly of the test article, which consisted of sandwiching the top and bottom edge of the membrane between the stiffeners made from Aluminum strip stock, was vital, as any misalignment of the stiffeners affected the wrinkle pattern formed in the membrane when tension was applied. Parameters that had the most effect on wrinkling included hole alignment, and "squareness" of the membrane stiffeners (ensuring that the Al strips on the top and bottom of the constrained edge were parallel to each other, and perpendicular to the unconstrained test article edges). In order to reduce the chance of assembly errors, a detailed procedure for test article assembly was developed and closely followed.

All Aluminum components described in Chapter 3 (Fig. 3-2, Fig. 3-3 and Fig. 3-5) were machined to the dimensions specified. Four of the stiffeners machined from the Al strip stock were chosen, and held together to ensure that the centers of all 5 holes aligned. While held in this position, a benchmark line was drawn with the black permanent marker on the top left part of the stack of strips, as shown in Fig. 3-18. Strips used along the top edge of the membrane were marked T1 and T2; and the strips used along the bottom edge of the membrane were marked as B1 and B2, as shown in Fig. 3-19.

The weight of each strip was individually recorded using the digital scale. A T1 strip was placed on the table with the non-marked surface facing upwards, and a layer of rubber cement was applied on the surface of the strip starting from the benchmark point to the other end of the strip as shown in Fig. 3-20. The top edge of the 9" X 11" film was adhered to the top surface of the T1 strip starting from the bench mark point, laying perfectly flat so that no wrinkles formed on the surface of the film. The process was repeated on the bottom edge of the membrane with the B1 strip. A second coating of rubber cement was then applied on the top surface of the film's top and bottom edges. The benchmarks on strips T2 and B2 were aligned with those on the edges of strips T1 and B1, and adhered respectively to the exposed surface of the membrane, along the top and bottom membrane edges, respectively (as shown in Fig. 3-21). After the adhesive had cured for at least five minutes, the membrane could be hung vertically from the top edge stiffeners (T1/T2 strips) by attaching the membrane to the top adaptor plate (Section 3.4.3)

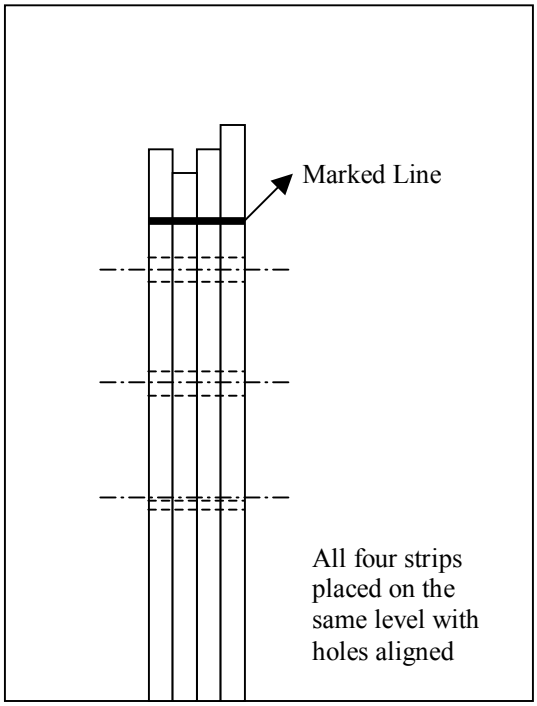

Fig. 3-18: Schematic of drawing a benchmark line used to ensure alignment of the through-holes on the membrane edge stiffeners.

Fig. 3-19: Labeled strips.

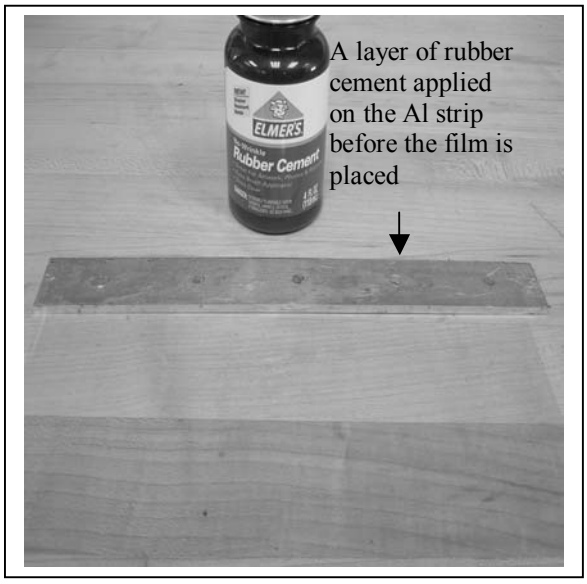

Fig. 3-20: Applying rubber cement to the surface of the strip stiffener.

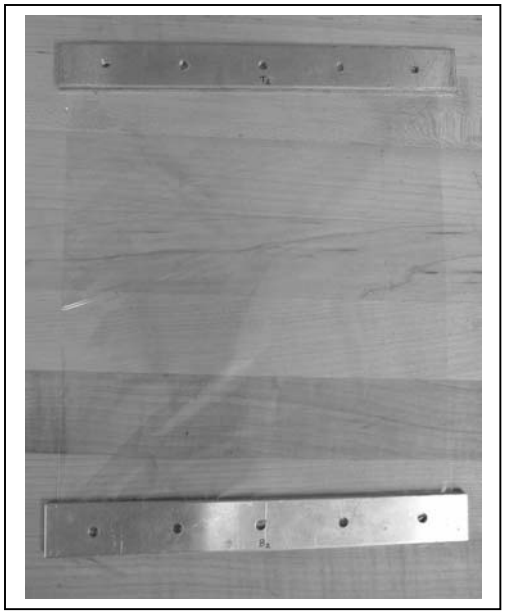

Fig. 3-21: The assembled test article sandwiched between edge stiffeners along the top (T1 and T2) and bottom (B1 and B2) edges.

3.5.2 Printing the Dots on the Membrane

The dense array of targets was generally printed on the bottom left quadrant of the test article. In order to facilitate the placement of dots "by-hand" the test article was oriented as shown in Fig 3-22. To support the membrane, a stack of white office paper equal in thickness to one of the Aluminum strips was placed between the two set of strips, to provide support for the membrane.

To create a template of targets, a plain sheet of 8.5" X 11" paper was placed horizontally on the flat surface. Using the ruler as a guide, dots were marked vertically on the paper at intervals of 0.2 inches over a total range of 5 inches. To create the horizontal rows of targets, the concept of alias frequency was applied here. In this application, the density of the dots used for targeting should always exceed the frequency of the wrinkle formed. For instance, if we know that the approximate wavelength observed when tension is applied to the top and bottom edges of the test article is about 0.5", it is recommended to print a dot at least every 0.125". Note that under the Nyquist criterion,

the minimum acceptable horizontal dot density would be one per 0.25". Using the ruler, a 5" array of horizontal dots spaced at intervals of 0.1" were created adjacent to three points chosen in the vertical array: the bottom point in the array, and two others. The marked sheet of paper was then placed under the membrane so that the vertical line of dots was aligned with the left vertical edge of the membrane, as shown in Fig 3-23. Using the template as a guide, each dot was marked on the film with a fine-point permanent marker, completely filling out the 5" X 5" targeted area, as shown in Fig. 3-24. The dots were bolded (to increase their diameter) with the help of a wider-tipped permanent marker. Finally a sharp instrument was used to pierce through the portion of the membrane that blocked each of the mounting holes along the top and bottom edges. This prepared the test article to allow mounting screws to pass through the edge strips.

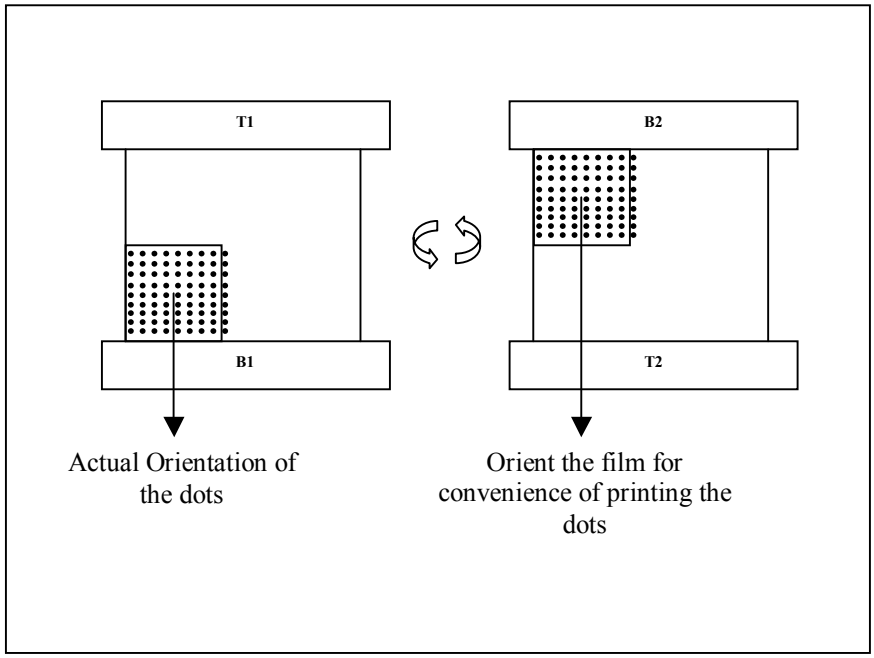

Fig. 3-22: Orientation of the film for convenience of printing the dots.

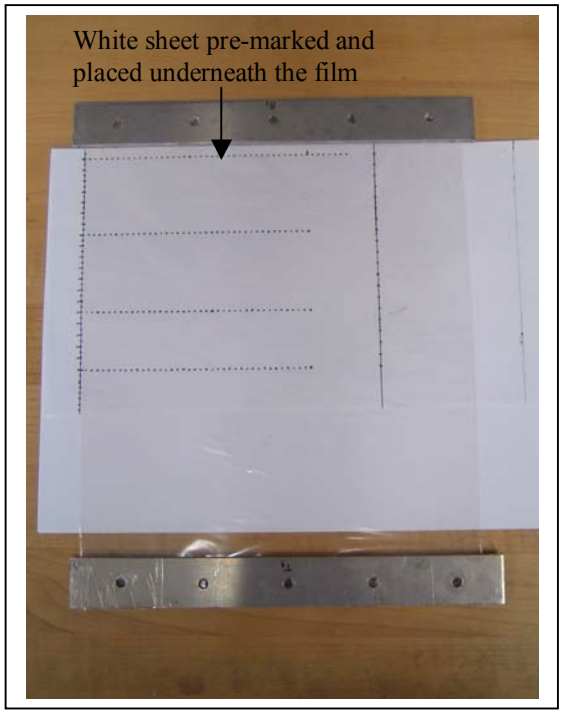

Fig. 3-23: Target template shown under the membrane.

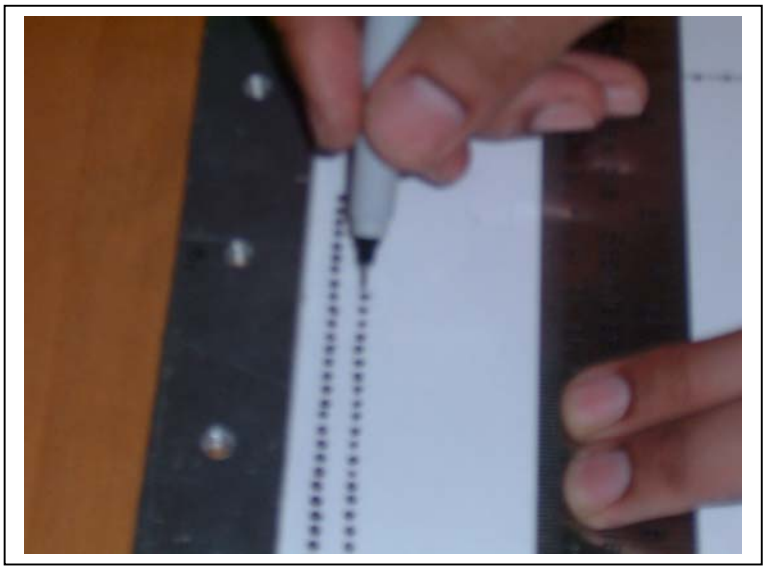

Fig. 3-24: Printing dots.

3.5.3 Mounting and Tensioning the Membrane

The top adaptor plate (membrane holder) was aligned along the front edge of the table top so that its face, containing the threaded membrane mounting holes, protruded

out a bit from the edge of the work surface. This ensured that the film did not contact the table edge during the experiment (Fig. 3-25). The top adaptor plate was secured to the horizontal work surface using adhesive tape. To provide a uniform background (surface texture) for the transparent membrane, standard office paper was used behind the membrane, attached to the edge of the table below the adaptor plate using adhesive tape, so that they hang vertically. Care was taken to ensure that the white sheets were far enough behind the test article to prevent accidental contact. Once the white background was placed, the test article was attached to the top adaptor plate holder by screwing through the holes in the top stiffener strips. The test article was installed so that the film and the lower edge stiffeners hung freely, and so that the dots were oriented along the bottom left corner of the test article. The heavy aluminum bar (bottom adaptor plate) was secured to the floor using adhesive tape. It was placed so that the face containing the 3/8" holes was oriented vertically, and aligned with the front face of the test article and top adaptor plate. The 3/8" carriage screws were inserted into the bottom adaptor plate from the rear, and the front of the screws were secured with nuts. For the test article used in this experiment, the second, fourth and sixth holes were used to engage the test article (through the spring balances), as shown in Fig. 3-26. Fishing line was attached to the back of each of the carriage screws (using strong knots), leaving about 10" of line on each. The other end of each fishing line was tied to one of the three spring balances, as shown in Fig. 3-27. Another fishing line was attached between the top end of each spring balance and the bottom edge stiffener on the test article, as shown in Fig. 3-28. When attaching the fishing lines to the test article, holes were chosen in the bottom edge stiffeners that preserved vertical orientation of each spring balance (Fig. 3-28). Excess fishing line was trimmed. The complete set up (to this point) is shown in Fig. 3-29.

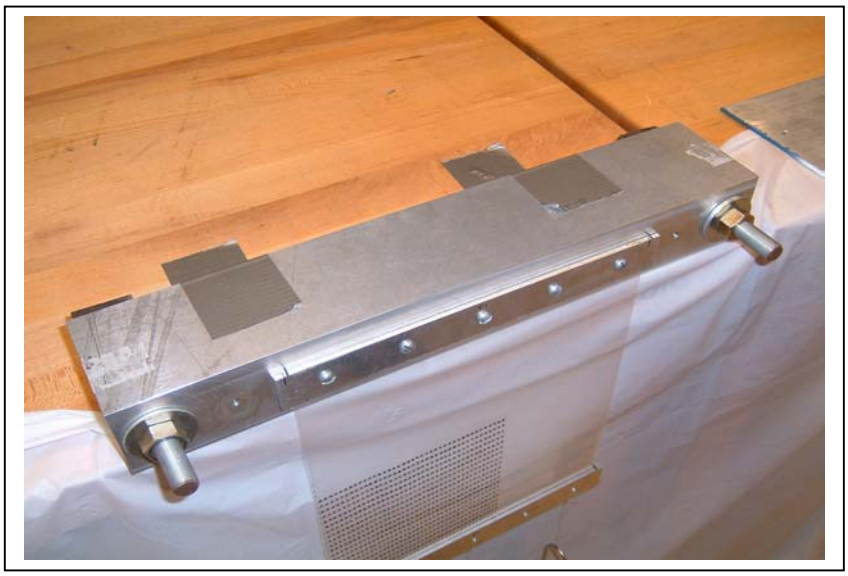

Fig. 3-25: Positioning the stiffener holder (upper adaptor plate). Note the sheet of office paper placed behind the transparent test article membrane.

Fig. 3-26: Carriage screws on the Aluminum block (lower adaptor plate). Note the fishing line attached to each carriage bolt.

Fig. 3-27: Carriage screws to spring balance connections.

Fig. 3-28: Spring balance to lower membrane edge stiffener connections.

A single-hole punch was used to create retro-reflective dots from a sheet of adhesive-backed retro-reflective material. These dots were used to create a coordinate system on a 5" X 5" sheet of graph paper. After a point was chosen to serve as origin, additional dots were distributed at one inch intervals in the X (horizontal) and Y (vertical) directions on the graph paper. This sheet was mounted adjacent to the test article, and served as a fixed reference plane for the photogrammetry process. It was positioned so that it could be readily viewed from the perspective of all four cameras (Fig. 3-30). In order to increase contrast between the retro-reflective targets and the graph paper, the targets were outlined using a black marker. This helped improve the photogrammetry reconstruction, as it permitted the software to locate the centroid of each retro-reflective target more accurately.

Fig. 3-29: Complete set up

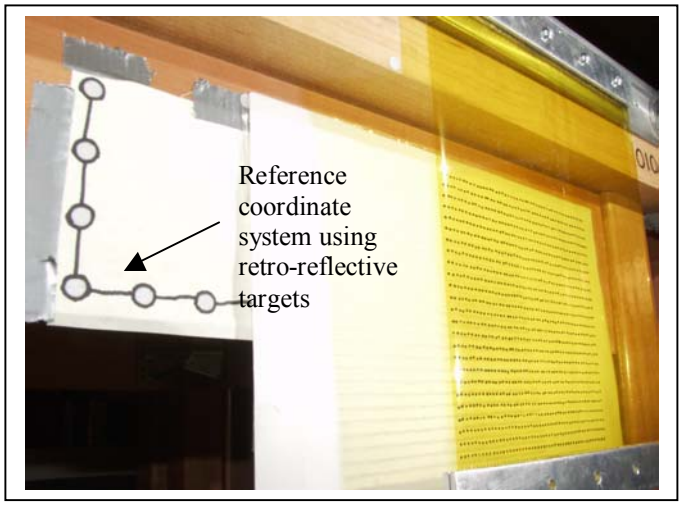

Fig: 3-30: Position of the coordinate system sheet with respect to the film as seen from Camera 2.

3.6 Conducting the Experiment

Items required:

- White sheets for draping workspace (to provide indirect reflective lighting)
- Calibrated digital cameras (Olympus Camedia Model number E-20N, 5.0 Mega Pixel), and associated accessories (Fig. 3-31 shows the 4 cameras labeled)
- Junction box for simultaneous triggering
- Tripods (one for each camera)
- Work lights (for illuminating work space)

3.6.1 Camera Placement and Background

Sheets were dropped around the workspace (sides, ceiling, and floor), to prevent seeing reflected objects in the test article (from the perspective of each camera). The membrane was pre-tensioned by adjusting the carriage screws until each spring balance read 50 g. Camera 2 (pre-labeled on the camera and camera box) was loaded with the battery corner and turned on. The camera was set up as follows:

- Removed the front cap

- The camera was set to manual mode by turning the knob at the bottom left corner at the front.
- Turned the focal length lens ring completely clockwise when facing behind the camera until it reads 9.
- The camera was set to infinite focus by turning the front wheel a couple of turns in the far direction.
- The camera was set to manual exposure.
- Pushed the flash button so that the flash unit popped up.
- Camera speed was set greater than 80 by turning the knob located on the top right corner of the camera in front of the camera's click switch.

Camera 2 was loaded on to one of the tripods and placed on the lower left corner position so that the focal axis was oriented approximately 45˚ with respect to the test article (Fig. 3-15). The camera and tripod were positioned to maximize the size of the image within the camera's field of view. The process was repeated for cameras 1, 4 and 3, which were respectively placed at the top left, bottom right and top right corner positions as shown in Figs. 3-31 and 3-15. The remote shutter release jack in each camera was connected to a junction box that allowed one remote trigger to simultaneously operate up to six cameras (Fig. 3-32). For proper test article illumination, the work lights (Fig. 3-33) were shined on the draped sheets, rather than directly on the test article. Following this approach, a bright, white, reflected image was produced in the membrane when viewed from the perspective of each camera. This bright white surface texture increased the contrast of each target (inked dot) on the membrane, which in turn increased the accuracy of the photogrammetric reconstruction.

3.6.2 Obtaining Membrane Images

Images of the test article were made simultaneously by using the cable release trigger. To ensure that each of the cameras triggered properly, the image on each of the cameras was checked after exposure by displaying it using each camera's play mode. This also helps to ensure that the lighting was adequate to illuminate the targets on the test article. In cases when the lighting was insufficient, either the work lights were repositioned or the individual strobe flash units on each camera were used to improve the contrast. All images were transferred via USB cable from the on-board micro drives to a laptop PC, into a folder named <trial #_film type _ thickness _ weight>, where "film type" was either polyimide (Kapton) or Mylar, thickness was provided in µm, and weight

was the total applied spring force in grams. (Note that although technically incorrect, the spring scales were calibrated when manufactured using units of mass (g) instead of units of weight (N).) As each camera assigns its own names to each image, they were all renamed using the labels *top left, bottom left, top right* and *bottom right* for pictures in Cameras 1, 2, 3 and 4 respectively, once they were transferred to the PC. After a satisfactory set of images was obtained, the tension on the test article was increased, in order to determine the effect of applied tension force on membrane wrinkling. A complete matrix of test article parameters and applied tensions is provided in Table 3-1. Once each series of experiments was completed (low to high tension), the carriage bolts were loosened, to release the tension in both the membrane and the spring balances. This was to minimize the likelihood of introducing a permanent offset in the spring balances.

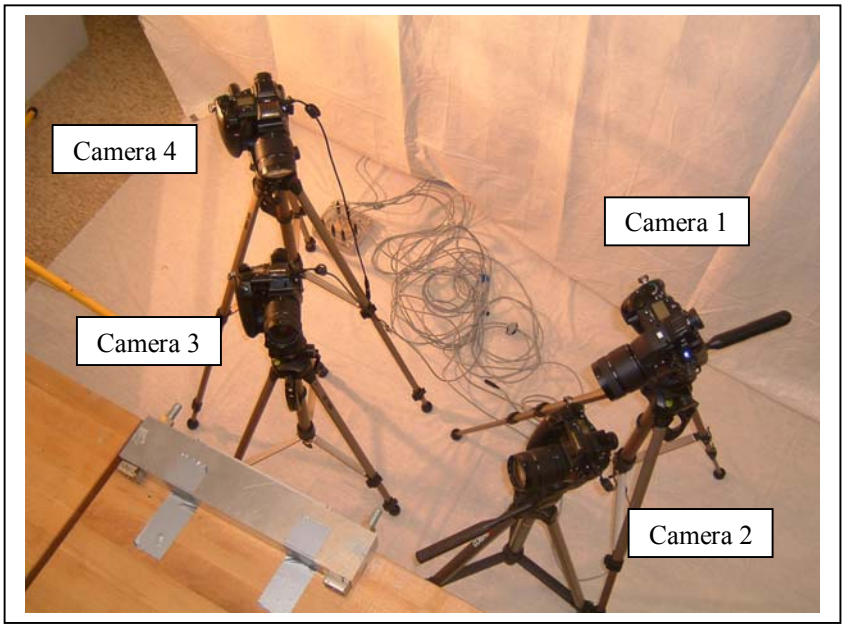

Fig. 3-31: Camera positions. The test article is located directly below the upper adaptor plate visible in lower-left corner.

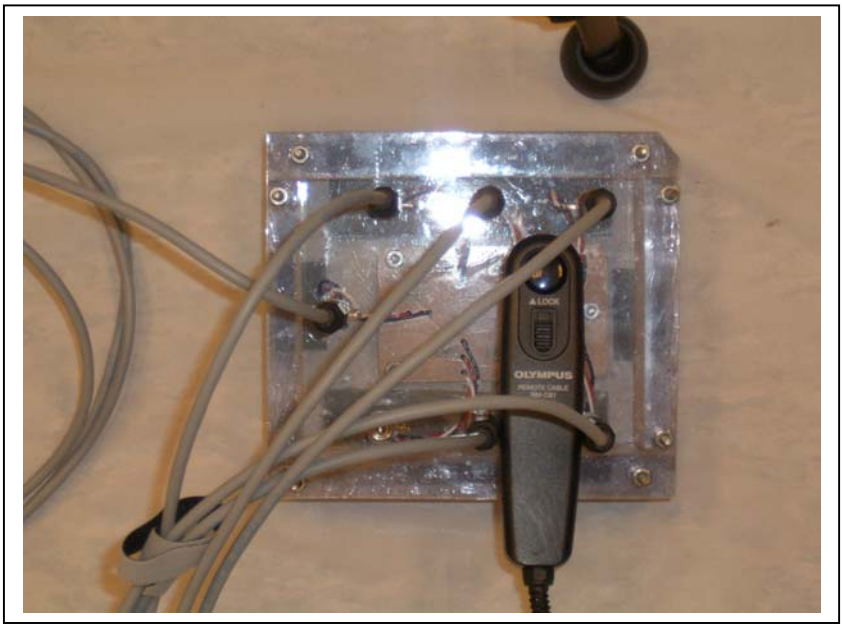

Fig. 3-32: Trigger junction box.

Fig. 3-33: Work lights.

		Tensions applied (in Newtons)						
Film Type	Thickness (μm)	Set-up 1	Set-up 2	Set-up 3	Set-up 4	Set-up 5	Set-up 6	Set-up 7
Kapton	7.62	2.4	3.4	3.8	4.8	5.8		
Kapton	12.7	1.9	2.4	2.9	3.4	3.9	4.4	
Mylar	12.2	1.4	1.9	2.4	2.9	3.4	3.9	4.4
Mylar	23.4	1.4	1.9	2.4	2.9	3.4	3.9	4.4

Table 3-1: Matrix of test article parameters and applied tensions.

3.7 Image Reconstruction using PhotoModeler® Pro

3.7.1 Introduction

PhotoModeler® is a photogrammetric software package used to reconstruct the three dimensional shape of an object from two dimensional images. The images taken from all camera locations are imported into the software. High-contrast dots and coordinate points (targets) are recognized by the software, which calculates the centroid of each target using any one of a number of standard schemes. Once each of the targets have been located in each image, they are cross-referenced to each other, which means that points in each image corresponding to the same physical target on the physical test article are identified as being the same. Once this process has been completed, the software can calculate the location of each target point on the test article through a triangulation process. In this process, the software uses known parameters such as the camera focal lengths, and calculates the x, y and z values of each target location and tabulates them. The user can then export the data for further analysis or visualization. The following sections provide the detailed step-by-step procedure followed during the series of experiments.

3.7.2 Transferring Photos into Reconstruction Software

On the new project window, a standard PhotoModeler project was selected. Measurement units were selected as inches and approximate size of images was selected as 20”, which was the appropriate field of view shown in figs. 3-14 and 3-16. Since the cameras used for the project were calibrated, the “calibrated camera” option was chosen,

along with the location of the calibration files. (Note that camera calibration is done by imaging a test pattern provided by the software company and then following their specified procedure.) Each calibration file contains information that allows PhotoModeler to account for physical variations inherent in the optics of each Camera. Project images were chosen by selected using the "add remove images" button and the "change directory" icon to move to the directory in which the images are stored. By manually choosing one photo from the required folder, all the corresponding images automatically were selected. "All >>" was clicked to transfer the pictures into the software. "O.K.", "Next" and "Finished" were respectively clicked to close the New Project window. The selected photos appeared on the left menu. The properties window of each image was opened and the calibration files corresponding to each image were loaded to set the properties of the image to reflect their respective cameras. This is an important, yet easily missed step, for if the correct calibration file is not used for each image, the accuracy of the three-dimensional reconstruction is reduced. The PhotoModeler project file was saved under folder name < film type _ thickness _ weight> under the same file name, and updated regularly in order not to lose any data.

3.7.3 Sub Pixel Marking

Photo Modeler has a special feature called the sub-pixel marking tool. Sub-pixel interpolation algorithms calculate the x-y coordinates of the geometric center of high contrast circular targets [38], with much greater resolution than suggested by the ± ½ pixel resolutions normally attained based on the image pixel density. Using the sub-pixel marking tool, the user can click anywhere in the center of the target and drag to encompass the target, and the software will automatically calculate the geometric center of an ellipse (circular targets look elliptical in pictures due to the viewing angle of the camera) with resolution approaching one-tenth of a pixel [38] (Fig. 3-34). The point is then assigned a unique identification number [38]. This is an important feature because the software can recognize dark circles on a light background or vice versa without actually requiring the user to guess and mark the center [38]. Human operators are usually accurate to about one to three pixels, while the present version of the software used has the ability to automate the sub-pixel marking while still achieving resolution of

up to one-tenth of a pixel [38]. Here, this improved resolution is vital as very small changes in surface configuration of each membrane are being documented by this technique.

To complete the marking process, zoomed views were used for better target visibility. The "sub-pixel target mode" from the "Marking menu" was selected to avail the dragging option described. In the image, the center of each target was spotted and while mouse down, the selection box was dragged out to enclose the target. Removing the mouse allowed the centroid of the target to be found with sub-pixel resolution. The process was repeated until all targets and coordinate points were marked. The complete process was repeated for each image used in the three-dimensional surface reconstruction.

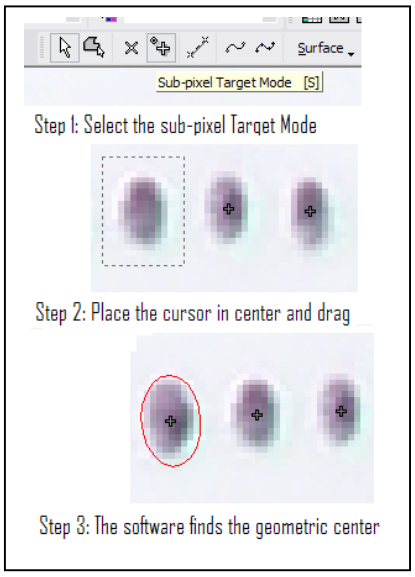

Fig. 3-34: Sub-pixel marking tool in PhotoModeler. Note the selection box (top-left) encompassing the mark, and the resulting ellipse (bottom-left) found by PhotoModeler®. The plus shaped marks represent the centroid of each ellipse calculated by the software.

3.7.4 Target Point Cross-referencing

The next step in the process is called "referencing". Referencing reassigns a common point in four images with the same identification number so as to virtually unite them to be one [38]. The user must initially reference at least 10 points and process them

using the software's in-built bundle adjustment algorithm [38]. The bundle adjustment algorithm measures the 3D coordinates with its associated precision errors. It also computes the exact location and orientation of each camera [38]. Once these initial points have been referenced, the software semi-automates the process, by projecting an "epipolar line" (shown in Fig. 3-35), which is a ray of projected light, on the second image once a point has been selected in the first image [38]. This epipolar line originates from the location in space corresponding to the location of the camera that produced the image. Based on the currently calculated camera position, the target in the second image corresponding to the one in the first should be located along the epipolar line. Once this point has been referenced in the second image with the help of the epipolar line, the software automatically places the cursor on the corresponding target in the third and fourth images, to click and reference, the moment they are opened [38]. Verification of the calculated target locations must be accomplished by clicking on them with the mouse. It would always be efficient to reference a few points at a time and process them using the bundle adjustment algorithm to avoid any reference errors committed by the user [38].

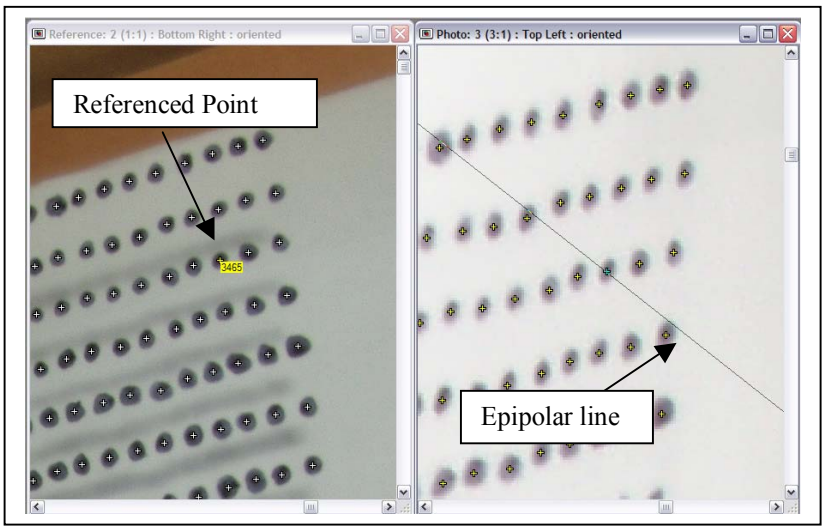

Fig. 3-35: Epipolar line that helps referencing in PhotoModeler®. The location (in the right photo) of the point marked on the length will be found somewhere along the epipolar line shown.

Regarding complete details of the referencing process, the reference mode was selected by clicking on the double X symbol on the Mode box or selecting Reference

mode from the referencing menu (shown in Fig. 3-36). The software randomly selected two of the images and displayed them in order to start the referencing process. The left window always contains the source image (the image containing the points that serve as reference) and the right window contains one of the images with the points to be associated to those in the reference image. In the source image, one of the sub-pixel marks that required referencing was selected and the cursor was then moved to the destination image (right window). The corresponding sub-pixel mark was selected in the destination image, which then changes color to show that it had been referenced. The next destination image was then displayed, and the process was repeated. This whole process was repeated for all the sub-pixel points on the upper edge of the targets array on the membrane. The "Process" icon was then selected from the project menu or by clicking the "running man" symbol in the "Mode" box. A window, depicted in Fig. 3-37, then popped up. If there were no major suggestions other than those to select more marks on the images, or if the list of points with quality problems numbered less than 5, the referenced points were processed. As mentioned earlier, it is generally best to process only a few referenced points at a time. After referencing, if a window popped up with suggestions pertaining to reference errors, or unusually large residual values, the selected points were unreferenced and the process was repeated for those points. Otherwise, the process of referencing and processing was repeated row by row, until all rows were completed done. To check on the 3D locations calculated by PhotoModeler, the 3D Viewer window could be opened from the "Project" Menu or by clicking the "screen" icon beside the "tables" icon. In the 3D viewer options menu that appeared, the "Cam Stations" option was highlightened so that the locations of the cameras could be seen in the 3D display window. Along with the calculated camera locations, the image in the 3D viewer window showed the locations of all referenced points. Since all of the target points were essentially located in the plane of the membrane, any inconsistencies such as points calculated to be significantly above or below the membrane surface, could be immediately noted and corrected. A typical 3D viewer image is shown in Fig. 3-9.

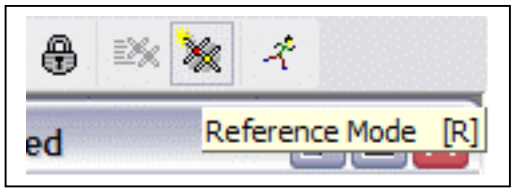

Fig. 3-36: Reference mode available in the menu of PhotoModeler®. (Icon highlighted by a square border)

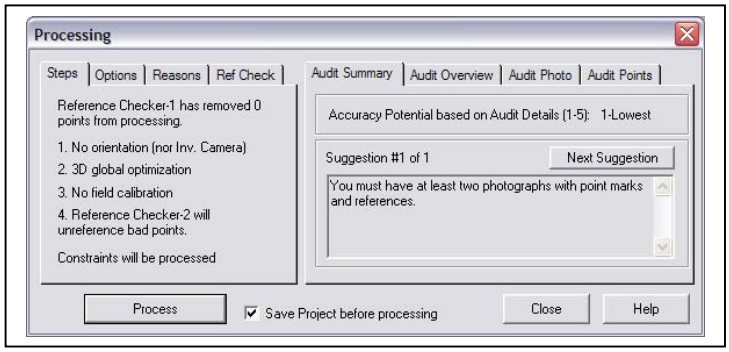

Fig. 3-37: Processing box with the suggestions box to the left in PhotoModeler®.

3.7.5 Automatic Referencing Option

Once the process of referencing has been performed manually on about 5% of the total targets (each represented by a unique sub-pixel mark in each of the four images), the software has the capability of automatically referencing all the remaining points in each of the images. Fig. 3-38 shows the automatic reference window in PhotoModeler.

The Automatic Referencing tool is invoked by selecting it from the "Referencing" menu. Initially, the search distance was set to 0.001 inches (Fig. 3-38). The distance is usually set to a very low number in order to minimize the possibility of misreferencing points. The "Execute Referencing" button was used to perform the referencing operation (Fig. 3-38). After referencing, the 3D viewer was used to check the quality of the referencing. This quick visual check was performed to make sure that all the points located by PhotoModeler were either on the film or on the coordinate points. If there were any inconsistent points, they were selected and unreferenced using the "Ctrl U" command. After checking and unreferencing all poorly-referenced points, the automated process was repeated using an increased search distance of 0.002, a value which was increased even further until all the points were referenced. For this particular work, there

were typically only 4 points in the project that were left unreferenced after the automated process was complete. These points were therefore referenced manually.

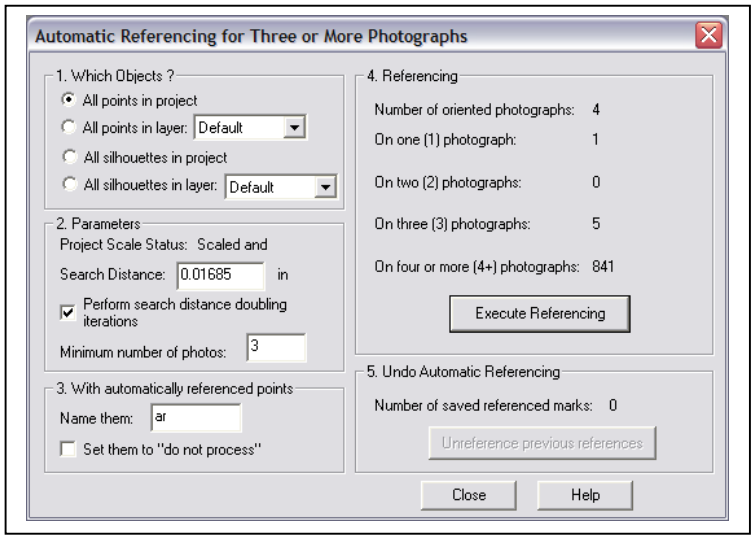

Fig. 3-38: Automatic referencing window in PhotoModeler®.

3.7.6 Project Scaling

The 3D viewer was used to view all of the targets in 3D space; the point cloud shown in the 3D viewer was neither scaled nor oriented after the completion of the referencing process. Therefore a separate scaling and orientation procedure was required. This was done by defining X, Y and Z coordinate directions, as well as a physical scale and an origin. Based on what parameters are provided, the locations of all points are properly reported with respect to the user-defined origin, coordinate axes and scale. In order to provide fixed points to serve as a reference frame, each image used contained a set of fixed points averaged so that (1) the distance between each point was known. (2) the vertical column of targets defined the Y-axis; and (3) the horizontal row of targets defined the X-direction. This fixed set of targets is shown in Fig. 3-10, and their depiction in the PhotoModeler 3-D viewer is shown in Fig. 3-9. Using the array of fixed targets, PhotoModeler required the user to select two points to define each axis. The software defined the axis orientation as directed from the first to the second point chosen. Fig. 3-39 shows the “scale rotate” window in Photo Modeler, which is used to set the coordinate directions, origin and scale of the model.

With the 3D viewer showing the fixed coordinate points open, the “Scale/Rotate” option was selected from the “Project” menu. Generally, the origin was set first, by

clicking on the “Translate” tab. This was done by choosing the point that would serve as the origin in the 3-D viewer, and then clicking “Define”. Completing this operation successfully turned the selected origin point green. The model was scaled by clicking on the “Scale” tab, and entering “1 inch” for the distance. This corresponded to the physical distance between the origin and the point to its immediate right. These two points were chosen, in order, in the “3D view” window. Finally, checking on the “Rotate” tab allowed the coordinate directions to be defined. The two points used to scale the project were selected to define the X-axes; the origin, and the point immediately above it were defined in the model as the Z-axis. Based on these selections, PhotoModeler automatically defined the orientation of the Y-axis to coincide with that found in the typical right handed Cartesian coordinate system.

After the model was satisfactorily oriented and scaled, the 3-D coordinates of all the points were exported to a spreadsheet from which they were sent to visualization software for further analysis. This was done by selecting the “Point table” option from the “Tables” menu. The “Coordinates” option was selected from the menu found in the top-left portion of the window. The items were sorted according to their X-coordinate by clicking on the header of the x-coordinate column. Once the point file was exported using the “Table Export” option, the PhotoModeler project was saved and then closed. Figure 3-40 shows the point table window containing the 3D location of each point in the project.

Note: Each time “Save” was clicked, the software automatically created a back up file with <file name_Ver#>. Each file containing a specific version number is an archived version of the project, while the most up-to-date version consisted of the file-name only.

Once the error in the PhotoModeler reconstruction has been reduced to an acceptable level, the point cloud representing the surface of the test article can be best visualized using other 3D plotting packages, such as Surfer (Golden Software) or even Microsoft® excel. As stated previously, PhotoModeler data can be exported for use in other applications by selecting *table, export* from the menu bar.

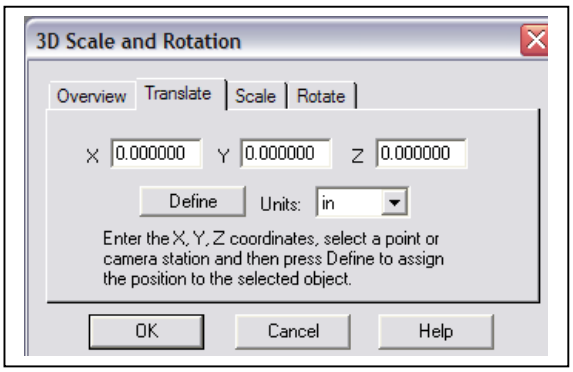

Fig. 3-39: Scale/Rotate window in PhotoModeler®.

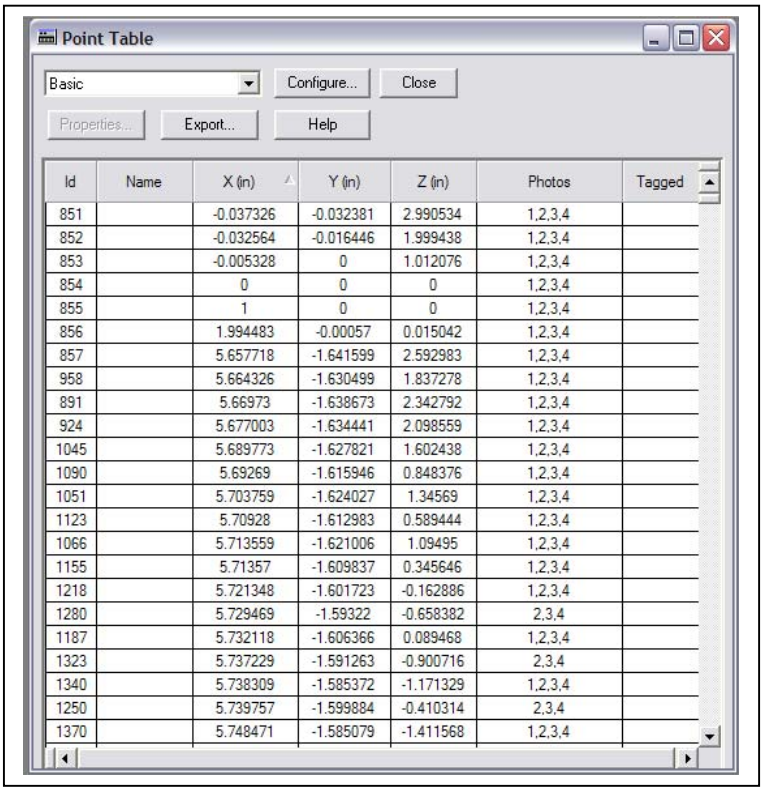

Id	Name	X (in)	Y (in)	Z (in)	Photos	Tagged
851		-0.037326	-0.032381	2.990534	1,2,3,4	
852		-0.032564	-0.016446	1.999438	1,2,3,4	
853		-0.005328	0	1.012076	1,2,3,4	
854		0	0	0	1,2,3,4	
855		1	0	0	1,2,3,4	
856		1.994483	-0.00057	0.015042	1,2,3,4	
857		5.657718	-1.641599	2.592983	1,2,3,4	
958		5.664326	-1.630499	1.837278	1,2,3,4	
891		5.66973	-1.638673	2.342792	1,2,3,4	
924		5.677003	-1.634441	2.098559	1,2,3,4	
1045		5.689773	-1.627821	1.602438	1,2,3,4	
1090		5.69269	-1.615946	0.848376	1,2,3,4	
1051		5.703759	-1.624027	1.34569	1,2,3,4	
1123		5.70928	-1.612983	0.589444	1,2,3,4	
1066		5.713559	-1.621006	1.09495	1,2,3,4	
1155		5.71357	-1.609837	0.345646	1,2,3,4	
1218		5.721348	-1.601723	-0.162886	1,2,3,4	
1280		5.729469	-1.59322	-0.658382	2,3,4	
1187		5.732118	-1.606366	0.089468	1,2,3,4	
1323		5.737229	-1.591263	-0.900716	2,3,4	
1340		5.738309	-1.585372	-1.171329	1,2,3,4	
1250		5.739757	-1.599884	-0.410314	2,3,4	
1370		5.748471	-1.585079	-1.411568	1,2,3,4	

Fig. 3-40: Point table in PhotoModeler®.

3.8 Visualizing the Wrinkled 3D Membrane Surface

3.8.1 Importing data into Surfer and Removing Extraneous Points

Surfer 8, by Golden Software, is the package that was used to fit a surface on to the three-dimensional point cloud produced by PhotoModeler. It has a unique function that returns equidistant X-value points, or grid data, that best fits the surface points provided. This allows a surface to fit even to areas of the point cloud containing sparse data. However, this means that extraneous points, including those corresponding to the fixed coordinate axes, had to be eliminated before the surface was fit.

The point table file exported from PhotoModeler was opened in Surfer. The file essentially looked like an Excel sheet. The first three rows contained labels that were exported from PhotoModeler, as shown in Fig. 3-41. These were deleted as extraneous. The first column contains the labels for each point generated by PhotoModeler. These, too, were eliminated. The Y axis and Z axis labels were swapped. The Z axis described by PhotoModeler should be preferably labeled as the Y axis. We were only interested with these and the X axis points in our analysis. Since these were the only two directions used in our analysis and PhotoModeler has little flexibility offered when it comes to defining axis the required way, the axis names were swapped in Surfer. Rows 2 to 7 of the numeric data contained points related to the coordinate system attached to the left of the film. The use of the coordinate system is only to orient and scale the data in the PhotoModeler®. Since this purpose had already been served, rows 2 through 7 were deleted. The file was saved as a Golden software data file with the label <File name _ TableExport>.

3.8.2 Plotting the Data

In order to visualize the three-dimensional surface of the film, the "Plot" document feature in Surfer was used. A "New" file was opened as a Plot document to plot the data saved the "Data" option in the grid menu was selected to import the data from the edited spreadsheet. The grid data window appeared as shown in Fig. 3-42. The file "Table Export" in the Golden software data format was opened in the grid data window. The Y axis and Z axis positions were swapped. The grid data function returned interpolated values of the surfer deflection over equal intervals of x that best fit the surface imported. The Surfer-Report 1 window was closed and not saved as it was not required. The "Surface" option was selected on the "Map" Menu, and a 3D map was

displayed that corresponded to the surface configuration of the wrinkled membrane (Fig. 3-43). Using the 3D trackball option, the map was rotated to better observe the orientation and amplitudes of the surface contours. Note that at least one surface wrinkle is easily observed using the view showed in the figure. The file was saved under the name <file name _ final plot>.

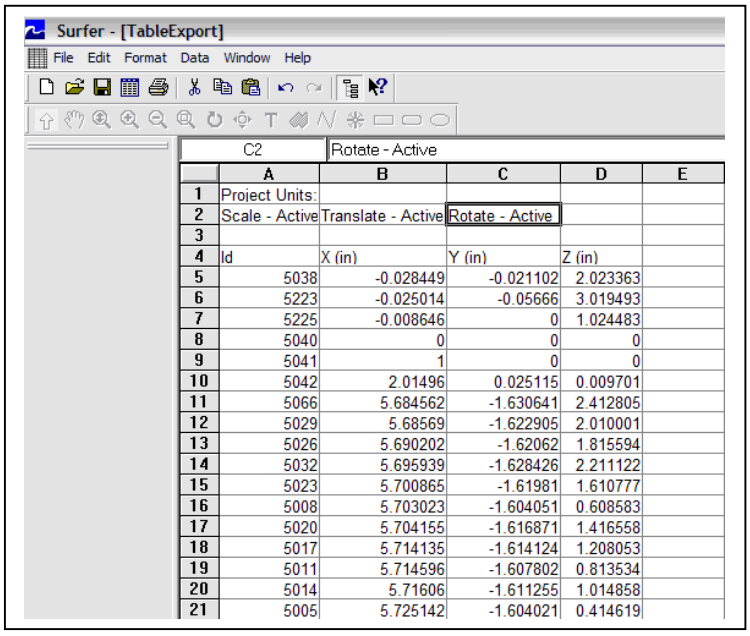

	A	B	C	D	E
1	Project Units:				
2	Scale - Active	Translate - Active	Rotate - Active		
3					
4	Id	X (in)	Y (in)	Z (in)	
5	5038	-0.028449	-0.021102	2.023363	
6	5223	-0.025014	-0.05666	3.019493	
7	5225	-0.008646	0	1.024483	
8	5040	0	0	0	
9	5041	1	0	0	
10	5042	2.01496	0.025115	0.009701	
11	5066	5.684562	-1.630641	2.412805	
12	5029	5.68569	-1.622905	2.010001	
13	5026	5.690202	-1.62062	1.815594	
14	5032	5.695939	-1.628426	2.211122	
15	5023	5.700865	-1.61981	1.610777	
16	5008	5.703023	-1.604051	0.608583	
17	5020	5.704155	-1.616871	1.416558	
18	5017	5.714135	-1.614124	1.208053	
19	5011	5.714596	-1.607802	0.813534	
20	5014	5.71606	-1.611255	1.014858	
21	5005	5.725142	-1.604021	0.414619	

Fig. 3-41: Exported data as it looks in Surfer software.

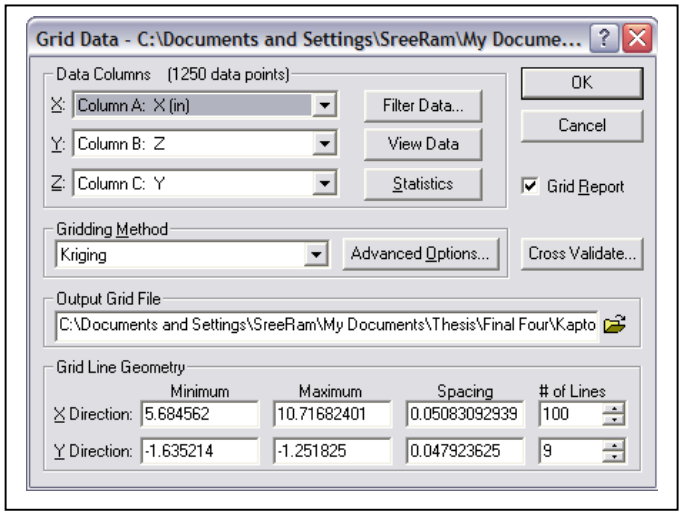

Fig. 3-42: Grid data function window in Surfer software.

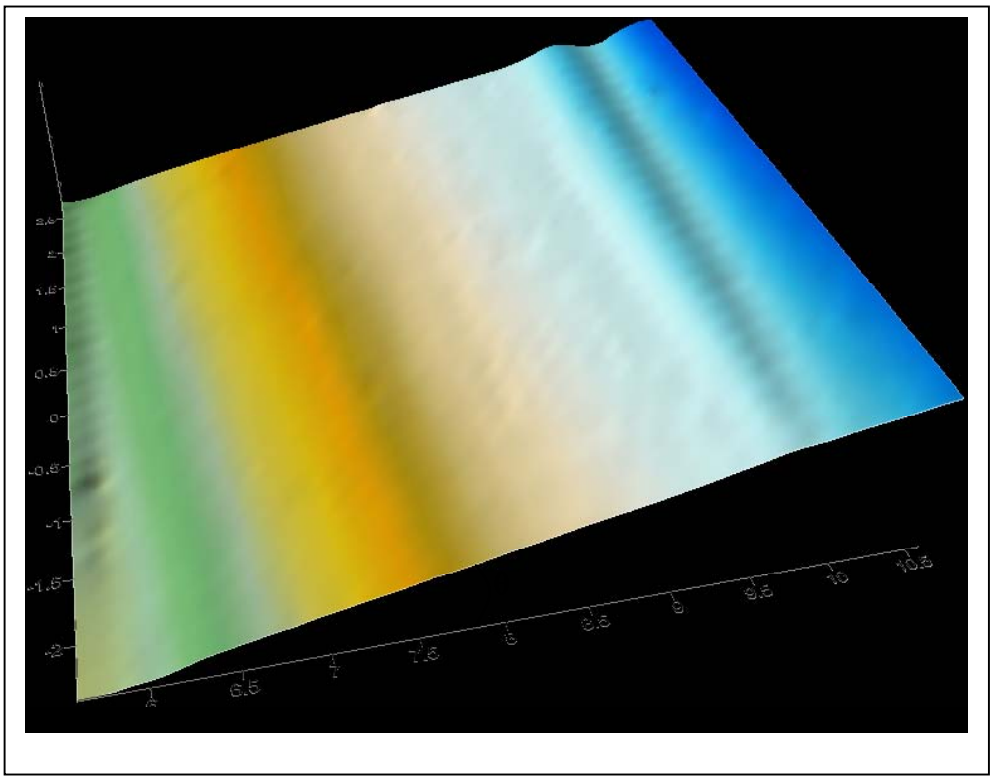

Fig. 3-43: 3D plot of wrinkled membrane surface as shown by the Surfer software.

Chapter 4: DATA ANALYSIS

4.1 Introduction

The objective of this experiment was to determine the dependence of tension-induced wrinkle amplitude and wavelength on material parameters, thickness, and applied tensile load. The cases tested and photographed experimentally are listed in Table 3-1.For each combination of parameters, average wavelength and amplitude were determined as follows: Using the sorted "grid" data from Surfer (that was fit to the raw, experimental data), two random rows of dots near the middle of the film were selected. The X and Z values for these corresponding points were exported and plotted. It was initially found that the points were centered along a line that was rotated with respect to the X-axis. A coordinate transformation was used to eliminate this rotation, and the resulting graph was then plotted and printed. Using a ruler, specific values of wavelength and amplitude found on the graph were measured to obtain a range of wavelengths and amplitudes for each specific case. Details pertaining to each step in the process are found in the following sections.

4.2 Exporting Data to Microsoft® Excel

As discussed previously, the Surfer software fit a tight grid of points to the surface defined by the raw data in the table-export file, using a "kriging" algorithm. For each case, the Surfer grid file that read <TableExport _ file name> was opened, and resaved The file was saved under the file type "ASCII XYZ data" as an excel file. This enables the software to export a set of points to the excel file saved.

4.3 Extracting Relevant Rows

In a separate window, the PhotoModeler file corresponding to the case under evaluation was picked to allow selection of rows of interest. Selection was aided by zooming the points for visibility in the 3D viewer window of PhotoModeler. Using the "measure" option on the top menu in PhotoModeler (Fig. 4-1), the range of Z values were recorded for the particular row selected. In the excel sheet saved as described in the

previous section, the data were stored in a single column (as ASCII text) and therefore required some reformatting using the “text to columns” option in the “data” menu. X and Y values corresponding to the range of Z values (there may be more than one) noted were copied into a separate sheet in the same file. The sheet was named as <file name _ fft _ row#>.

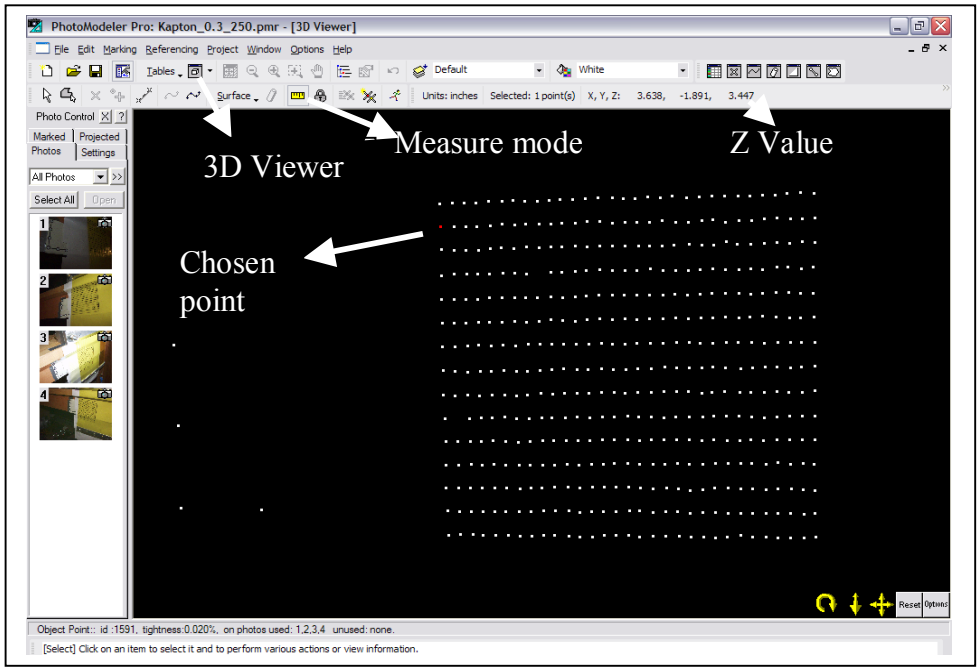

Fig. 4-1: Choosing rows to extract corresponding points.

4.4 Translating the Coordinates

In order to measure the amplitude and wavelength of the wrinkles, it is important to plot them using a scale that maximizes the detail visible on the graph. It is obvious that it would be easier to measure the amplitudes and wavelengths in Fig. 4-2 than Fig. 4-3, although both these graphs represent the same wave. In order to align the plot with the X-axis (and allow the detail to be magnified), the data must be transformed so that the X-axis is physically aligned with the plane of the membrane. This rotational transformation compensates for the misalignment between the hanging membrane and the reference axes that were present in the physical set up. This was done as follows: First the untransformed data, consisting of the X and Y values corresponding to the range of Z

values above were plotted. The resulting plot had a positive slope associated with it. With the help of the "display equation" option, the slope of the graph was noted. The angle of inclination, θ, formed due to the slight variations in the manual orientation of the film during the experimental set-up, was then calculated with the help of slope. The X and Y-axes were then rotated by this angle θ using Eq. 4-1, so that the wave form appeared parallel to the X-axis. The transformed graph looks as shown in Fig. 4-3.

$$X' = X\cos\theta + Y\sin\theta$$
$$Y' = -X\sin\theta + Y\cos\theta \qquad \text{(Eq. 4-1)}$$

Where θ= ATan $^{-1}$(Slope of the trend line)

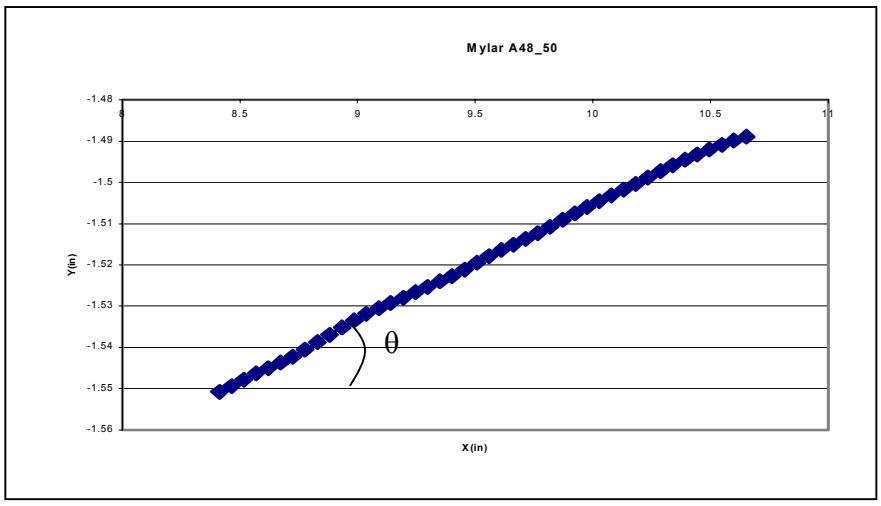

Fig. 4-2: X and Y values plotted before the transformation of the axes for a 0.48 mil (12.19 μm) thick Mylar film under a tension of 1.445 N.

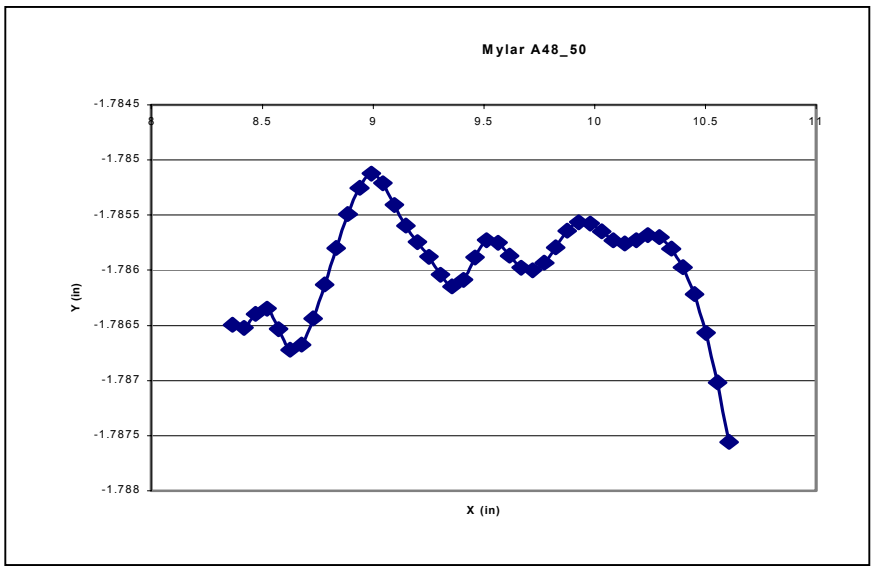

Fig. 4-3: X and Y values plotted after the transformation of the axes for a 0.48 mil (12.19 μm) thick Mylar film under a tension of 1.445 N.

4.5 Wavelengths and Amplitudes

Fig. 4-3 shows the profile of wrinkle across the cross section of a film. As we can see, the wave was not consistent, as one would expect, since both its amplitude and wavelength seem to vary. Hence, it was not possible to characterize the wave using simple observation; therefore, another method was used. Mechanical measurement was used. To find the range of wavelengths and amplitudes which were later analyzed to remove any outliers. This was done as follows: The graph shown in Fig 4-3 was moved to a separate excel sheet enlarged to fill an 8.5 X 11 sheet of paper, and printed. Using a physical ruler, the X-axis and Y-axis were scaled on the printed graph. For example, if the distance between 1.98" mark and 1.982" mark on the Y-axis was 26 mm on the ruler, the scale of the graph to ruler on the Y-axis would be $7.69 \text{ X } 10^{-5}$ inch/mm (0.002 inch / 26 mm). The consecutive crests and troughs on the graph were marked with a pencil and the vertical and horizontal distances between them were measured with the ruler. The vertical distance between a consecutive crest and trough was, theoretically, twice the amplitude. Hence the measured values were halved and tallied. Similarly, the horizontal distance between any consecutive crest and trough was, theoretically, half the wavelength of the wave. Hence, the measured values were doubled and separately tallied. The tallied measurements were then multiplied using their respective scales to determine the values of amplitudes and wavelengths in inches. This process was repeated for all the different test cases.

4.6 Outliers

Some of the measured values of amplitude were found to be as low as 0.0001", which is less than 6 μm. Wrinkles of this amplitude are not visible to human eye. However, the wrinkles we have observed during the experiment were clearly visible to the human eye. The waves corresponding to these low amplitudes generally had smaller wavelengths. Hence, a proper threshold value of amplitude was estimated, which roughly corresponded to all wrinkles that were visible to human eyes. All the values below that threshold were removed as outliers. A similar exercise was performed to identify and weed out the lower wavelength values from the data available.

4.7 Trend charts

The above process was repeated for each of the test cases for the four films. The values for amplitudes and wavelengths were tabulated for each film on separate sheets. For each of the applied tensile forces, the average wavelength and amplitude were calculated. Also, the standard deviation for the data set for each force were calculated and tabulated. Two additional columns for the lower limit (average wavelength/ amplitude – standard deviation) and the upper limit (average wavelength/ amplitude + standard deviation) were calculated. Table 4-1 shows a sample table of the amplitude calculations for the 0.48 mil (12.19 µm) thick Mylar film. Graphs were plotted for the average amplitudes/ wavelengths, upper limits and lower limits for all the test cases for each film against force in Newtons. Fig. 4-4 shows a sample graph for a 0.48 mil (12.19 µm) thick Mylar film. The graph shows that the trend of the average amplitude decreases with the increase in force. This was also true with the trend of the average wavelength to the force applied. Table 4-2 tabulates the average amplitudes and wavelengths along with their ranges and standard deviations for all the graphs.

Mylar 48	Force (N)	Multiplier	Mean (in)	Mean (m)	SD (in)	SD (m)	Lower limit	Upper limit	Sample Values			
Case 1	1.4	0.0000273	0.0006518	0.0000166	0.0001979	0.0000050	0.0000115	0.0000216	29	18.75		
									0.00079	0.00051		
Case 2	1.9	0.0000273	0.0005392	0.0000137	0.0001158	0.0000029	0.0000108	0.0000166	16.75	22.75		
									0.00046	0.00062		
Case 3	2.4	0.0000156	0.0003686	0.0000094	0.0002034	0.0000052	0.0000042	0.0000145	37.5	12.5	12.5	32
									0.00059	0.00020	0.00020	0.00050
Case 4	2.9	0.0000086	0.0002521	0.0000064	0.0000885	0.0000022	0.0000042	0.0000086	22.5	26.75	23.5	44.5
									0.00019	0.00023	0.00020	0.00038
Case 5	3.4	0.0000156	0.0002496	0.0000063	0.0000728	0.0000018	0.0000045	0.0000082	10.75	16.5	14.75	22
									0.00017	0.00026	0.00023	0.00034
Case 6	3.8	0.0000125	0.0002016	0.0000051	0.0000899	0.0000023	0.0000028	0.0000074	18.5	10.25	25.25	10.5
									0.00023	0.00013	0.00032	0.00013
Case 7	4.3	0.0000172	0.0001408	0.0000036	0.0000519	0.0000013	0.0000023	0.0000049	3.75	9.25	3.75	10.5
									0.00016	0.00016	0.00006	0.00018

Table 4-1: Amplitude calculations for a 0.48 mil (12.19 µm) thick Mylar film.

Fig. 4-5 summarizes the graphs for amplitudes for Mylar films of thickness 0.48 mil (12.19 µm) and 0.92 mil (23.4 µm). Fig. 4-6 summarizes the graphs for wavelengths for Mylar films of thickness 0.48 mil (12.19 µm) and 0.92 mil (23.4 µm). Fig. 4-7 summarizes the graphs for amplitudes for Kapton films of thickness 0.3 mil (7.62 µm) and 0.5 mil (12.7 µm). Fig. 4-8 summarizes the graphs for wavelengths for Kapton films of thickness 0.3 mil and 0.5 mil.

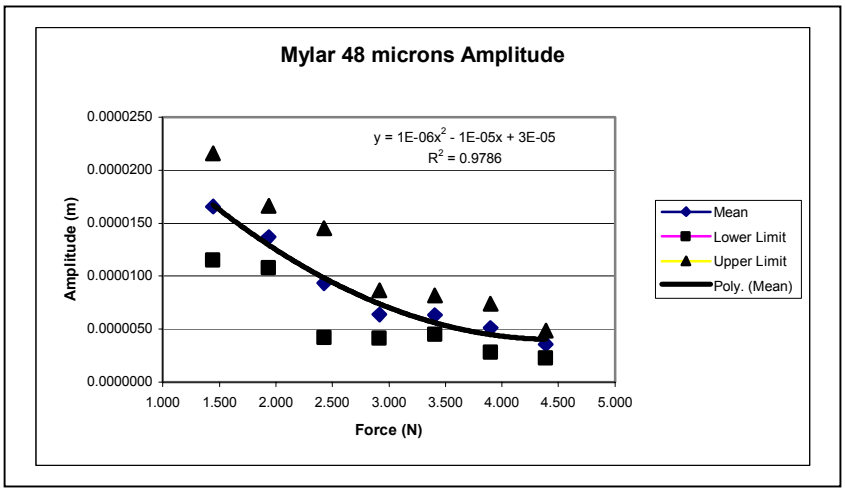

Fig 4-4: Sample graph that shows the trend of amplitude to force for a 0.48 mil (12.19 µm) thick Mylar film.

Mylar 0.48 mil thick film							Mylar 0.92 mil thick film						
Force	Avg. Amplitude	Lower Limit	Upper Limit	Avg. Wavelength	Lower Limit	Upper Limit	Force	Avg. Amplitude	Lower Limit	Upper Limit	Avg. Wavelength	Lower Limit	Upper Limit
(N)	(m)	(m)	(m)	(m)	(m)	(m)	(N)	(m)	(m)	(m)	(m)	(m)	(m)
1.446	0.0000166	0.0000012	0.0000216	0.01631	0.01303	0.01959	1.446	0.0000158	0.0000063	0.0000253	0.01919	0.00967	0.02872
1.936	0.0000137	0.0000108	0.0000166	0.01533	0.01108	0.01957	1.936	0.0000161	0.0000059	0.0000262	0.01499	0.00872	0.02126
2.426	0.0000098	0.0000057	0.0000138	0.01457	0.01181	0.01734	2.426	0.0000106	0.0000084	0.0000127	0.01344	0.00888	0.01801
2.917	0.0000064	0.0000042	0.0000087	0.01182	0.01025	0.01340	2.917	0.0000104	0.0000055	0.0000153	0.01139	0.01063	0.01215
3.407	0.0000063	0.0000045	0.0000082	0.01248	0.01132	0.01364	3.407	0.0000106	0.0000053	0.0000160	0.01175	0.00683	0.01667
3.897	0.0000051	0.0000028	0.0000074	0.01120	0.00886	0.01355	3.897	0.0000092	0.0000056	0.0000128	0.01226	0.00601	0.01851
4.388	0.0000036	0.0000023	0.0000049	0.01217	0.00952	0.01483	4.388	0.0000078	0.0000048	0.0000108	0.01376	0.00980	0.01772
Kapton 0.3 mil thick film							**Kapton 0.5 mil thick film**						
Force	Avg. Amplitude	Lower Limit	Upper Limit	Avg. Wavelength	Lower Limit	Upper Limit	Force	Avg. Amplitude	Lower Limit	Upper Limit	Avg. Wavelength	Lower Limit	Upper Limit
(N)	(m)	(m)	(m)	(m)	(m)	(m)	(N)	(m)	(m)	(m)	(m)	(m)	(m)
2.426	0.0000213	0.0000213	0.0000213	0.01225	0.00689	0.01760	1.936	0.0000192	0.0000144	0.0000240	0.01429	0.01318	0.01540
3.407	0.0000192	0.0000146	0.0000237	0.01001	0.00844	0.01159	2.426	0.0000191	0.0000141	0.0000240	0.01351	0.01158	0.01544
3.897	0.0000167	0.0000160	0.0000175	0.01113	0.01053	0.01174	2.917	0.0000186	0.0000146	0.0000225	0.01294	0.00863	0.01726
4.878	0.0000146	0.0000114	0.0000179	0.01156	0.01046	0.01265	3.407	0.0000185	0.0000113	0.0000257	0.01222	0.00934	0.01511
5.859	0.0000075	0.0000052	0.0000099	0.01066	0.00905	0.01226	3.897	0.0000160	0.0000118	0.0000202	0.01171	0.00990	0.01353
							4.388	0.0000127	0.0000126	0.0000128	0.01107	0.00887	0.01327

Table 4-2: Average amplitudes and wavelengths for all test cases and their ranges using one standard deviation.

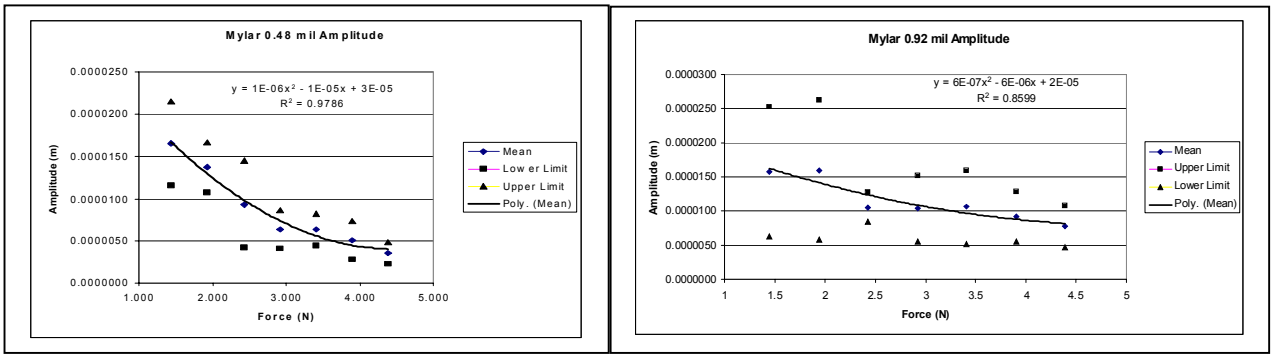

Fig. 4-5: Graphs for amplitudes for Mylar films of thickness 0.48 mil (12.19µm) and 0.92 mil (23.4 µm).

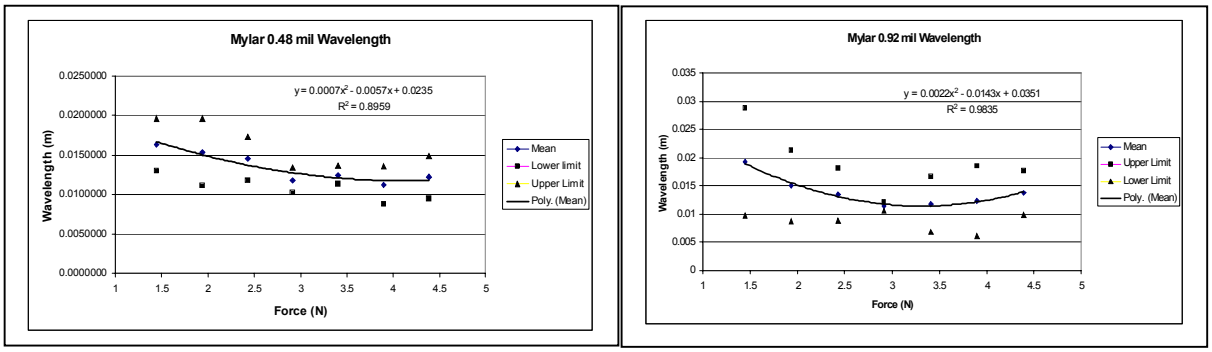

Fig. 4-6: Graphs for wavelengths for Mylar films of thickness 0.48 mil (12.19 µm) and 0.92 mil (23.4 µm).

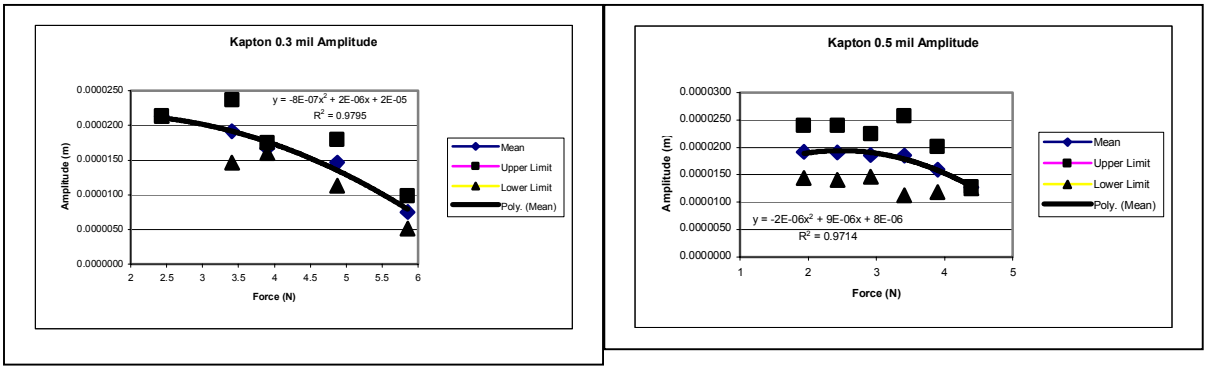

Fig. 4-7: Graphs for amplitudes for Kapton films of thickness 0.3 mil (7.62 µm) and 0.5 mil (12.7 µm).

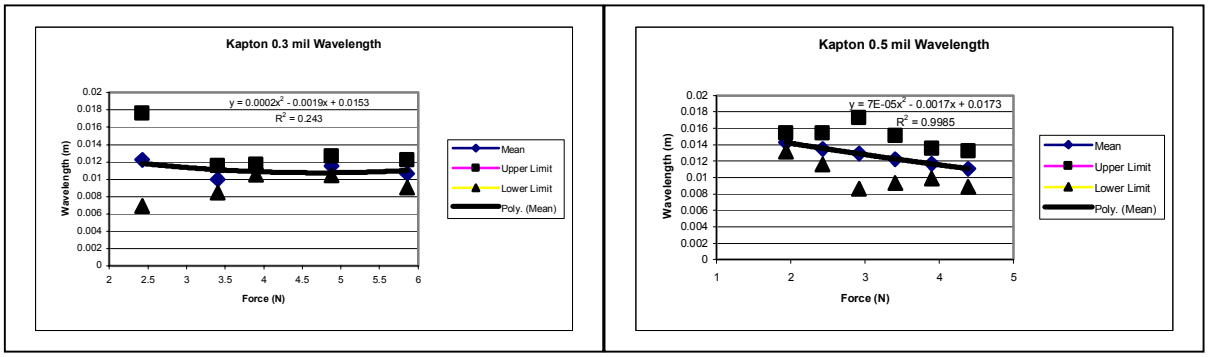

Fig. 4-8: Graphs for wavelengths for Kapton films of thickness 0.3 mil (7.62 µm) and 0.5 mil (12.7 µm).

4.8 Conclusion

While a commercial code like Matlab could have been used to process and analyze the data, the "by hand" analysis method chosen for use here was believed to be the most efficient way to determine the wavelengths and amplitudes because the outliers might end up being considered a part of the analysis. This was so, in part, to ensure that all outliers were eliminated. Increased confidence in the results reported here could be obtained by utilizing additional data from rows of points on the membrane not analyzed. Even more improvement could be obtained by extending the region of targets to the complete width of the membrane. Finally, the same experiments can be repeated on Kapton and Mylar materials of same thickness and dimensions under similar tensile forces to improve the accuracy of the measured values.

Chapter 5: DISCUSSION OF EXPERIMENTAL RESULTS

5.1 Introduction

The experimental measurements described in the previous chapter show that the wrinkles that form across the surface of the membrane depend, in part, on the applied tensile force, as well as the physical characteristics of the membrane (e.g. thickness, material parameters). In this chapter, these measurements will be compared with preliminary results of a numerical simulation. Additional insight will be provided by examining the Föpple – von Kármán equations, fundamental relations that govern the mechanical response of thin membrane structures. Results found in the literature that solves the F. – von K. equations for geometry similar to that studied here will be discussed. Both the numerical work and the new theoretical results strongly imply that strain along the boundary (in the lateral direction), a parameter that could be independently varied in the experiments described in the previous chapters, likely plays a major role in both wrinkle amplitude and wavelength. Shortcomings of the existing apparatus, as well as improvements that could enable it to be used to vary lateral boundary strain will also be discussed.

5.2 Effect of Various Factors on Amplitudes and Wavelengths

As observed in Fig. 4-5 and Fig. 4-7, the amplitudes of the wrinkles decreased with the increase in the tension loads. A similar trend of decrease in wrinkle wavelength as tension load was increased is depicted in Fig. 4-6 and Fig. 4-8. Although trend lines were fitted to the data presented in these figures, these experimental results do not necessarily establish that tensile load (as well as thickness) are the only parameter that affects the wrinkle pattern.

Wrinkle amplitude was plotted as a function of load for Kapton films of 0.3 mil (7.62 μm) and 0.5 mil (12.7 μm) thicknesses (Fig 5-1). As we can see, it is observed that the amplitudes decreased more quickly with applied tensile force for the 0.3 mil thick

films than they did for the 0.5 mil (12.7 μm) thick film placed under the same loading configuration. A similar trend was also observed for Mylar film (Fig. 5-2), where the wrinkle amplitudes for the 0.48 mil (12.19 μm) thickness showed a stronger (inverse) dependence on applied tensile force than the 0.92 mil (23.4 μm) sample did.

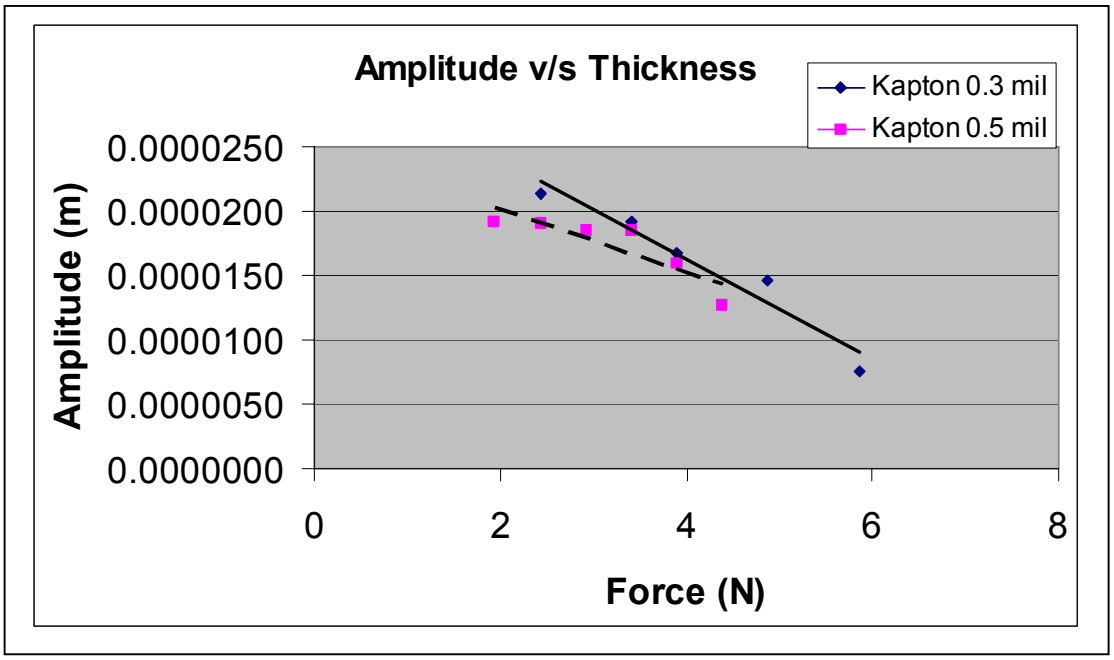

Fig. 5-1: Comparison of amplitudes for different loads for a 0.3 mil (7.62 μm) thick Kapton film and a 0.5 mil (12.7 μm) thick Kapton film.

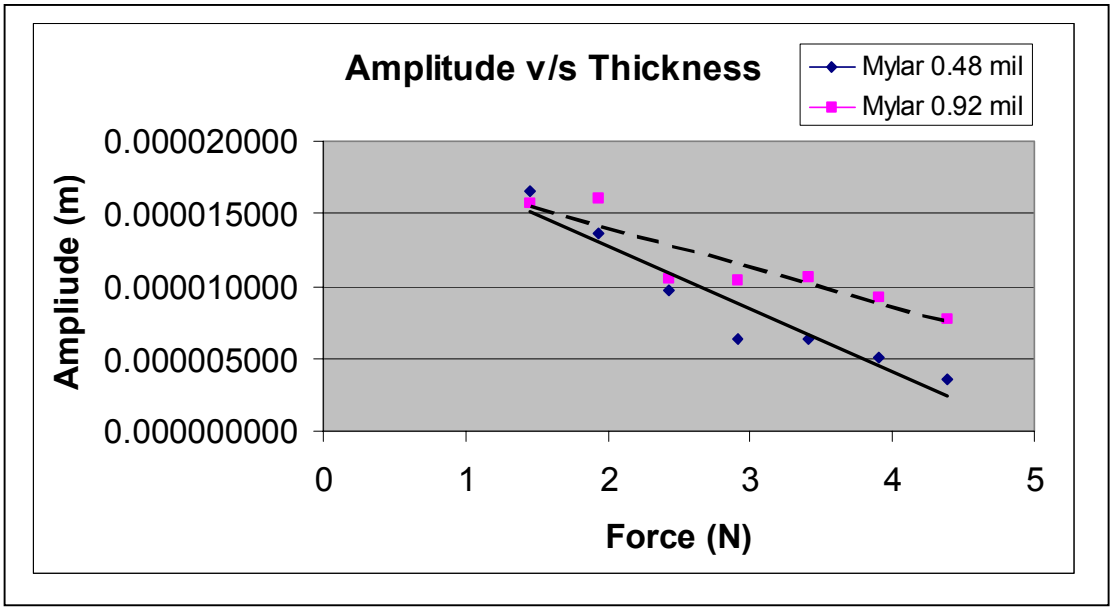

Fig. 5-2: Comparison of amplitudes for different loads for a 0.48 mil (12.19 μm) thick Mylar film and a 0.92 mil (23.4 μm) thick Mylar film.

Fig. 5-3 and Fig. 5-4 show that although the effect of thickness (independent of applied tension) on wavelength is very weak, thicker films do tend to have higher wavelengths than thinner films. In other words, the thickness of the film appears to be inversely related to the wavelength of the film.

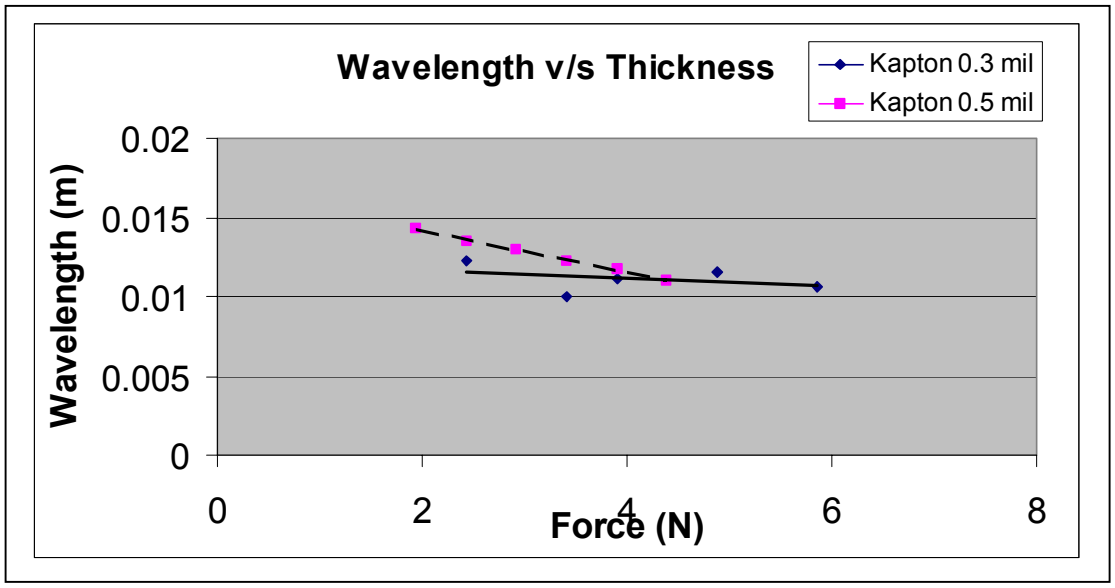

Fig. 5-3: Comparison of wavelengths for different loads for a 0.3 mil (7.62 µm) thick Kapton film and a 0.5 mil (12.7 µm) thick Kapton film.

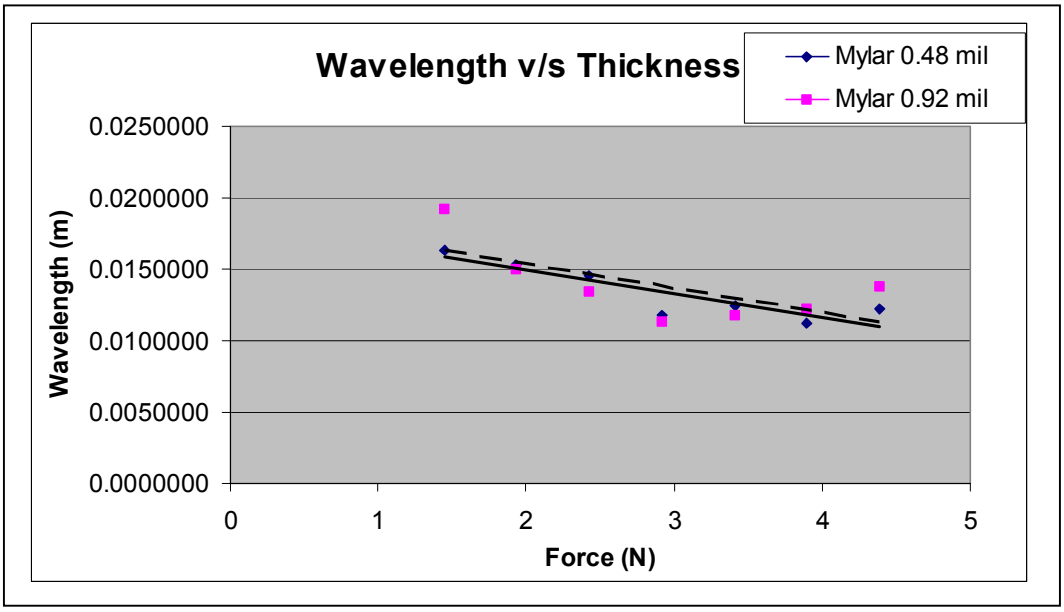

Fig. 5-4: Comparison of wavelengths for different loads for a 0.48 mil (12.19 µm) thick Mylar film and a 0.92 mil (23.4 µm) thick Mylar film.

5.3 Intent of Application in the Experiment

The initial plan of this research was to design a capacitive sensor to measure the amplitude of wrinkles on the film. The intent was to place a single distributed capacitive sensor array over the film, where the film acts as a parallel plate of the capacitor and local capacitance would change array based on the local distance between the sensors and film at different points. This would have allowed the out-of-plane displacements on the film to be measured. This idea did not work because of the accuracy and precision of capacitive sensors. Additionally, fabrication complexity prohibited this idea from being carried out.

A non-contact measurement system was vital to carry out the work performed here. As mentioned previously, the film is sensitive to even a light breeze. During the conduct of the experiment, it was very difficult to achieve a stable equilibrium. Even the slightest airwaves caused by situations like closing a door would create disturbance that would further disrupt the experiment.

The above stated conditions thus provided the challenge of finding a measurement system that would be highly precise and does not touch the test article. Photogrammetry was the right choice due to the availability of the above features in a single package. Photogrammetry can measure with precision of the order of μm. Accuracy of up to 1:20,000 is possible with amateur cameras which makes it possible to measure miniature sized objects much more accurately than most of the measurement systems.

5.4 Some References in the Literature to the Effect of Lateral Boundary Strain

Towards the end of this work, a reference was found to data for thin films subjected to normal compressive stresses. Besides the dependence on this normal compressive stress, wrinkle patterns also varied with lateral compression applied along the boundary. They were able to correlate their experimental results with the theoretical Föpple – von Kármán equation. It is likely that following a similar approach for the tensioned membranes studied here would yield results that are equally satisfactory. A summary of Audoly's work follows below.

In the paper, "Secondary buckling patterns of a thin plate under in-plane compression", Audoly et al. experimentally studied the secondary buckling patterns of a

thin poly-carbonate film, under the influence of bi-axial, in plane compression [40]. In this series of experiments, the rectangular film under evaluation was placed horizontally in a fixture. The longer sides of the film, which ran along the lateral direction, were clamped, and the shorter sides of the film, along the longitudinal direction, remained free. Biaxial compression was introduced to the film through the clamps, along both the longitudinal and lateral directions. The experiments of Audoly et al. differed from those performed as part of this work in a number of ways: (1) The longitudinal load applied by Audoly et al. was compressive, whereas the longitudinal load applied in this work was tensile in nature; (2) the poly-carbonate sample was significantly longer in the lateral direction than in the longitudinal direction, while the Mylar and Kapton films evaluated here were nearly square; and most importantly, (3) the average lateral compressive load along the membrane border could be precisely varied. Using this apparatus, Audoly experimentally measured a loading configuration that produced longitudinally-oriented wrinkles. He showed that these wrinkles could be predicted theoretically by solving the Föpple – von Kármán (F. – von K.) equations for the appropriate compressive longitudinal and lateral boundary conditions [40]. These equations are summarized as follows:

$$D\Delta^2\zeta - h\left(\frac{\partial^2\chi}{\partial x^2}\frac{\partial^2\zeta}{\partial y^2} + \frac{\partial^2\chi}{\partial y^2}\frac{\partial^2\zeta}{\partial x^2} - 2\frac{\partial^2\chi}{\partial x\partial y}\frac{\partial^2\zeta}{\partial x\partial y}\right) = 0 \qquad \text{(Eq. 5-1a)}$$

$$\Delta^2\chi + E\left\{\frac{\partial^2\zeta}{\partial x^2}\frac{\partial^2\zeta}{\partial y^2} - \left(\frac{\partial^2\zeta}{\partial x\partial y}\right)^2\right\} = 0 \qquad \text{(Eq. 5-1b)}$$

where,

$$D = \frac{Et^3}{12(1-\upsilon^2)} \qquad \text{(Eq. 5-1c)}$$

and,

E is the Young's modulus of the film,

t is thickness

υ is Poison's ratio

$\zeta(x,y)$ is out-of-plane film deflection

$\chi(x,y)$ is the Airy potential for in-plane stress

Using the F.-von K. equations, a theoretical phase diagram was developed by Audoly et al to show different types of wrinkle patterns expected at different compressive load levels simultaneously applied along the longitudinal and lateral directions. [40] While the authors were more focused on the generation of telephone cord (also called the worm like) patterns that developed at very high values of applied longitudinal and lateral stress (at nearly one-to-one ratios), the phase diagram also showed loading configurations for which wrinkles aligned along the longitudinal direction were produced. These configurations corresponded to relatively low levels of stress, for cases where $\sigma_l/\sigma_t \geq 0.66$. There was an indication in the paper that increasing compression along the clamps in the lateral direction can provide tendencies for a thin film to buckle away from its rest plane [40]. The paper said that in-plane displacements of the film edges of as little as 2 μm are capable of inducing film stresses that can be of the order of the critical lateral load σ_E capable of causing buckling, also known as the Euler's Elastica [40]:

$$\sigma_E = \frac{E\pi^2}{12(1-\upsilon^2)}\left(\frac{h}{b}\right)^2 \qquad \text{(Eq. 5-2)}$$

where

h is the thickness of the film

b is half the height of the film

It was also observed that temperature variations as low as *2K* can cause thermal stresses of the order of the critical lateral load in clamped membranes [40]. This insight clearly illuminates a major challenge in the design of solar sails and other membrane-based spacecraft, as they will likely endure very large temperature swings, as their exposure to sunlight changes during their trajectory. As membrane-based structures orbit the earth, temperature swings can be much higher than the *2K* required to cause stresses sufficient to produce buckling and wrinkling in the films. The difference in the

thermal coefficient of expansions of Mylar films and aluminum clamping apparatus, for instance, can cause compressive strains along the membrane-support interface. This implies that in-plane stresses such as those described may be induced in the films under normal operating conditions, even if the interface between the membrane and the clamp is perfect at the time of fabrication.

Note that Audoly's analysis was performed for simultaneous longitudinal and lateral compression. A separate solution would need to be obtained in order to determine the loadings in this regime that will produce longitudinal wrinkles under simultaneous longitudinal tension and lateral.

5.5 Causes of Wrinkles and Buckling in the Mylar and Kapton Membranes

The findings of Audoly et al. provided some major insight that helped to explain the cause of the longitudinal wrinkling observed in the experiments performed here. Unlike Audoly's, the apparatus described here did not allow for uniform lateral compression to be added to the boundary. However, it is now believed that lateral boundary compression is the main mechanism that causes longitudinal wrinkles in thin membranes. While the amplitudes and wavelengths of these wrinkles will vary depending upon the amount of longitudinal stress (tension or compression) present, the main effect governing the wrinkle configuration is the transverse compressive strain. Unfortunately, the amount of transverse compressive strain in the Mylar and Kapton samples tested here could not be independently controlled or measured. Modifying the setup to allow the edges to be clamped could change this.

In order to explore the relationship between longitudinal wrinkles and lateral edge strain caused by the membrane/clamp interface, a finite element model was created [41]. The model was constructed in ANSYS with about 60,000 SOLID 92 elements (instead of the usual SHELL 181 more typically used to model thin film structures) of Mylar [41]. The model was run in steps due to the non-linearity of the problem, with small increments of displacement strains applied across the edges until a total edge strain of 0.0001m in the negative X (lateral) direction was reached, as shown schematically in Fig. 5-5.

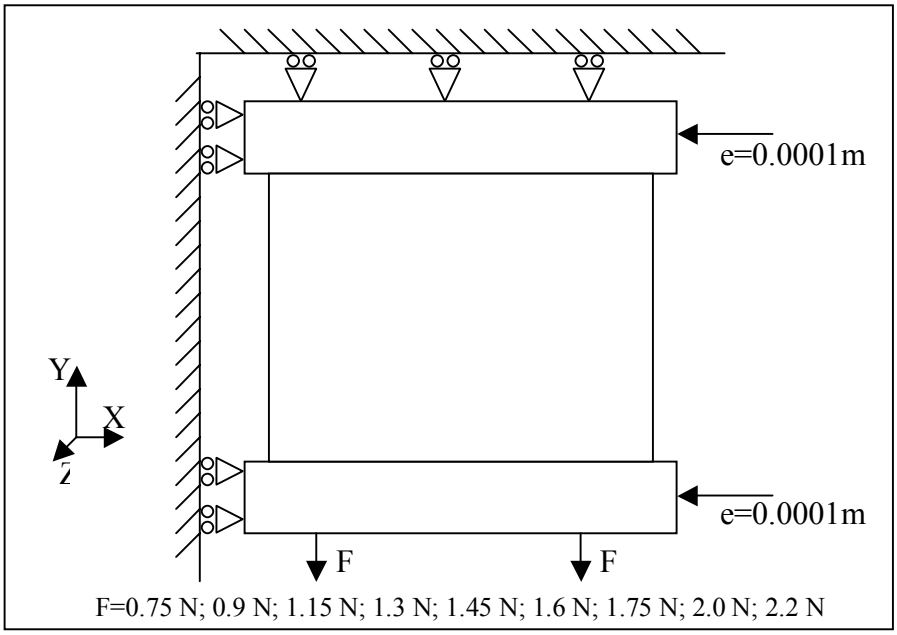

Fig. 5-5: Schematic of the finite element model with tension loads (applied sequentially) after compressive displacements of 0.0001 m along each edge were reached.

After the compressive displacement of 0.0001 m was reached along each edge, tensile forces were applied in pairs on either sides of the membrane (in sequence) in the negative Y direction to provide a net effect of 1.5 N, 1.8 N, 2.3 N, 2.6N, 2.9 N, 3.2 N, 3.5 N, 4 N and 4.4 N. (Note that small out-of-plane forces used to induce buckling in models comprised of shell elements did not have to be utilized here.) These particular values of force were chosen because of their close correspondence to the tension loads used in the experiment. An example of the vertical wrinkles observed in ANSYS in response to the applied loading is shown in Fig. 5-6 [41].

For each set of loads, the out-of-plane displacements (Z) of the membrane were plotted as a function location to measure the amplitude and wavelengths of the wrinkles along a horizontal cross-section of the membrane located approximately halfway between its top and bottom edges. Fig. 5-7 shows a sample of such a plot [41]. These wrinkles cannot be numerically (in ANSYS) induced under a longitudinal tension alone; they can only be induced in the presence of lateral edge compression. Once the longitudinal wrinkles have been induced, their amplitudes and wavelengths can be varied by changing both the longitudinal and lateral load magnitudes. Lateral compressive load magnitude as well as applied tension was noted (qualitatively) to have a large effect on the longitudinal

wrinkle configuration (both wavelength and amplitude). These simulations in the ANSYS along with the analysis by Audoly et. al [40] has confirmed that compressive lateral load levels must be considered in order to properly determine the amplitudes and wavelengths of longitudinal, tension-induced wrinkles.

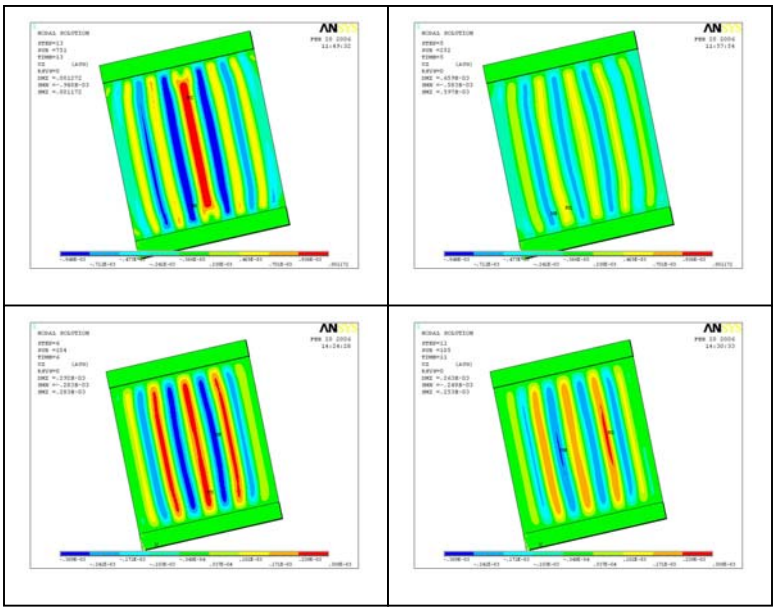

Fig 5-6: Vertical wrinkles observed under applied longitudinal tension forces and lateral compressive strain applied at the membrane edge [41].

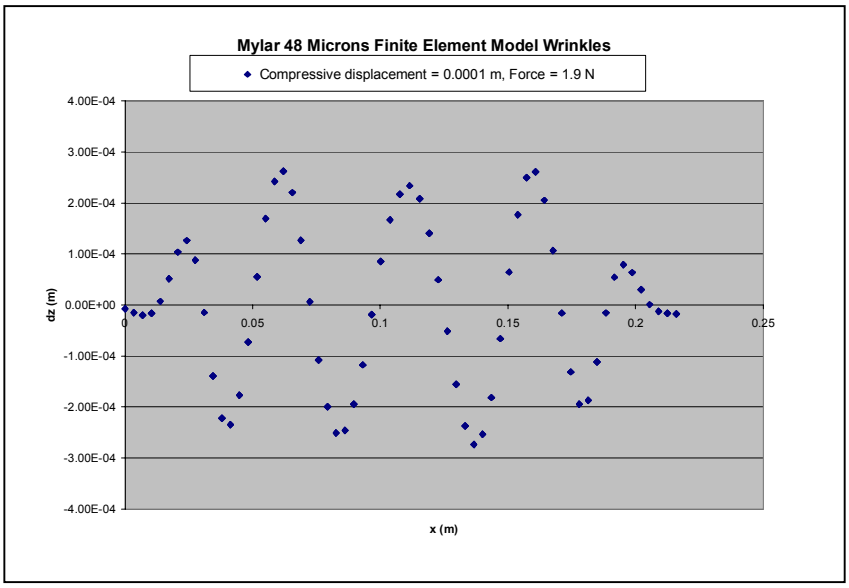

Fig. 5-7: Sample graph of out-of-plane displacements (denoted as Z) plotted against horizontal position (X) over a cross-section of a membrane (simulated in ANSYS) located midway between the top and bottom edges [41].

5.6 Shortcomings of the Correlation between the Numerical Simulations and the Experiment

As we can observe in Fig. 5-7, the amplitude of wrinkles obtained via ANSYS simulation were predicted to range between 0.0002 m to 0.0003 m for a Mylar 0.48 mil thick membrane. The force levels applied in the simulation were consistent with the experimental forces applied to the membrane; however, the experimentally-observed amplitudes only fell between 0.000005m to 0.000015 m. The simulation also predicts wrinkle wavelengths that are significantly larger than those observed experimentally. Another outcome of the simulations (reported elsewhere [41]) is that applied border strain seems to strongly influence wrinkle amplitude and wavelength. Now that it has been established that lateral edge strain is a determining factor in membrane response, two steps need to be taken in order to link the predictions of the numerical simulations to the experimental results: (1) An apparatus, similar to that of Audoly [40], must be built that will allow simultaneous longitudinal tension as well as lateral strain to be applied to a membrane. (2) The FE models must be refined to better model the strain within the membrane/support boundary. This boundary will most likely possess regions of residual compressive lateral strain caused by the manufacturing process, as well as thermal stresses induced by changes in temperature. In addition, physical parameters of the adhesive used to connect the support and the membrane have not been included in the FE model.

5.7 Theoretical Derivation of Wrinkle Wavelength

In view of the discrepancies between the numerical simulations and experimental results, a theoretical derivation for wrinkle wavelength was developed using an approach similar to that reported by Wong and Pellegrino [26-28]. Using this approach, the out-of-plane deflections for a single wrinkle (Fig. 5-8), oriented horizontally across the membrane, are assumed to be

$$W(x,y) = A\sin\frac{\pi x}{\lambda}\sin\frac{\pi y}{H} \qquad \text{(Eq. 5-3)}$$

where W(x,y) is the out-of-plane deflection

A is the Amplitude of the wrinkle

λ is half the wavelength of wrinkle

H is the membrane height

According to Wong and Pellegrino [26], "the compressive stress σ_x acting perpendicular to the wrinkles is set equal to the stress required to buckle a simply supported, infinitely wide plate of length λ that is loaded lengthwise." (Fig. 5-9) Using this approach, the presence of a wrinkle implies that the compressive stress necessary to form it is present in the material. This assumption does not presuppose that the compressive stress is from any particular source within the material.

By Euler's formula, the minimum compressive stress in the x direction required to buckle the material (and hence form the wrinkle) is given by

$$\sigma_x = -\frac{\pi^2 E t^2}{12(1-\upsilon^2)\lambda^2} \qquad \text{(Eq. 5-4)}$$

where E is the Young's modulus of the membrane material

t is the thickness of the membrane

υ is Poisson's ratio

In the Y-direction, the uni-axial stress-strain is assumed valid because the lateral (x) stress required to induce buckling is quite small. Hence, the stress in the Y-direction is given by the uni-axial stress-strain formula:

$$\sigma_y = E\varepsilon_y \qquad \text{(Eq. 5-5)}$$

where ε_y is the strain in the y-direction.

The average uni-axial stress in the y-direction, by definition, can also be calculated using the definition of stress as force over area:

$$\sigma_y = \frac{F}{Lt} \qquad \text{(Eq. 5-6)}$$

where F is the tensile force acting in the normal (y) direction

L is the width of the membrane

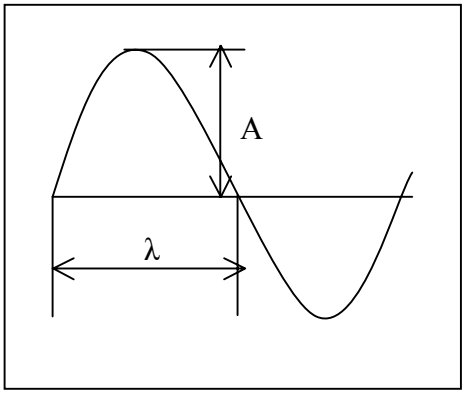

Fig. 5-8: Sketch of a single wrinkle.

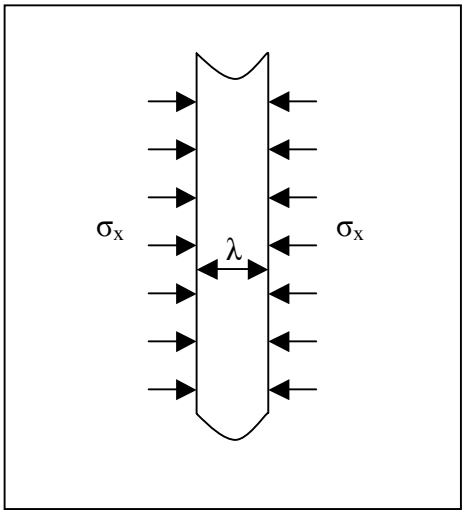

Fig. 5-9: Sketch showing a single wrinkle as a plate of infinite width and length λ under buckling.

Applying the condition of equilibrium for the membrane in the normal direction, we use

$$\sigma_x \kappa_x + \sigma_y \kappa_y = 0 \qquad \text{(Eq. 5-7)}$$

where κ_x and κ_y are the principal membrane curvatures.

The right hand side of the equation is equated to zero because there are no forces acting in the normal direction.

The principles membrane curvatures are given as

$$\kappa_x = -\frac{\partial^2 W}{\partial x^2} \qquad \text{(Eq. 5-8a)}$$

$$\kappa_y = -\frac{\partial^2 W}{\partial y^2} \qquad \text{(Eq. 5-8b)}$$

The negative sign indicates that we have chosen a negative radius of curvature for the single wavelength under analysis.

Using the contour of the wrinkle described by Eq. 5-3, we have

$$-\frac{\partial^2 W}{\partial X^2} = A\frac{\pi^2}{\lambda^2} Sin\frac{\pi x}{\lambda} Sin\frac{\pi y}{H} \qquad \text{(Eq. 5-9a)}$$

$$-\frac{\partial^2 W}{\partial Y^2} = A\frac{\pi^2}{H^2} Sin\frac{\pi x}{\lambda} Sin\frac{\pi y}{H} \qquad \text{(Eq. 5-9b)}$$

Plugging the expressions for σ_x, σ_y, κ_x and κ_y into Eq. 5-7, we get

$$-\frac{\pi^2 Et^2}{12(1-\upsilon^2)\lambda^2}\left[\frac{A\pi^2}{\lambda^2} Sin\frac{\pi x}{\lambda} Sin\frac{\pi y}{H}\right] + \frac{F}{Lt}\left[\frac{A\pi^2}{H^2} Sin\frac{\pi x}{\lambda} Sin\frac{\pi y}{H}\right] = 0 \qquad \text{(Eq. 5-10)}$$

Dividing out the common factor (bracketed), we obtain:

$$-\frac{\pi^2 Et^2}{12(1-\upsilon^2)\lambda^4} + \frac{F}{LtH^2} = 0 \qquad \text{(Eq. 5-11)}$$

Eq. 5-11 can be rearranged to allow direct computation of the wavelength:

$$\lambda = \left[\frac{\pi^2 E t^3 H^2 L}{12F(1-\upsilon^2)} \right]^{\frac{1}{4}} \qquad \text{(Eq. 5-12)}$$

The following assumptions have been made to derive the above formula for calculating the wavelength of wrinkles:

- The lateral stress acting perpendicular to the wrinkles is equal to the stress required to buckle a simple-supported, infinitely wide plate of length λ loaded lengthwise.
- The membrane behaves the same near the free edges as it does near the middle.

Based on the above two assumptions, the values of wavelength have been calculated and tabulated along with those obtained experimentally, in Table 5.1.

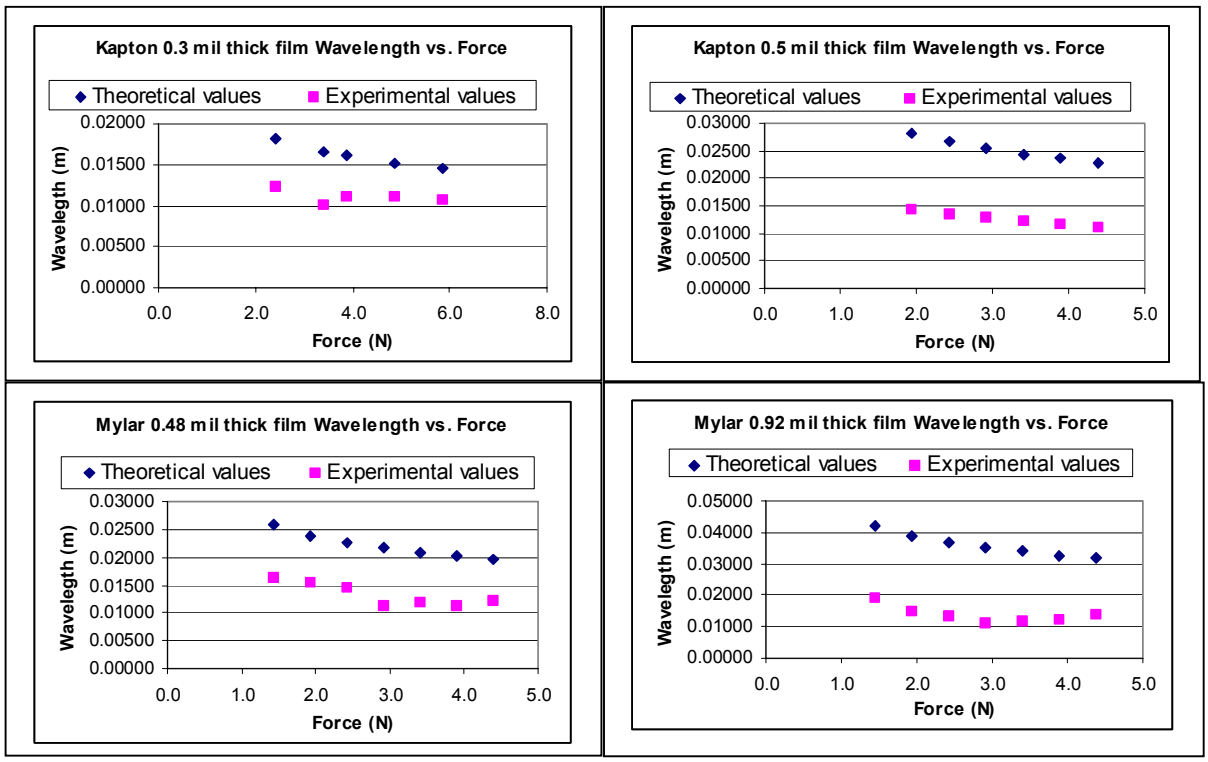

Fig 5-10: Graphs comparing the experimental and theoretical trends for all the test articles.

Film	Thickness(m)	Force(N)	Theoretical Values (m)	Experimental values (m)
Kapton	0.0000076	2.4	0.01810	0.01222
Kapton	0.0000076	3.4	0.01662	0.01001
Kapton	0.0000076	3.9	0.01607	0.01113
Kapton	0.0000076	4.9	0.01520	0.01116
Kapton	0.0000076	5.9	0.01452	0.01066
Kapton	0.0000127	1.9	0.02814	0.01429
Kapton	0.0000127	2.4	0.02660	0.01351
Kapton	0.0000127	2.9	0.02540	0.01294
Kapton	0.0000127	3.4	0.02443	0.01222
Kapton	0.0000127	3.9	0.02362	0.01171
Kapton	0.0000127	4.4	0.02293	0.01107
Mylar	0.0000122	1.4	0.02569	0.01631
Mylar	0.0000122	1.9	0.02389	0.01533
Mylar	0.0000122	2.4	0.02257	0.01457
Mylar	0.0000122	2.9	0.02156	0.01124
Mylar	0.0000122	3.4	0.02074	0.01182
Mylar	0.0000122	3.9	0.02005	0.01120
Mylar	0.0000122	4.4	0.01947	0.01217
Mylar	0.0000234	1.4	0.04188	0.01919
Mylar	0.0000234	1.9	0.03893	0.01499
Mylar	0.0000234	2.4	0.03679	0.01344
Mylar	0.0000234	2.9	0.03514	0.01139
Mylar	0.0000234	3.4	0.03380	0.01175
Mylar	0.0000234	3.9	0.03268	0.01226
Mylar	0.0000234	4.4	0.03173	0.01376

Table 5.1: Comparison of Theoretical values of wavelength to that of the Experimental values

Fig. 5-10 shows the graph comparisons of the theoretical values and experimental values for Kapton and Mylar films. As seen in the graphs, the trends confirm that wavelength decreases with increase in force. It is observed that the average wavelength measured experimentally is less than the theoretical values in general. One possible reason for this discrepancy stems from the fact that Eq. 5-12 assumes that only the minimum amount of compressive stress required to produce a wrinkle is present in the material. The higher levels of compressive stress that are likely present in the physical specimens would cause higher order buckling modes that would in turn have characteristically lower wavelengths.

5.8 Conclusion

The unknown factor in the current experimental set-up, namely, the level of in-plane compressive loads along the clamped membrane edges that were not controlled during the experiment make it highly difficult to compare the experimentally-obtained amplitudes and wavelengths to any analytical or numerical solutions. Time constraints prevented the modification of the experimental setup after the initial set of photogrammetric measurements was made. This shortcoming (unknown boundary strain) in the experimental approach was not realized until late in the work. However, basic trends that link increased longitudinal tension to decreased amplitude and wavelength in thin-film membranes clamped on top and bottom have been verified.

APPENDIX A

Step wise procedure to calibrate the cameras:

Items required:

Camera stand, Calibration sheet, PhotoModeler® Pro software, Tape, Lights

Procedure:

1. Find an empty space of about 5' X 5'. **Tape the Calibration sheet** in the center of the floor.
2. Provide some **lighting** with the help of the lights on the calibration sheet around the perimeter of the workspace.
3. Open one of the **camera** boxes and **attach the battery box** to the camera at the bottom with the help of the screw provided.
4. Open the battery box at the left and **insert a charged battery** into the battery box.
5. Make sure that the **settings on the camera** are as follows:
    a. Remove the front cap
    b. Manual Mode
    c. Focal length turned completely clockwise until it reads 9.
    d. Set to infinite focus by turning the front wheel a couple of turns in the far direction.
    e. Set the camera to manual click.
    f. Push the flash button so that the flash light pops up.
    g. Set camera speed to greater than 80 by turning the appropriate knob.
6. Now attach the camera to the **camera tripod** in an orientation such that the flash light is on the top.
7. Place the camera stand **perpendicular to one of the 4 edges** of the calibration sheet in such a way that its distance from the center of calibration sheet is equal to the height of the camera tripod.
8. Turn the camera on and make sure that it covers all the area of the calibration sheet. If it does not cover, **adjust the position of camera** by moving the camera tripod only.
9. **Take the picture** of the calibration sheet. Put it in the play mode and check that the picture covered the calibration sheet completely and make sure that the dots on the calibration sheet are visible.
10. If the photo is not properly visible, based on the requirements, either **readjust the position of the camera** by moving the stand or **adjust the flash** with the help of Menu options beside the screen of the camera.
11. Repeat steps 7 through 10 for the **other three edges** of the calibration sheet.
12. Now **adjust the camera** in such a way that the **flash faces to the left** while the camera still faces the calibration sheet. This can be done with the help of adjustment knobs provided on the camera tripod.
13. Repeat steps 7 through 11 and **take pictures**.

14. Now **adjust the camera** in such a way that the **flash faces to the right** while the camera still faces the calibration sheet. This can be done with the help of adjustment knobs provided on the camera tripod.
15. Repeat steps 7 through 11 and **take pictures**.
16. **Export the 12 pictures** taken into a computer loaded with PhotoModeler® Pro software with the help of the USB port wire provided by the Camera as accessories.
17. **Open PhotoModeler®** Pro software. **Close the tutorials** option that pops up.
18. Click file and select **new project** option. Select a **calibration project**. Click **next** twice.
19. Write the **camera name** as Camera 1, Camera 2 etc. Click next.
20. Select, "No this camera has only **one focal Length"**. Click **Next**. Select camera type as **digital**. Select **next**.
21. **Export the pictures** from the saved location into the software through the **add/remove images option**. Click **next**. Click **finished**.
22. The camera will **calibrate itself**. Click **Tables** and select **point tables** option. Select **Quality option** in the top menu. Double click on the **largest residual** and make sure that none of them cross 1.00. If most of them do, **redo** the complete experiment.
23. Save the PhotoModeler® file under the **camera #** calibration file name.
24. Remove the Camera from the stand and repeat steps 3 through 23 for **other three cameras**.
25. **Remove** the set up, stand, lights and calibration sheet.

APPENDIX B
PHOTOGRAMMETRY IN MANUFACTURING

Introduction

Close range photogrammetry is starting to become more and more prevalent in industrial applications. Also know as Vision metrology, Industrial photogrammetry has been a major field of interest for manufacturing ever since the early 1970s [10]. Vision metrology is used in applications where non-contact measurement methods are required for one or more reasons.

The process used in close range photogrammetry generally involves taking a number of images of the object of interest using either a single or multiple cameras. These pictures can then be processed to determine the XYZ locations of target points placed on the surface of the object. These points can then be used to reconstruct the object shape by mathematically fitting a surface through the point cloud.

Applications in Manufacturing

Some of the major applications of industrial photogrammetry to manufacturing include the following [10]:

Measurement of Molds, Patterns or Models for Input to a CAD Database

Photogrammetry is widely used in reverse engineering. Any physical model or object already available can be captured through imaging and processed to mathematically determine its shape. One way of doing this is to physically place targets on the model surface to allow calculation of the object's critical dimensions during the surface reconstruction. These critical dimensions are then entered into CAD software to allow the existing point to be changed based on the photogrammetric measurements, allowing for subsequent fabrication of the modified part. This is especially important in cases where the original parts, drawings and measurements have been lost.

Periodic Inspection of Tools, Jigs and Fixtures

Some tools, jigs and fixture setups are quite complicated and cannot be manually measured to ensure that the intended setup has not changed. As periodic inspections of these setups are required to ensure that no unintended deflections have occurred, the photogrammetry process can be used to calculate various 3D coordinates for comparison with a set of benchmarked 3-D coordinates taken from the correct setups. Deviations from the unintended setups are then analyzed using predetermined tolerances and thresholds for acceptance of further usage of the tools, jigs or fixtures. Fig. B-1 shows a fixture used in automotive environment that contain targets used for photogrammetric analysis [11].

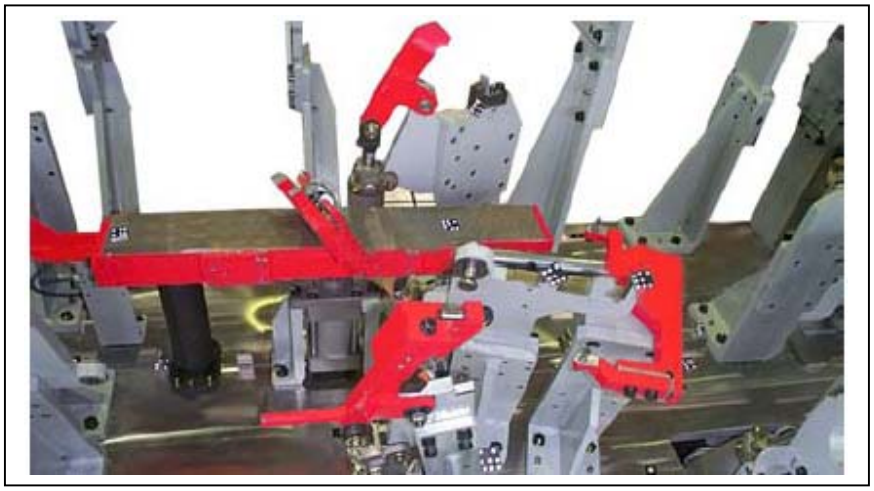

Fig. B-1: Application of Photogrammetry to measure the dimensions of a fixture in automotive industry [11].

Measurements in Dangerous Environments

In nuclear plants, where certain environments are not safe, photogrammetry can be used for measuring and maintaining the plant. Fig. B-2 shows the view of control rods that are measured and maintained in a French nuclear plant [12]. In this particular example, it is required that the positions of the control rods be controlled with high accuracy for proper regulation of the nuclear plant reaction.

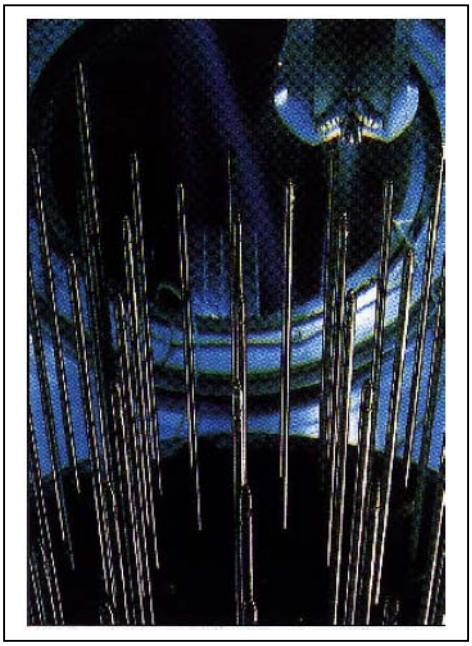

Fig. B-2: View of Control rods in a French nuclear plant [12].

Measurement of Large and Expensive Equipment

It may be required to determine the physical shape taken on by a mechanical system while it is operating. At other times, analyzing equipment while it is operating is desirable, as the shutdown of large and expensive equipment for measurement or maintenance purposes can be very expensive. Measurements of operating equipment that cannot be obtained through the use of traditional contacting methods can be accomplished through the use of vision metrology. Fig. B-3 shows one such example involving the world's largest electric ring motor incorporated into an ore crusher at a gold mine in New South Wales. It appeared that the stator became elastically deformed when the amperage to the motor was increased. [13] Using photogrammetry, the stator shape was analyzed for a number of different amperages. It took 25 minutes to record the 10 or so images required at each current level, and less than 10 additional minutes to measure all the images and perform the bundle triangulation required to precisely determine the shape of the stator[13].

Fig. B-3: Application of photogrammetry on large and expensive equipment.

Challenges Faced by Photogrammetry in Industry

In order that industry accepts photogrammetry as a powerful tool for measurements, many issues had to be addressed. Other metrology devices like theodolites and laser trackers posed a major threat to the application of photogrammetry systems. Photogrammetric systems required high accuracy in measurements. Also the end user of vision metrology systems is usually untrained and requires user-friendly software for ease of operation. Some of the technological enhancements incorporated by the photogrammetry industry to penetrate the metrology market were:

Intelligent Cameras

Digital cameras used in photogrammetry were generally classified into 3 categories based on their price and accuracy [14]. The first type of cameras is amateur cameras which range around $1500 and provide accuracy of the order 1:20,000 [14]. These are generally easily available and are designed for normal photography purposes. However, they can be used to perform photogrammetry in some research applications. The demanding requirement of short image acquisition and processing time in industry generally results in avoiding this type of cameras. The second type of cameras is professional cameras which cost around $10,000 and provide accuracy of the order of about 1:100,000 [14]. The third category called the photogrammetric cameras cost around

$60,000 and provides accuracies of the range 1:200,000. Based on the requirements of the industry both the above categories are used for various applications. Due to the continuing demands, the costs are reducing on these cameras. Fig. B-4 shows INCA 6.3 released by Geodetic Services Inc [15]. INCA("INtelligent CAmera" abbreviated) has an on board PC that compresses images, sets exposure automatically and also measures the image. Another example of a good photogrammetric camera widely used is Kodak DCS 460 (shown in fig. B-5). It offers measurement accuracies of about 1/40 pixel which leads to a relative accuracy of about 1:100000. The camera has an image grabber file with storage capacity of 6.0 megabytes and the imager itself of size 2036 pixels * 3060 pixels [16].

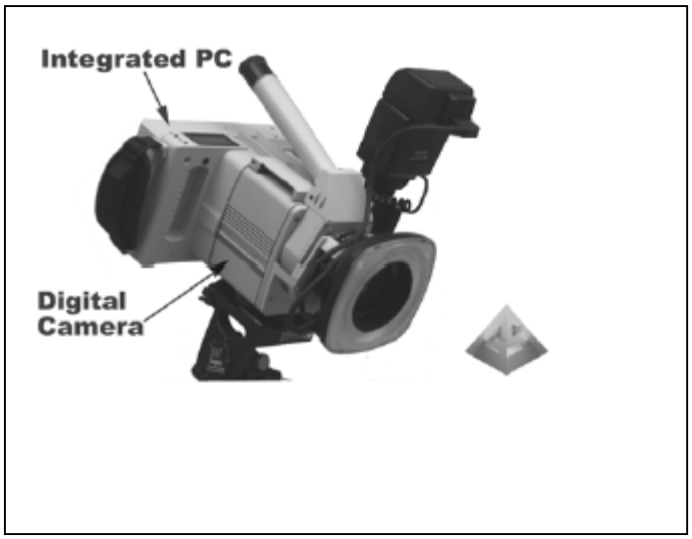

Fig. B-4: "INCA 6.3" camera [15].

Fig. B-5: Kodak's DCS 460 [16].

Targeting the Object

Generally, it is required to code the object of observation using Retro-reflecting targets. These targets are then photographed using the above-mentioned cameras. The targets are then matched in various photographs to locate the point. Most of the cameras require calibrating them for the purpose of usage. This process is usually done with the help of standard coded targets and standard automated initial exterior orientation methods [14]. Pictures of these coded targets are imported into the photogrammetric software to calibrate itself to the specifications of the camera. However, these days, self-identifying

targets are developed to directly help the software calibrate as well as process and measure the object in observation [11]. A stored file helps the software to realize the already loaded target and thus recognize and measure without the requirement of any manual processing or manual calibration [11]. Fig. B-6 [11] and Fig. B-7 show some examples of coded targets.

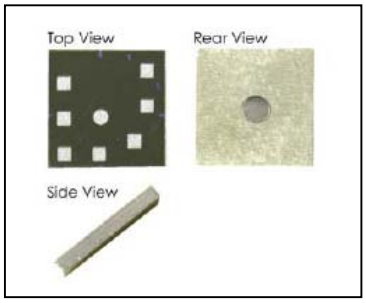

Fig. B-6: Plane target [11].

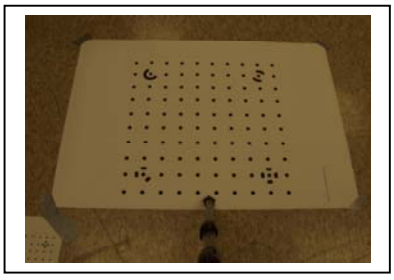

Fig. B-7: Coded target used for calibration.

Image Analysis

The next logical process that has ongoing developments and research underway is the processing of images to return the XYZ coordinates of the final image. The software package that handles the image analysis consists of various algorithms that are improved everyday by improved technologies and technical capabilities. Bundle Adjustment algorithms and multi-photo orientation algorithms determine the best locations of the cameras based on data collected like camera information, user and system photo markings etc [16,17]. The algorithm creates a functional relation between the image coordinate system and the actual coordinate system of the corresponding points in the object coordinate system. This transformation matrix is then used to realize the position of the camera [16]. Automated marking algorithms automatically mark the target points thereby avoiding human errors in sub pixel markings and thus help in increasing accuracy of measurements [17]. Research has proved the successful linking of image processing tools with photogrammetric techniques. Some of the common shapes like cylinders and cuboids can be easily recognized with the help of image processing which would further help in reducing the time to process and match the images [12]. Common software available in the markets is V-Stars system offered by the Geodetic Services Inc. and FotoG™ offered by the Vexcel Corporation. Eos systems Inc. offers stand alone software called the PhotoModeler®.

Measuring Factors

Photogrammetry is analyzed by the time taken to perform the following functions.

Image Acquisition

This is time taken to take the pictures, compress the images and store inside the camera. This is a major step where most of the time is spent and can be potentially be automated to save considerable amount of time.

Image Transfer

This is the time taken to transfer images into a local PC hardware that has access to photogrammetry software. Use of digital photography automated image transfer can save considerable amount in this process.

Initial Exterior Orientation

This is the time taken to initially orient the cameras with the use of assorted hand held probes, auto bars or initial calibration techniques. The use of self identifiable targets can save considerable amount of time in this process [11].

Initial Bundle Adjustment

This step follows the exterior orientation step where the algorithm orients the targets to calibrate the software. The automation of the previous step also partially automates this step.

New Point Determination

This step includes locating and labeling of points in at least two images in order to cross reference and match similar points in other images. Using image processing tools and other mathematical rules, most of this process can be automated.

Final Bundle Adjustment

Once the points are matched in different images, the cameras are required to be reoriented by the computer to acquire better accuracies.

Clean-up and Re-bundle

The bundle algorithm fails to cross reference certain points and these points tend to be the outliers in the process. Hence, they are deleted and the bundle adjustment algorithm is performed to re-orient the camera locations.

Potential Applications of Close Range Photogrammetry in Manufacturing Environments

Inspection using current metrology methods such as manual gauging with a micrometer for measurement consume time and labor. This step in many production processes can be automated with the help of close range photogrammetry. A series of cameras are placed around the assembly line on which the product passes. The number of cameras depends on the accuracy requirements as well as the intricacies in the product design. Images taken by each camera as parts pass by the inspection station are then processed through a computer, and in certain circumstances can almost immediately provide the dimensions of the part. These dimensions can then be programmed through a statistical process control system to pass or stop the further transportation of the product. Judicious targeting of the parts can be used to identify critical points and dimensions. Fig. B-8 shows a schematic diagram of an off-line close range photogrammetry process. The product moves on the production line while the 4 cameras installed to capture the image of the product with the targets on it. These pictures are then processed through the computer to measure the dimensions of the product and thereby check the compliance to the required specifications. Current technologies, accuracies and image processing speeds can make this application very feasible.

The high precision of photogrammetry can help in resolving the measurement challenges in the industry of nanotechnology or small objects manufacturing. Objects of small size provide challenging problems in dimensional measurements. PCB assemblies can be fed into the computer with each major component in the layout fed as coded targets into the photogrammetric software and images can be compared to the main design fed into the software for verification. With commercial photogrammetric packages like V-Stars and PhotoModeler®, measurements can be provided with high accuracy and precision.

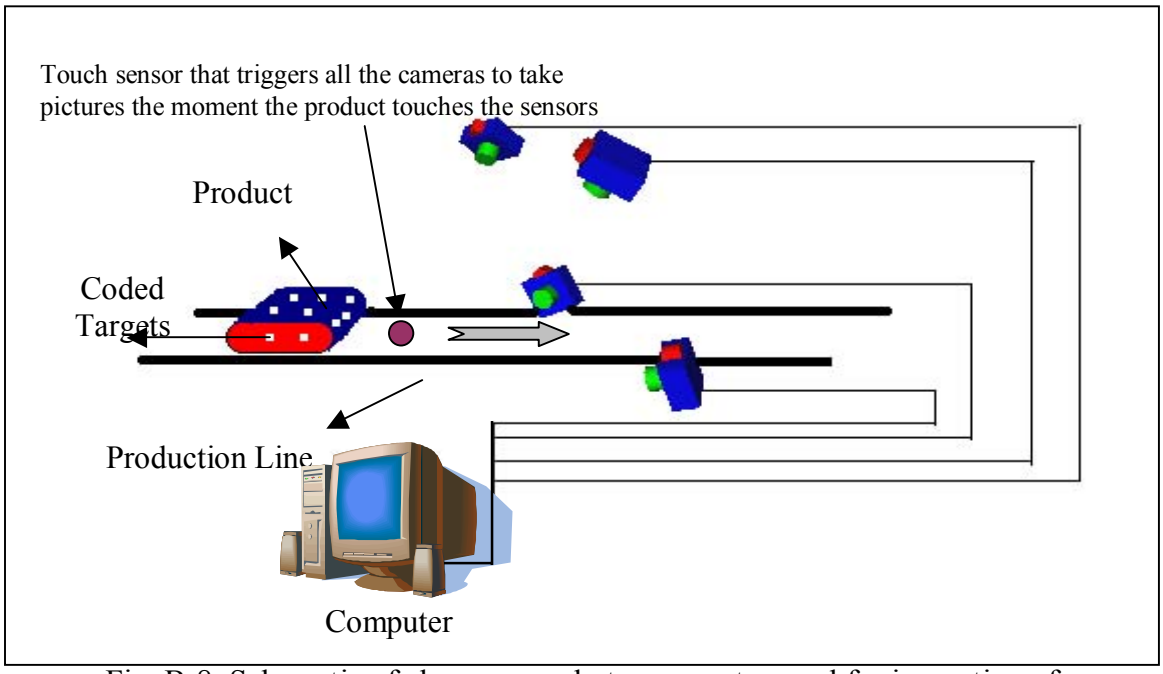

Fig. B-8: Schematic of close range photogrammetry used for inspection of specifications of a product on a production line.

Conclusion

The growing popularity of photogrammetry in industry provided new ways of performing certain operations in industry. Due to the fact that photogrammetry is a conglomeration of different industries like photography, image processing and software technologies, the growth sounds promising for further integration and synergetic outcomes with broader applications to manufacturing. Based on the requirement of the industry, photogrammetric packages along with the right cameras can be chosen to tailor the needs of the measurements. If the accuracy question can be answered by choosing the right camera, the response time can be controlled by the use of the right photogrammetric software and coding systems.

Bibliography

1. Website on the History works of Dr. Robert Leggat.

   www.rleggat.com/photohistory/history/cameraob.htm, accessed 29 SEP, 2005.

2. Website on the history of photography and the camera

   http://inventors.about.com/library/inventors/blphotography.htm, accessed 29 SEP, 2005.

3. Leggat, R., *"A history of Photography from its beginnings till the 1920s"*

   http://www.rleggat.com/photohistory/ accessed 29 SEP, 2005

4. Website of the University of Hannover, Institute for Photogrammetry and Geo-Information.

   www.ipi.uni-hannover.de/elan/iso/history.htm accessed 29 SEP, 2005.

5. History of Photogrammetry by the Center for Photogrammetric Training, Surveying Engineering Department, Ferris State University.

   http://www.ferris.edu/htmls/academics/course.offerings/burtchr/sure340/notes/History.pdf accessed 29 SEP, 2005.

6. Doyle, F., 1964. *"The Historical Development of Analytical Photogrammetry"*, Photogrammetric Engineering, XXX(2): 259-265

7. Konecny, G., 1985. *"The international Society for Photogrammetry and Remote Sensing – 75 years old, or 75 years young"*, keynote address, Photogrammetric Engineering and Remote Sensing, 51(7), pp 919-933.

8. Meyer, R., 1987. *"100 Years of Architectural Photogrammetry"*, Photogrametrie, Vol. XIX, Leipzig: Akademische Verlagsgessells shaft, pp. 183-200.

9. Doyle, I.W., 1980 *"Sherman Mills Fairchild"*, Photogrammetric Engineering and Remote Sensing, 46(7), pp 923-936.

10. The Official Website of 3-Space Inc. www.3-space.com/3space_2.html accessed 29 SEP, 2005.

11. Ganci, G., Clement, R., 2000. "The Use of Self-identifying Targeting for Feature Based Measurement", Coordinate Measuring System Committee, Dearborn, Michigan.

12. Naudet, S., Viala, M., Sayd, P., Cohen, L., Jallon, F., Dumont, A., Monnerie, J., 2001. " An As-Built On-line Modeling Technique AOMS" from website www.ceremade.dauphine.fr/~cohen/mypapers/ceaisprs2000.pdf accessed 29 SEP, 2005.

13. Fracer C. 1999. "Automated Vision Metrology: A Mature Technology for Industrial Inspection and Engineering Surveys", 6th South East Asian Surveyors Congress, Fremantle, Western Australia.

14. Fraser, C., 2001. "Automated Off-line Digital Close Range Photogrammetry: Capabilities and Applications", 3rd International Image Sensing Seminar on New Developments in Digital Photogrammetry, Gifu, Japan.

15. Ganci, C., Handley, H., "Automation in Videogrammetry" from the website of the department of Geomatics at the University of Melbourne http://www.sli.unimelb.edu.au/hanley/html/papers/VideoAutomation.pdf accessed 29 SEP, 2005.

16. Gayde, J.C., Humbertclaude, C., Lesseur, C., "Prospects of Close Range Photogrammetry in Large Physics Installations", C.E.R.N., Geneva, Switzerland.

17. Website of Eos Systems Inc. www.eossystems.com/coretech_tech.html accessed 29 SEP, 2005.

18. Blandino, J.R., Johnston, J.R., Miles, J.D., Salop, J.S., 2001. "Thin Film Membrane Wrinkling due to Mechanical and Thermal loads", 45th AIAA/ASME/ASCE/AHS/ASC Structures, Structural Dynamics and Material Conference and Exhibit, Seattle, WA. AIAA-2001-1345

19. Jenkins, C.H.M., Gough, A.R., Pappa, R.S., Caroll, J., Blandino, J.R., Miles, J.J., Rakoczy, J., 2004. "Design Considerations for an Integrated Solar Sail Diagnostics System". AIAA-2004-1510

20. Lichodziejewski, D., Derbes, B., Reinert, R., Belvin, K., Slade, K., Mann, T., 2004. "Development and Ground Testing of a Compactly Stowed Scalable Inflatable Deployed Solar Sail" AIAA-2004-1507.

21. Leifer, J., Black, J., Belvin, W., Behun, V., "Evaluation of Shear Compliant Borders for Wrinkle Reduction in Thin Film Membrane Structures", 44th AIAA/ASME/ASCE/AHS/ASC structures, Structural Dynamics, and Materials Conference, Norfolk, Virginia.

22. Pappa, R.S., Black, J.T., Blandino, J.R., 2003. "Photogrammetric Measurement of Gossamer Spacecraft Membrane Wrinkling", NASA.

23. Dorrington, A.A., Jones, T.W., Denehy, P.M., Pappa, R.S., 2004. "Laser-Induced-Flourescence Photogrammetry for Dynamic Characterization of Membrane Structures" AIAA Journal, 0001-1452, vol. 42, no. 10, 2124-2129.

24. Black, J.T., Leifer, J., Demoss, J.A., Walket, E.N., Belvin, W.K., 2004. "Experimental and Numerical Correlation of Gravity Sag in Solar Sail Quality Membranes" AIAA-2004-1579.

25. Lichodziejewski, D., Derbes, B., West, J., Reinert, R., Belvin, K., Pappa, R., 2003. "Bringing an Effective Solar Sail Design towards TRL6" AIAA-2003-4659.

26. Wong, Y.W., Pellegrino, S., 2002. " Amplitude of Wrinkles in Thin Membranes" New approaches to structural mechanics shells and biological structures, Kluwer Academic Publishers, 257-270.

27. Wong, Y.W. and Pellegrino, S., 2002 "Computation of Wrinkle Amplitude in Thin Membranes" 43rd AIAA/ASME/ASCE/AHS/ASC Structures, Structural Dynamics and Materials Conference, Denver, CO, AIAA 2002-1369.

28. Wong, Y.W., and Pellegrino, S., 2003. "Wrinkled Membranes", Textiles Composites and Inflatable Structures, CIMNE, Barcelona, 2003.

29. The website of online solution provider Malaysian Internet Resources, http://www.mir.com.my/rb/photography/companies/nikon/htmls/models/specroom98/e3/ accessed 29 SEP, 2005.

30. The website of Nikonians®, a community formed by Nikon® users. http://www.nikonians.org/html/resources/guides/digital/how_does_it_work_1.html accessed 29 SEP, 2005.
31. The website of http://www.startphoto.com/learn/glossary/glossary_so-sz.htm accessed 29 SEP, 2005.
32. Photogrammetric terms described in the website of Leica Geosystems http://gis.leica-geosystems.com/support/FocusOn/FocusOn_detail.aspx?article_ID=17 accessed SEP 29, 2005.
33. Karabork, H., Yildiz, F., Coskun, E., 2004. "Object Recognition for Interior Orientation in Digital Photogrammetry", XX International Society for Photogrammetry and Remote Sensing Congress, Istanbul, Turkey.
34. Calladine, C.R., 1983 "Theory of Shell Structures", Cambridge University Press, Cambridge.
35. Wong, Y.W., 2000 "Analysis of Wrinkle Patterns in Prestressed Membrane Structures", thesis, University of Cambridge.
36. Thota, P., Leifer, J., Smith, S.W., Lumpp, J.K., 2004, "Pattern Evaluation for In-Plane Displacement Measurement of Thin Films" Society of Experimental Mechanics, Vol. 45, No. 1, 18-26.
37. Leifer, J., Belvin, W.K., 2003 "Prediction of Wrinkles Amplitudes in Thin Film Membranes using Finite Element Modeling" AIAA-2003-1983.
38. Pappa, R.S., Giersch, L.R., Quagliaroli, J.M., 2000 "Photogrammetry of a 5m Inflatable Space Antenna with Consumer Digital Cameras" NASA/TM-2000-210627.
39. Jenkins, C. H., Haugen, F., Spicher, W.H., 1998 "Experimental Measurement of Wrinkling in Membranes undergoing Planar Deformation" Experimental Mechanics 38, 147-152.

40. Audoly, B., Roman, B., Pocheau, A., 2002, "Secondary Buckling Patterns of a Thin Plate under In-plane Compression" The European Physical Journal B, 27,7-10.

41. Leifer, J., Morgan, B.G., Mangalampalli, S., "Structural Wrinkling of Thin Gossamer Films under Edge Shear and Tension," In preparation for submission to Journal of Experimental Mechanics.

Vita

Author's Name – SreeRam Mangalampalli

Birthplace – Kakinada, India

Birthdate – January 12, 1981

Education

Bachelor of Technology in Mechanical Engineering (Mechatronics)

Jawaharlal Nehru Technological University, India.

April - 2002